



**HAL**  
open science

# Area selective deposition of microcrystalline silicon by PECVD : physical origin, challenges and solutions.

Ghewa Akiki

## ► To cite this version:

Ghewa Akiki. Area selective deposition of microcrystalline silicon by PECVD : physical origin, challenges and solutions.. Physics [physics]. Institut Polytechnique de Paris, 2021. English. NNT : 2021IPPAX129 . tel-03662473

**HAL Id: tel-03662473**

**<https://theses.hal.science/tel-03662473v1>**

Submitted on 9 May 2022

**HAL** is a multi-disciplinary open access archive for the deposit and dissemination of scientific research documents, whether they are published or not. The documents may come from teaching and research institutions in France or abroad, or from public or private research centers.

L'archive ouverte pluridisciplinaire **HAL**, est destinée au dépôt et à la diffusion de documents scientifiques de niveau recherche, publiés ou non, émanant des établissements d'enseignement et de recherche français ou étrangers, des laboratoires publics ou privés.

# Area selective deposition of microcrystalline silicon by PECVD: physical origin, challenges and solutions.

Thèse de doctorat de l'Institut Polytechnique de Paris  
préparée à l'École Polytechnique

École doctorale n°626 Ecole Doctorale de l'Institut Polytechnique de  
Paris (ED IP Paris)  
Spécialité de doctorat: Physique

Thèse présentée et soutenue à Palaiseau, le 13 Décembre 2021, par

**Ghewa Akiki**

Composition du Jury :

Agnès Granier Directrice de recherche, IMN, Nantes (UMR 6502)	Présidente
Christophe Vallée Professeur, Université Grenoble Alpes	Rapporteur
Thierry Belmonte Directeur de recherche, IJL, Nancy (UMR 7198)	Rapporteur
Adrie Mackus Assistant professor, TU Eindhoven, The Netherland	Examineur
Muriel Bouttemy Ingénieure de recherche, ILV, Versailles (UMR 8180)	Examinatrice
Erik V. Johnson Directeur de recherche, LPICM (UMR 7647), Ecole Polytechnique	Directeur de thèse
Pavel Bulkin Ingénieur de recherche, LPICM (UMR 7647), Ecole Polytechnique	Co-Directeur de thèse
Sergej Filonovich Ingénieur, TotalEnergies, IPVF	Invité



# ***Acknowledgements***

I finished my three years of PhD in the LPICM and I am glad to say that it was one of the best experiences I have had in my life (excluding, of course, the lockdown and the COVID restrictions).

My first and most sincere gratitude goes to my amazing thesis director Erik V. Johnson and co-director Pavel Bulkin. I never regretted a single day my decision to do my PhD with you. I learned enormously from you, scientifically and mostly improved a lot personally. I sincerely believe that it would be difficult to have better supervisors. I cannot express how much I am thankful. I appreciate the continuous support of Erik (even during the lockdown), for his positive feedback after every presentation even if it was bad, for enhancing my self-confidence, for his organized supervision and for his guidance in every step in my thesis. I couldn't feel the impact of his great management until the end of my thesis when I realized how easy was to organize my manuscript. I would thank Pavel for welcoming me in his office every day every hour, for his teaching, for his caring, and for trusting my capability in working autonomously on the ALD and ATOS (and a lot more). Also thank you Pavel for pushing me beyond my limits always and one more important thing thanks a lot for your advice regarding wine choices. In this context, I would like to thank you both Pavel and Tatiana Novikova for your advice (that helped me a lot on personal level) and for your many dinner invitations.

Secondly, I would like to acknowledge Agnès Garnier, Thierry Belmonte, Christophe Vallée, Adrie Mackus, Muriel Bouttemy and Sergej Filonovich for accepting to be a part of my jury. I appreciate your effort, whether to come to Ecole Polytechnique despite the degraded COVID19 sanitary situation and discussing my work or the time difference constraints. I want to specifically thank Christophe Vallée for being my reference in the area selective deposition field and for all our discussions in the conferences. I hope to meet you in the future in the United States. My gratitude goes to Muriel and Mathieu Frégnaux for the XPS experiments. You never hesitated to answer my questions and help me understand this method. In addition, special thanks to Muriel for her help in the award applications and for her interest in my topic.

I would also like to thank all LPICM members for your welcome, your friendliness and your help throughout my thesis. I will start by thanking Ileana Florea and Costel Cojocaru for accepting me as an intern in their group even if my profile was a little bit far from their topic. I appreciate the opportunity that you gave me and your recommendations. Thank you Ileana for your help in the TEM, for the time that you spent on preparing my samples, for your continuous support and caring.. Then, I want to thank Yvan Bonnasieux (and his wife) for helping me in all french application corrections, Pere Roca my office “neighbor” for cheering me up during my writing by just doing small gestures (candies, flowers, staying late...), Cyril Jadaud for solving ARCAM troubleshooting (and all other issues) and for the encouragement (ca faisait du bien de parler du ski, de la pêche de n’importe quoi sauf du travail quand rien ne fonctionne!!), Patxi in the 3D printer, Jean Charles , Fabienne Pandolf (je n’oublie jamais ton fort beau sourire), Laurence Gerot and Gabriela Medina (merci pour votre réactivité dans les procédures administratives et pour l’attention que vous m’avez donné), Aleix Guell (you made me like and master the AFM!! I will miss your great company to Lozere rer B station late at night), Eric Paillassa (j’espère que j’ai bien fait attention au PC) and Jacqueline Tran. It was always a pleasure to discuss with Fatima Bouanis, Angelo Pierangelo, Holger Vach, Jean-Luc Maurice, Francois Silva, Marc (surtout dans les impressions des poster), Jerome Charliac, Didier Pribat, Denis Tondelier, Khaoula Jemli.

A big thanks to the PhD and postdoc colleagues that we have shared a lot of good memories. I am really glad to meet you all. Thanks to my compatriots Mariam Ezzedine for your help during my internship and for your caring whenever you see me down, Haifa Taoum and Joseph Chakar for organizing the “cagnotte” (I wish we spent more than three months together), Loan my all-time office colleague (you will be released soon), Hindia Nahdi (my partner in the lab animation), Junha Park, Daniel Funes-Hernando (even if your wine wins we will still be friends), Guili Zhang (I will miss your delicious food), Marta Mucientes (your gift was super helpful in my defense), Monalisa Ghosh (I will miss our chat together), Junkang Wang, Martina Papa, Minjin Kim (the dirty jokes guy), Haeyeon Jun (thank you for always inviting us to your room to taste delicious Korean meals), Heeryung Lee (the chef), Robert Benda, Gookbin Cho, Anatole Desthieux, Deyan Ivanov, Omar Rodriguez-Nunez (for your encouragement), Antonio-de-jesus Olivares-Vargas (I hope I wrote it right), Chaoqi Wang, Shenming Wang, Clotaire Chevalier, Andjelika Bjelajac, Fatme Jardali, Mengkoing Sreng, Chloe Dindault, Letian Dai for sand blasting my dirty deposition in ARCAM, Ronan Leal, Michel Goncalves and Mihai Zamfir. There were many good memories in the 408

building but the chocolate breaks with my best colleagues Marta Chrostowski (je ne peux plus regarder le manuscrit) and Romain Bude were among the best. Thank you for your support till the end.

Throughout my PhD, I spent a big part of my PhD in the cleanroom of Thales preparing my samples. I would like to thank firstly Dmitri Daineka for teaching me the first lithography steps, for helping me in all the logistics and for being there whenever I need his help. Secondly, my sincere gratitude goes to Etienne Eustache. I appreciate your interest in my project and your advice on my silly problems. Our discussions helped me a lot in advancing in my PhD. I also would like to thank Julie Cholet for her availability and her reactivity and Anne-lise for the hints.

Besides, thank you Sandrine Tusseau-Nenez from PMC for your help in the XRD measurements and Alexandre Blaizot for the AFM measurements in IPVF.

Finally, thank you to my friends in Paris (or more specifically in Ile de France) for making this whole period easier: Maher, Tatiana, Hanady, Nour, Georges and last but not least to my special person Samer (yes we did it together). Thank you, mum and dad, my lovely sisters Maha and Lea, my handsome brother Maroun, Mirene and my cute Teresia for being there for me despite the distance. Without you, I wouldn't be the person I am.



# Contents

<b>1</b>	<b>Introduction.....</b>	<b>1</b>
1.1	Solid state technology.....	2
1.2	Area Selective Deposition.....	6
1.2.1	Definition.....	6
1.2.2	Area Selective Chemical Vapor Deposition.....	7
1.2.3	Area Selective Atomic Layer Deposition.....	9
1.3	Microcrystalline Silicon Deposition.....	12
1.4	Thesis outline.....	19
	References.....	20
<b>2</b>	<b>Experimental Techniques.....</b>	<b>29</b>
2.1	Sample fabrication.....	30
2.1.1	Deposition techniques used for substrates preparation.....	31
2.1.1.1	Atomic Layer Deposition.....	31
2.1.1.2	Plasma Enhanced Chemical Vapor Deposition.....	33
	a) Chemical Vapor Deposition.....	33
	b) Plasma.....	34
	c) Radio Frequency PECVD.....	35
	d) Electron cyclotron resonance PECVD.....	37
2.1.2	Patterned substrates fabrication.....	39
2.1.2.1	Photolithography steps.....	39
2.1.2.2	Etching.....	42
2.1.2.3	Photoresist removal.....	42
2.2	Experimental setup.....	43
2.2.1	ARCAM.....	43
2.2.2	ATOS.....	44
2.2.3	Ellipsometry.....	45
2.3	Sample and plasma characterization techniques.....	47
2.3.1	Atomic Force Microscopy.....	47



2.3.2	Scanning Electron Microscopy .....	49
2.3.3	Transmission Electron Microscopy .....	50
2.3.4	X-ray Photoelectron Spectroscopy .....	51
2.3.5	Contact angle measurement .....	53
	References .....	56
<b>3</b>	<b>Area Selective Deposition Process .....</b>	<b>63</b>
3.1	Optimal plasma parameters.....	64
3.1.1	Area selective plasma conditions in ARCAM-PECVD reactor .....	65
3.1.2	Ex-situ ellipsometry and SEM of the selective silicon deposition samples.....	66
3.1.3	Area selective plasma conditions in ATOS reactor .....	71
	a) Monitoring deposition by in-situ ellipsometry .....	73
	b) Microcrystalline nature of the deposited silicon layer .....	76
3.2	Losing selectivity .....	79
3.2.1	Effect of gas flow rates .....	80
3.2.2	Effect of plasma power and substrate electrode temperature .....	81
3.2.3	Surface contamination .....	83
3.3	AS-PECVD for different materials.....	85
3.4	Summary .....	89
	References.....	91
<b>4</b>	<b>Origins of Area selective PECVD process .....</b>	<b>93</b>
4.1	Chemical characterization of substrate surfaces .....	94
4.1.1	Energy dispersive X-ray (EDX) chemical analysis on SiO <sub>x</sub> N <sub>y</sub> and AlO <sub>x</sub> areas after plasma deposition process .....	94
4.1.2	X-ray photoelectron spectroscopy (XPS) chemical analysis for SiO <sub>x</sub> N <sub>y</sub> and AlO <sub>x</sub> areas .....	97
4.1.3	Surface-wetting characterization of AlO <sub>x</sub> and SiO <sub>x</sub> N <sub>y</sub> areas .....	101
4.2	Plasma characteristic.....	104
4.2.1	Plasma optical emission spectra .....	104
4.2.2	Peak to peak and V <sub>DC</sub> measurements for different plasma conditions ....	107
4.3	Summary .....	111
	References .....	113

<b>5</b>	<b>Selective processes for patterned substrates .....</b>	<b>119</b>
5.1	Challenges in the fabrication of patterned substrates .....	120
5.1.1	Recall lithography steps .....	120
5.1.2	Contamination .....	121
5.1.3	Solutions to resist contamination .....	122
5.1.4	Sensitivity to process details .....	125
5.2	ASD on patterned substrates: .....	127
5.2.1	Chemical and topographical characterization .....	127
	a) Contact angle measurement .....	127
	b) Atomic Force Microscopy .....	129
	c) X-ray Photoelectron Spectroscopy .....	131
5.2.2	Area selective $\mu\text{c-Si}$ on patterned substrate with different dimension .....	138
	a) Far from pattern area .....	140
	b) Reduced $\text{SiO}_x\text{N}_y$ feature size .....	142
5.3	Summary .....	148
	References .....	150
<b>6</b>	<b>Conclusion and perspectives .....</b>	<b>151</b>
Appendix	.....	155
Appendix A	.....	156
Appendix B	.....	159
Appendix C	.....	162
Appendix D	.....	163

# ***List of Acronyms***

<b>Acronyms</b>	<b>Definition</b>
Extreme Ultra-Violet	EUV
Ultra-Violet	UV
Area Selective Deposition	ASD
Atomic Layer Deposition	ALD
Chemical Vapor Deposition	CVD
Plasma Enhanced Chemical Vapor Deposition	PECVD
Area Selective Chemical Vapor Deposition	AS-CVD
Area Selective Atomic Layer Deposition	AS-ALD
Self-assembled monolayers	SAMs
Plasma Enhanced Atomic Layer Deposition	PEALD
Atomic Layer Etching	ALE
Hydrogenated microcrystalline silicon	$\mu\text{c-Si:H}$
Microcrystalline silicon	$\mu\text{c-Si}$
Hydrogenated amorphous silicon	a-Si:H
Transmission Electron Microscope	TEM
Radio Frequency Plasma Enhanced Chemical Vapor Deposition	RF-PECVD
Trimethylaluminium	TMA
Aluminum Oxide	$\text{AlO}_x$
Silicon Oxynitride	$\text{SiO}_x\text{N}_y$
Reactive Ion Etching	RIE
Capacitively Couple Plasma	CCPs
Electron Cyclotron Resonance	ECR
Optical Emission Spectroscopy	OES
Spectroscopic Ellipsometry	SE
Atomic Force Microscopy	AFM
Scanning Electron Microscopy	SEM

High Resolution Transmission Electron Microscope	HR-TEM
Energy Dispersive X-ray Spectroscopy	EDX
Focus Ion Beam	FIB
X-ray Photoelectron Spectroscopy	XPS
Water Contact Angle	WCA
Surface Free Energy	SFE
Cristalline Silicon	c-Si
Corning Glass	CG
X-Ray Diffraction	XRD
Grazing Incidence X-Ray Diffraction	GIXRD
Scanning Transmission Electron Microscopy	STEM
High-Angle Annular Dark Field	HAADF
Fast Fourier Transform	FFT
Ion Bombardment Energy	IBE
Root Mean Square roughness	RMS roughness



# Chapter 1

## Introduction

1.1	Solid state technology .....	2
1.2	Area Selective Deposition .....	6
1.2.1	Definition .....	6
1.2.2	Area Selective Chemical Vapor Deposition.....	7
1.2.3	Area Selective Atomic Layer Deposition.....	9
1.3	Microcrystalline Silicon Deposition.....	12
1.4	Thesis outline .....	19
	References .....	20

## **1.1 Solid-state technology**

Solid-state or semiconductor devices are electronic components formed using semiconductor materials. In 1874, the first semiconductor device (a DC-AC converter) was invented [1]. Nevertheless, the era of semiconductors did not truly begin until the development of the point-contact transistor by J. Barden and W. Brattain in 1947, followed by the creation of the bipolar junction transistor in 1948 by W. Shockley. In 1959, the invention of the metal–oxide–semiconductor field-effect transistor by M. M. Atalla and D. Kahng was a major breakthrough in the transistor research field, making it the most manufactured transistor worldwide. Later on, the integrated circuit (IC) was created by J. Kilby of Texas Instruments and R. Noyce of Fairchild Semiconductor in 1974. These now consist of thousands to billions of semiconductor devices (transistor, resistors, capacitors and diodes) interconnected on one small chip of silicon. From that time on, the development of electronic appliances exploded, starting from radios, calculators, watches and more recently laptops and smartphones.

Semiconductors are not just used for computing and memory, but also as power devices needed in the fabrication of refrigerators, microwaves and LCD (liquid crystal display) televisions. Recently, they became the backbone of green technology, including hybrid cars, fuel cells and solar cells. Another important class of semiconductor devices is the Micro Electro Mechanical Systems (MEMS) that are found in the sensor components.

As semiconductor devices become vital in everyday life, the continuous development in this field is crucial. The semiconductor industry follows Moore's law, which is a prediction that the economically viable number of semiconductor devices per silicon chip will double every two years [2]. This was achieved mainly by reducing or miniaturizing the dimensions of the devices from the micrometers scale, called microelectronics, to nanoscale, called nanoelectronics (devices in the order of 20 nm and smaller).

Nowadays, as the device makers reach the limits of miniaturization, the invention of new materials, new device geometries, and new circuit architectures is required to achieve higher performance and reduced cost per device. An example of a new transistor structure is the tunnel field effect transistor as an energy efficient transistor [3-5] and negative

capacitance field effect transistor [6, 7]. Nevertheless, the fabrication of such devices require less familiar materials than silicon, such as SiGe, Ge, III-V semiconductors (GaAs, InP, GaN), and 2D materials (graphene, transition metal dichalcogenides TMD) [8]. New types of semiconductor geometry have also appeared that consist of vertical stacking (the so-called 3D architecture (Fig. 1.1)). It relies on stacking devices vertically instead of putting small devices horizontally on the same chip [9].

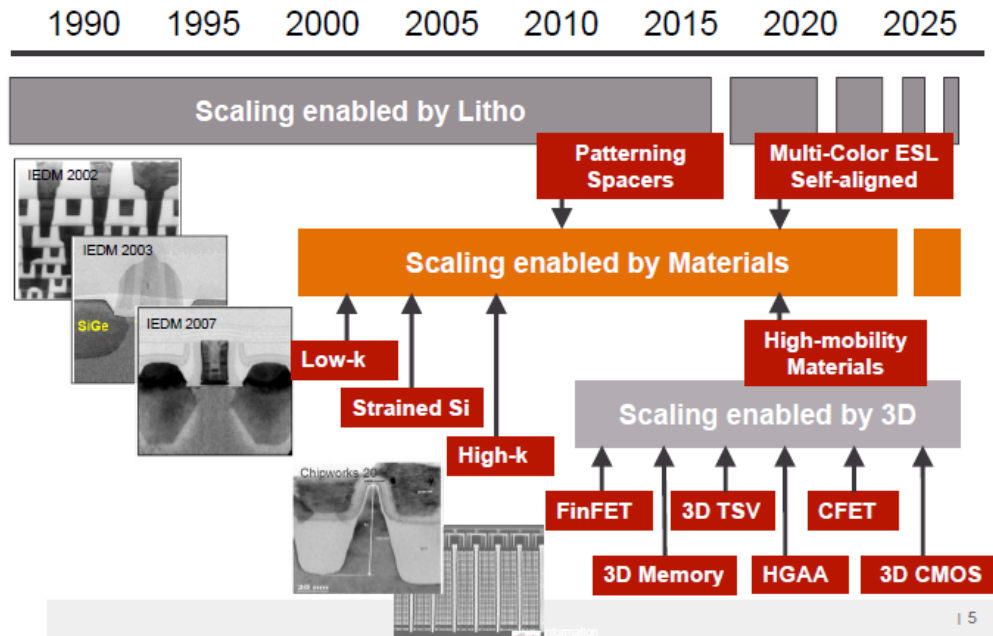


**Figure 1.1** Future technologies in the semiconductor industry based on 3D architecture and new materials (ASM Analyst and Investor Report)

New fabrication processes are also needed for the new generation of semiconductor manufacturing that potentially could replace the top-down approach used in current microelectronic fabrication based on lithography.

Photolithography (or optical lithography) is the process most widely used for microfabrication or nanofabrication. It uses light to reproduce the patterns from a photomask on a substrate following the steps illustrated in Fig. 1.2. First, a polymer solution called photoresist is spin coated on a substrate. This photoresist is exposed to UV light through a photomask. The exposed photoresist<sup>1</sup> is chemically modified so that it can be soluble in a

<sup>1</sup> In this figure the photoresist is "positive", and exposed areas are subsequently removed



chemical solution (developing step). The resulting patterns created in the photoresist are used as a mask to prevent etching or deposition of a material on a specific zone of the substrate.

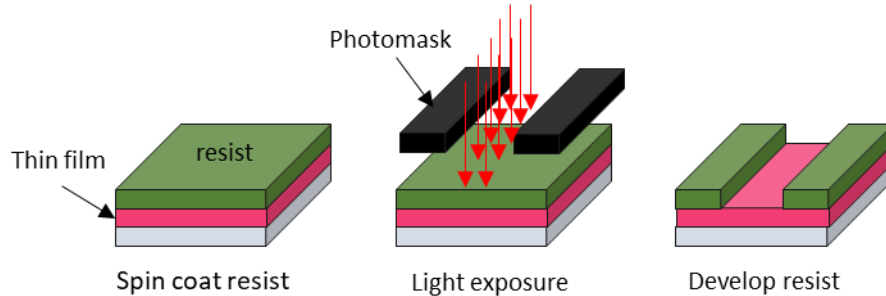


**Figure 1.2** Main steps of standard photolithography

The resolution ( $R$ ) of a projection photolithography process is defined as the smallest feature that can be printed and it is determined by the well-known Rayleigh equation:

$$R = \kappa_1 \frac{\lambda}{NA} \quad (1.1)$$

Where  $\kappa_1$  is a constant that depends on the specific resist material, process technology and image-formation technique used,  $\lambda$  is the exposure wavelength of the light source and  $NA$  is the numerical aperture of the lens in the optical system.

Therefore, by increasing  $\lambda$  or decreasing  $NA$ , better resolution can be reached [10]. Fig. 1.3 shows the evolution of photolithography resolution with time. At first, the wavelength of the light source was 436 nm or 365 nm, corresponding to the g-line or i-line of a mercury lamp, respectively. In 1995, deep ultraviolet excimer lasers have been introduced into the production of semiconductor devices [11, 12]. At that moment, krypton fluoride (Kr-F) excimer lasers at 248 nm wavelength and argon fluoride excimer lasers (Ar-F) at 193 nm wavelength become the most common illumination sources for lithography, as they enabled a decrease of feature sizes from 250 nm down to 70 nm. Subsequently, optical lithography resolution has been improved by combining Ar-F excimer lasers and liquid immersion lithography. The latter is based on adding a liquid of a refractive index greater than 1 between the lens and the wafer in order to increase the numerical aperture up to 1.55 [11].

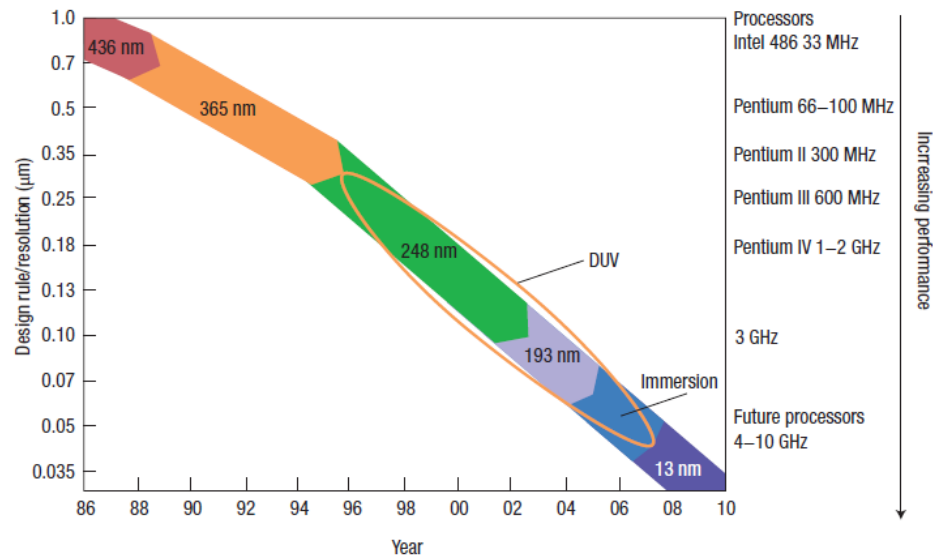


**Figure 1.3** Increase of photolithography resolution with reducing light source wavelength. DUV refers to Deep Ultra-Violet immersion lithography at the wavelengths of 248 nm and 193 nm. The resolution is reduced by adding a liquid (water) between the lens and the wafer (immersion lithography). [11]

Current research is pushing for a better resolution by developing Extreme Ultra-Violet (EUV) lithography that couples a laser produced-plasma with a sophisticated optical system [13, 14]. It enables the production of features of the order of 10 nm in size. However, EUV lithography systems are extremely expensive (around 100 million USD per machine) and the mask for exposure is hard to fabricate.

In parallel to the EUV lithography, the fabrication of devices in the order of 10 nm can be still achievable by UV lithography through the introduction of self-aligned, multiple patterning method [8]. This approach is used for the fabrication of lines and spacers in semiconductor devices. In this method thin film material is supposed to be deposited on top of photoresist but in practice the growth of this material occurs inside the photoresist as it is a porous layer. This will cause problems in the photoresist removal. Afterwards, the wiring process to connect the fabricated elements is done by multi-step lithography. It is based on the deposition of vias directly on top of the fabricated line. Unfortunately, since the corresponding surface is about 20 nm in size or less, the positioning of the growth of a layer on top of another layer (layer to layer alignment) becomes more and more complicated. It

leads to more fabrication issues, such as the edge placement error resulting from an imperfect alignment of a mask on a target zone (see Fig. 1.4) [15].

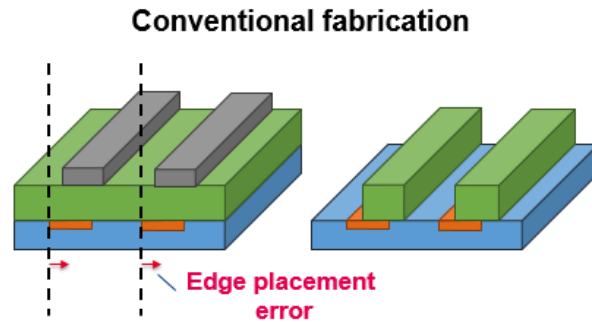


**Figure 1.4** Schematic representation of the edge placement error in conventional patterning techniques [16]

A promising solution to the problems named above is to develop new bottom-up approaches as alternatives to the top-down patterning techniques or conventional lithography techniques, as they can eliminate the step of the deposition of material on photoresist and reduce edge placement errors. The idea is to design a process that enables the deposition of a thin film on a specific area of the substrate, with atomic resolution. Such techniques are called area selective deposition (ASD). They are gaining increasing interest for academic and industrial researchers and are in rapid development. In fact, some ASD processes have been already included in nanoelectronics production.

## 1.2 Area Selective Deposition

### 1.2.1 Definition

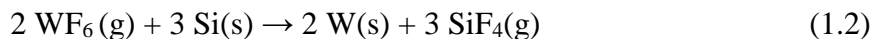
Area-selective deposition (ASD) is an approach that controls where deposition takes place through the properties of the surface and the nature of surface material rather than through any masking step. It promotes the deposition on the target “growth” area of a substrate while preventing deposition on the “non-growth” area. Atomic Layer Deposition (ALD) and Chemical Vapor Deposition (CVD) are the most widely-used techniques employed to achieve ASD, depositing metals, semiconductors, and insulators [17, 18]. These techniques work either by activating the growth area surface, passivating or deactivating the

non-growth area surface, adding a co-reagent to the precursors, or treating the surfaces prior to the process in a way to block any deposition or etching [19, 20]. A brief description of area selective ALD and CVD based approaches, including their development, will be given.

### **1.2.2 Area Selective Chemical Vapor Deposition (AS-CVD)**

The first Area Selective Deposition processes were achieved in 1962 using chemical vapor deposition<sup>2</sup>. Work started with the selective epitaxial growth of semiconductors such as silicon (Si) and gallium arsenide (GaAs) using silicon tetrachloride (SiCl<sub>4</sub>)/hydrogen (H<sub>2</sub>) and a GaAs source/ hydrochloric acid (HCl) or arsenic trichloride (AsCl<sub>3</sub>)/H<sub>2</sub>, respectively [21, 22]. In these cases, chlorine was the factor that promotes the selectivity, as it can reduce the rate of deposition of Si and gallium (Ga) [23]. Afterwards, selective Plasma Enhanced Chemical Vapor Deposition (PECVD) of amorphous silicon on Si surfaces was accomplished by modulating the flow of silane (SiH<sub>4</sub>) and hydrogen gases in time [24]. Selectivity is attributed to alternating deposition and etching processes that maintain the growth on Si surfaces, but prevent the growth on SiO<sub>2</sub> surfaces due to the nucleation delay in the presence of atomic hydrogen. In another study, silicon dots were selectively deposited on SiO<sub>2</sub> by forming OH-terminated areas [25]. Thus, the substrate of a given material can be both the growth and the non-growth surface, depending on the process and techniques employed, as long as the surface is treated differently.

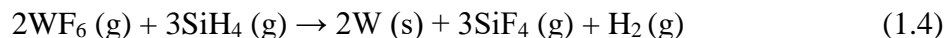
As for metals, selective tungsten CVD has been demonstrated in two reaction steps using tungsten fluoride gas mixtures (WF<sub>6</sub>/H<sub>2</sub>). In the first step, bare silicon is considered as a solid reducing agent, as it can lose an electron and dissociate WF<sub>6</sub> to deposit tungsten (W) (equation 1.2).



Once the first W layer is formed, any gaseous reducing agent such as H<sub>2</sub> or SiH<sub>4</sub> reduces WF<sub>6</sub> and assures a steady growth of W (equations 1.3 and 1.4).

---

<sup>2</sup> More details about this technique can be found in chapter 2



On the other hand, no reduction of the  $\text{WF}_6$  precursor occurs on  $\text{SiO}_2$ , as the Si in  $\text{SiO}_2$  is fully oxidized, preventing W growth [23, 26]. However, selective tungsten deposition is limited to about 200 nm layer thickness on Si, as for thicker layers, W starts to grow on  $\text{SiO}_2$  surfaces as well. Selective tungsten deposition has been also demonstrated using low pressure CVD and remote plasma CVD [27].

In addition, selective CVD of metallic aluminum on Si/ $\text{SiO}_2$  patterned samples was achieved using triisobutylaluminum (TIBA). The reaction of the precursors with  $\text{SiO}_2$  surfaces led to the creation of a monolayer containing C and Al that doesn't react with additional precursor molecules [28].

In these examples, AS-CVD could be achieved as a consequence of the dissimilar interaction of the precursor with different surfaces. On the non-growth surface, the precursor either does not stick directly, or it reacts and saturates the surface with a relatively stable layer. This layer blocks the reaction of any additional precursor with which it comes into contact. On the growth surface, however, deposition dominates all other surface-precursor interaction events (see Fig. 1.5) [29].

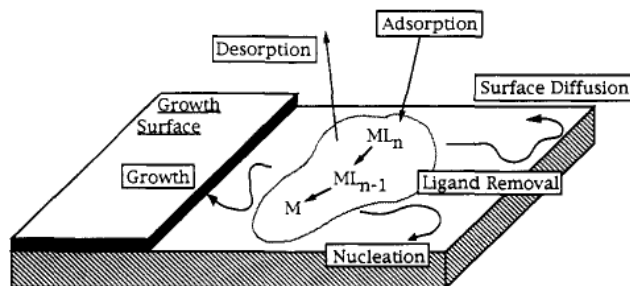


**Figure 1.5** All possible events on growth and non-growth surfaces under the same precursor flux [29]

Another approach for AS-CVD is the addition of an inhibitor to the process that passivates one surface and promotes deposition on another. Such is the case for  $\text{MoC}_x\text{N}_y$ , Fe and Ru thin films deposited selectively on metal surfaces but not oxide surfaces [30]. Similarly, the selective deposition of cobalt (Co) thin film is obtained on acidic oxides versus

basic oxides when a flow of  $\text{NH}_3$  is added to the precursors [31]. A recent approach relies on the introduction of “co-adsorbate” species during the process. For example, 4-octyne chemical species bind more strongly to copper (Cu) surfaces compared to  $\text{SiO}_2$  surfaces, blocking the growth of  $\text{ZrO}_2$  film on Cu [32] (Fig. 1.6).

A. H. Simon et al. showed the potential of AS-CVD processes by comparing selective CVD cobalt capping to industry-standard CuMn alloy seed layers on 22 nm-groundrule copper interconnects [33]. However, the direct application of AS-CVD in the microelectronic fabrication is currently quite minor.

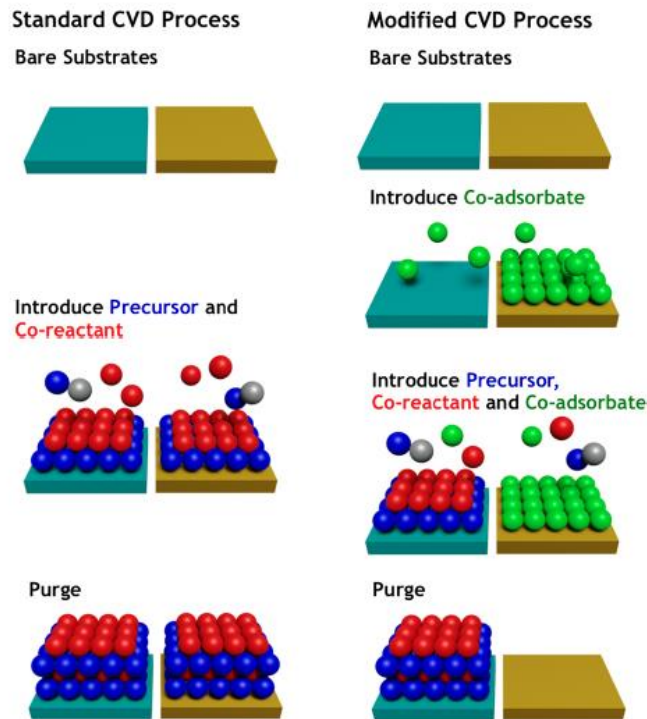


**Figure 1.6** AS-CVD approach based on addition of co-adsorbate species (green circles), sticking on one surface (green) but not another surface (gold) [32]

### 1.2.3 Area Selective Atomic Layer Deposition (AS-ALD)

Several years ago, ASD has been studied in ALD as it is a surface reaction dependent process and produces a high quality film with a very uniform thickness across the wafer.

This technique is based on alternating two gases, precursor and co-reactant, in a half-cycles in a sequential manner. A full ALD cycle would be completed after exposure of the surface to both precursors<sup>3</sup>. There are three main approaches for AS-ALD that can be summarized as (1) activation of the growth surface, (2) deactivation of the non-growth surface or (3) alternating cycles of deposition and etching.

The first two approaches rely on the application of different modifications to a surface prior to the ALD process. For example, a seed layer can be formed on the growth area to catalyze and promote the deposition. As a result, precursor or co-reactant gases will selectively adsorb on the growth area only [34]. Another kind of treatment can be performed by exposing the surface to an H<sub>2</sub> plasma [35] or by depositing organic films such as self-assembled monolayers (SAMs) [36-44] or polymers [45-49]. These organic films preferentially react with a certain type of surface (metals or oxides) inhibiting any film growth during the subsequent ALD process. The key in such techniques is to make a specific surface more hydrophobic after polymer or SAMs deposition, as hydrophilic surfaces enhance growth while hydrophobic surfaces block deposition [48]. An example of the passivation of an area for an ASD process is presented in Fig. 1.7. In this case, AS-ALD is a three step process that repeats until a specific thin film thickness is reached on the growth area. Step A consists of the selective adsorption of inhibitor molecules on the non-growth area. In step B, the growth precursor is generated and binds only on the growth area. The oxygen in step C acts as the co-reactant that removes precursor ligands and etches inhibitor molecules. However, this methodology is beset with many constraints, such as the adsorption of the precursor on the inhibitor, and losing the inhibitor molecules after a few cycles, to name a few [50].

---

<sup>3</sup> Detailed description of ALD technique can be found in chapter 2

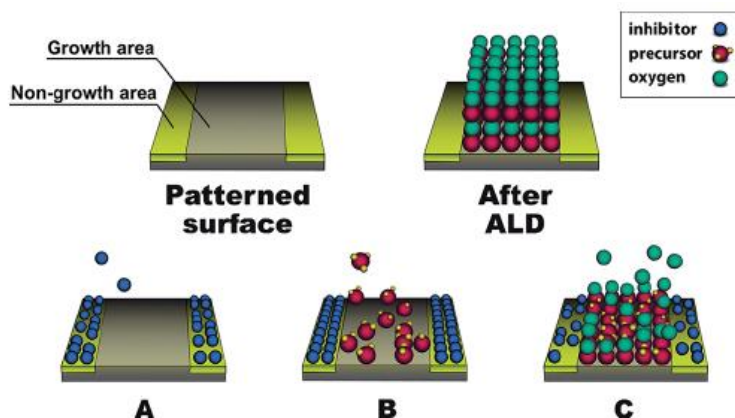


**Figure 1.7** Schematic illustration of AS-ALD process using inhibitor molecules to prevent growth on one area. [39]

One domain in ASD research focuses on alternating deposition and etching. This so-called “super-cycle” method benefits from the nucleation delay between two different surfaces to get the first monolayers to deposit selectively. Then, an etch step is introduced to reinitiate a new nucleation delay [51-54]. In fact, for certain precursors, the nucleation delay depends strongly on the surface properties and chemistry. However, this nucleation delay appears only at the first stage of the growth process and for a relatively short time [20]. R. Vallat et al. have demonstrated the inclusion of a plasma etching step to Plasma Enhanced ALD (PEALD) to “reset” the nucleation delay on the no-growth area. Doing so, a super cycle of deposition and etching processes are repeated until the desired thickness is reached on the growth area [51]. Fig. 1.8 shows an example of the main steps for the super-cycle approach [54]. First a substrate with a surface composed of different materials (represented in grey and red) is loaded for an ALD process. After several cycles, the deposition has already advanced on the red area, while on the grey area, it has only just started. Then, an etching step is performed, by Atomic Layer Etching (ALE), to stop the growth on the grey area, etch the deposited nuclei, and reset a new nucleation delay. Finally, this super-cycle of deposition and etching is repeated until the desired thickness is reached on the red area.



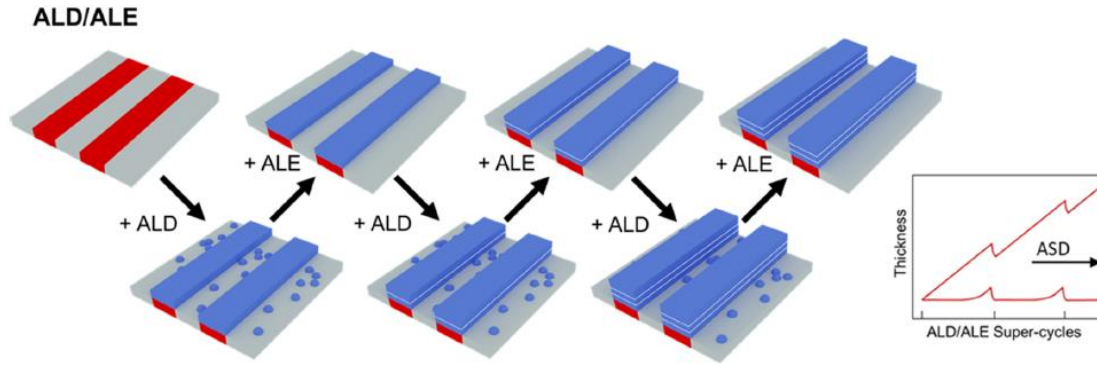


**Figure 1.8** Schematic of the deposition (ALD) + etching (ALE) super-cycle approach [54]

### 1.3 Microcrystalline Silicon Deposition

In this thesis, the main materials studied are thin films of hydrogenated microcrystalline silicon ( $\mu\text{c-Si:H}$ ), so this section includes the growth mechanism of this specific type of silicon, as well as previous research studies from the LPICM about this subject

In general, the growth of crystalline materials is a result of consecutive processes starting from nucleation, followed by island growth, coalescence of those islands forming a continuous layer [55, 56]. Similarly, growth mechanism for  $\mu\text{c-Si:H}$  consists of an incubation phase, wherein a seed layer of crystallites (possibly within an amorphous layer) is deposited on the substrate, followed by a columnar growth of crystalline zones that collide and fuse, forming in the end a continuous layer [57]. The resulting  $\mu\text{c-Si:H}$  layer is different from its amorphous counterpart, hydrogenated amorphous silicon ( $\text{a-Si:H}$ ) in that it has a smaller band gap and higher infra-red absorption compared to  $\text{a-Si:H}$ . Those properties made it a good choice for photovoltaic applications, especially in tandem junctions with  $\text{a-Si:H}$ .

The most common technique used to deposit high quality  $\mu\text{c-Si:H}$  is plasma-based deposition or more specifically Plasma Enhanced Chemical Vapor Deposition (PECVD). Many details could be discussed if considering all the varying plasma chemistries that can be used to grow  $\mu\text{c-Si:H}$  by PECVD. I will instead focus in this section on the growth steps for two main plasma chemistries:  $\text{SiH}_4/\text{H}_2$  and  $\text{SiF}_4/\text{H}_2$  gas mixtures.

Regarding the growth mechanism from **SiH<sub>4</sub>/H<sub>2</sub>**, the first event that happens before the growth of either a-Si or  $\mu\text{c-Si:H}$  is the decomposition of the gases in the plasma [56]. In the case of a SiH<sub>4</sub>/H<sub>2</sub> mixture, under low pressure (<10 Pa) and low power (< 10 mW/cm<sup>2</sup>), SiH<sub>3</sub> is considered to be the main growth precursor, as SiH<sub>3</sub> radicals are found to be the dominant chemical species detected in the steady state plasma [58, 59]<sup>4</sup>. SiH<sub>3</sub> physisorbs on the H covered surface and diffuses until it chemisorbs on a dangling bond or recombines with SiH to form SiH<sub>4</sub> or Si<sub>2</sub>H<sub>6</sub> (when combining with another physisorbed SiH<sub>3</sub>) [60]. During this process, the first crystalline nuclei may randomly form, probably aided by the presence of atomic H. If the plasma conditions encourage the growth of crystalline material over amorphous material, these first nuclei (nucleation) will grow faster than the surrounding a-Si:H, forming cones. When the cones collide, a continuous layer is formed with a roughness dependent on the density of nuclei.

The next important parameter to look at is the hydrogen dilution ratio  $R = [\text{H}_2]/[\text{SiH}_4]$  as the nature of the grown film depends strongly on this parameter<sup>5</sup>. As shown in Fig. 1.9, by increasing R, the microstructure of the deposited Si:H thin film changes from the amorphous phase (a-Si) to a mixed amorphous and microcrystalline phase (a+ $\mu\text{c:Si}$ ) to then reach microcrystalline phase ( $\mu\text{c:Si}$ ), all for the same substrate temperature [61]. In the figure, protocrystalline Si:H refers to the thin-film material in the amorphous regime of growth. In addition, one can note that depending on the hydrogen dilution, the first several angstrom of  $\mu\text{c-Si}$  thin film growth consist of either an a-Si incubation layer (if  $20 < R < 40$ ) or just instantaneous nucleation of nano/microcrystallites (if  $R > 40$  for this temperature, power and pressure).

---

<sup>4</sup> When increasing pressure and power, other species such as SiH<sub>2</sub> and eventually higher silanes will take part in the growth, and SiH<sub>3</sub> will not be the only precursor

<sup>5</sup> The ratio of plasma species fluxes at the surface together with ion energy determine the nature of the deposited layer.

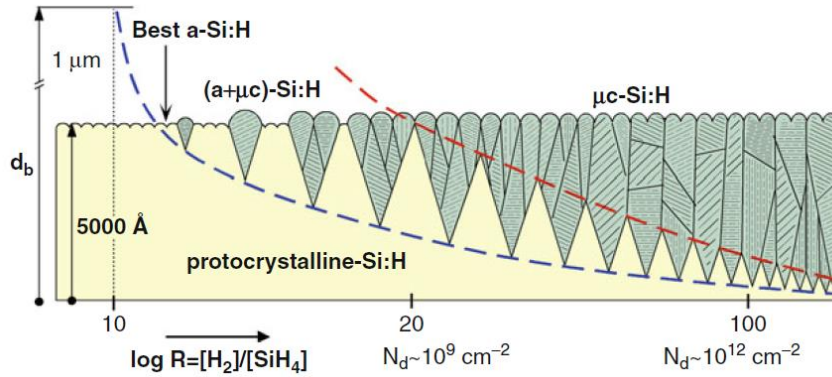


**Figure 1.9** Schematic representation of the microstructure evolution in the bulk thickness  $d_b$  as a function of hydrogen dilution of silane  $R = [H_2]/[SiH_4]$ . The blue and red dashed lines indicate the  $a \rightarrow (a+\mu c)$ , and  $(a+\mu c) \rightarrow \mu c$  transitions, respectively.  $N_d$  is the density of nucleating centers of microcrystalline growth. [61]

C.R. Wronski et al. represent the evolution of the microstructure as function of  $SiH_4$  dilution in a different way (Fig. 1.10). The silane dilution is inversely proportional to the amorphous Si phase amount compared to the crystalline phase amount in the layer [63]. Indeed, at very low silane dilution,  $\mu c$ -Si has a columnar structure with relatively large grains but no amorphous tissue. While for a slightly higher dilution, growth starts with an a-Si incubation layer following by the nucleation of crystallites or nuclei that grow in cones until they coalesce to form a continuous layer.

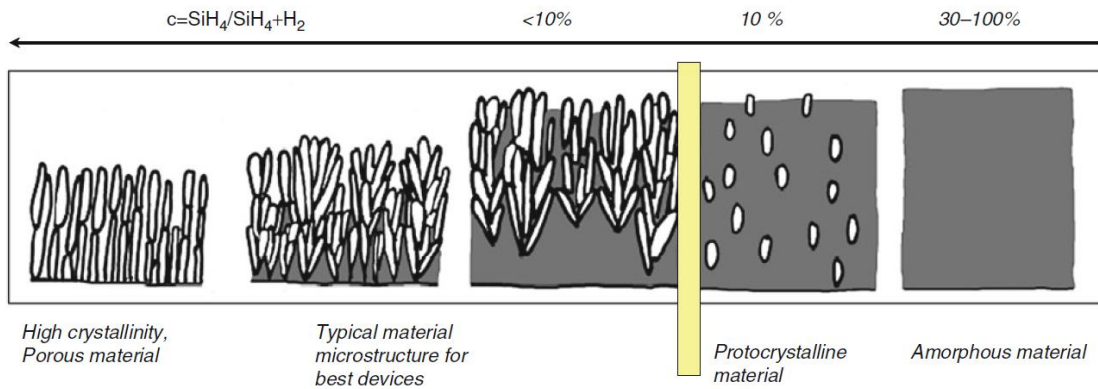


**Figure 1.10** Effect of silane dilution on the microstructure of thin-film Si material. Nanocrystallites are represented in white while the amorphous tissue is in gray. [61]

Fig. 1.11 presents a typical Transmission Electron Microscope (TEM) image of a  $\mu\text{-Si}$  layer with its a-Si incubation layer, demonstrating the morphology resulting from  $\mu\text{-Si}$  growth [61-63]. In general, one can say that for any silane dilution, the resulting  $\mu\text{-Si}$  film consists of a mixture of grains (or nanocrystals), amorphous tissue, and voids, and the surface of the layer is relatively rough compared to a-Si:H.

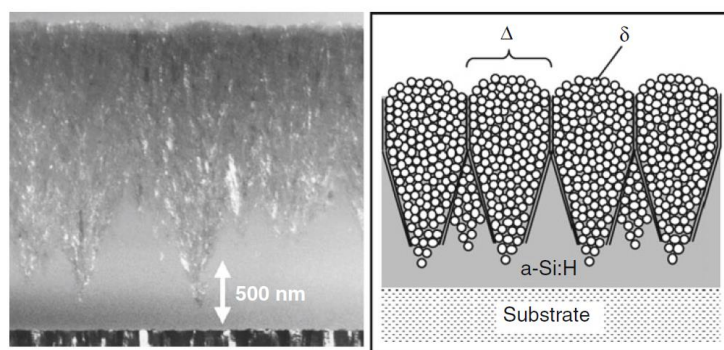


**Figure 1.11** Dark field TEM image of a typical  $\mu\text{-Si}$  layer having 500 nm of a-Si incubation layer (left) and its schematic representation (right).  $\delta$  represents nanocrystals and  $\Delta$  the conical structure [64].

It has furthermore been demonstrated that not only the silane concentration in the gas mixture controls the crystallinity of the film, but also the silane concentration in the plasma [65], as well as the substrate material [66]. Ions also have a crucial role in determining the nature of the film, as they enhance the surface diffusion of plasma species (which favors crystallinity) at low energy [67], but destroy the crystallinity (or cause renucleation within existing crystals) when their energy becomes too high.

Due to its simplicity and material quality, the  $\text{SiH}_4/\text{H}_2$  plasma chemistry is the most common one used to grow microcrystalline silicon. However, other precursor mixtures have been explored with success for the same purpose, notably the  $\text{SiF}_4/\text{H}_2$  plasma chemistry.

In 1978, silicon thin film deposition from a  $\text{SiF}_4/\text{H}_2$  plasma chemistry was demonstrated by the S. Ovshinsky and A. Madan group [68, 69]. The films grown were an amorphous Si-F-H alloy with a low density of states and high photoconductivity, essential properties for electronic applications. This same chemistry can also produce  $\mu\text{-Si}$  thin films on glass substrates, at higher hydrogen flows compared to a-Si deposition, and at a substrate temperature lower than  $300^\circ\text{C}$  [70]. Later on, G. Bruno, P. Capezzuto, and G. Cicala, studied

the chemical processes of a-Si growth in an RF-PECVD system using a SiF<sub>4</sub>/H<sub>2</sub> gas mixture [71]. Afterwards, this same group studied the deposition of μc-Si films from a similar SiF<sub>4</sub>/H<sub>2</sub>/He gas mixture [72]. They suggested a phenomenological model of the growth based on deposition/etching competition. Deposition of μc-Si is activated by SiF<sub>x</sub> radicals and hydrogen atoms while a-Si etching results from F atoms removing the silicon. The growth is described assuming F will selectively etch the a-Si phase, promoting microcrystalline growth. From SiF<sub>2</sub>, H, and F density (corresponding to their emitting excited states obtained from OES data), they showed that by controlling the plasma process, μc-Si deposition can be achieved. A much higher deposition rate than etching rate mainly yields the amorphous phase, whereas approaching the equilibrium results in the amorphous to-microcrystalline phase transition [73].

Another model for the growth of μc-Si from a Ar/SiF<sub>4</sub>/H<sub>2</sub> gas mixture has been studied in the LPICM laboratory [74]. The argon in this chemistry is considered as a catalyst for the dissociation of SiF<sub>4</sub>. To understand the reactions leading to growth, it uses kinetic equations that are correlated with the intensity of the emitting excited states of different plasma species. Equations 1.5 and 1.6 describe the dissociation of SiF<sub>4</sub> and H<sub>2</sub> gases, producing mainly SiF<sub>3</sub>, F and H. In the model, SiF<sub>3</sub> is assumed to be the growth precursor. The third equation corresponds to the reaction between hydrogen and fluorine, resulting from the above dissociation reactions, creating volatile HF molecules.



The reaction (1.7) plays a vital role in the growth, as it provides a route for the scavenging of F by atomic hydrogen. The removal of F contributes directly to the growth since fluorine is the most electronegative element and can etch wide range of materials, including silicon. In order to avoid etching, H<sub>2</sub> gas dilution is controlled in a way to have enough atomic H to scavenge all atomic F. Equation 1.8 reminds one that H<sub>2</sub> can also be effective in scavenging F, but will not participate in the nucleation process as will atomic H.

As in the  $\text{SiH}_4/\text{H}_2$  mixture,  $\text{H}_2$  flow rate determines the microstructure of the material. However, different mechanisms are involved in the case of  $\text{SiF}_4/\text{H}_2$  and are presented in Fig. 1.12. In this study, all process parameters (except  $\text{H}_2$  flow rate) were kept constant, namely Ar and  $\text{SiF}_4$  (4 sccm) flow rates, as well as power and substrate temperature. In the absence of  $\text{H}_2$ , no deposition occurs (as no F is scavenged). The deposited silicon film at  $\text{H}_2$  flow rates between 0 and 5 sccm is amorphous (when F is in excess), and at  $\text{H}_2$  flow rate greater than 5 sccm, it is microcrystalline (when  $\text{H}_2$  is in excess). The amorphous to microcrystalline silicon transition was found to be at the limit between those two regimes. It was also pointed out that the  $\mu\text{c-Si}$  deposition rate depends on RF power only when  $\text{H}_2$  is in excess to F [76] which is unlike the  $\text{SiH}_4/\text{H}_2$  plasma chemistry.

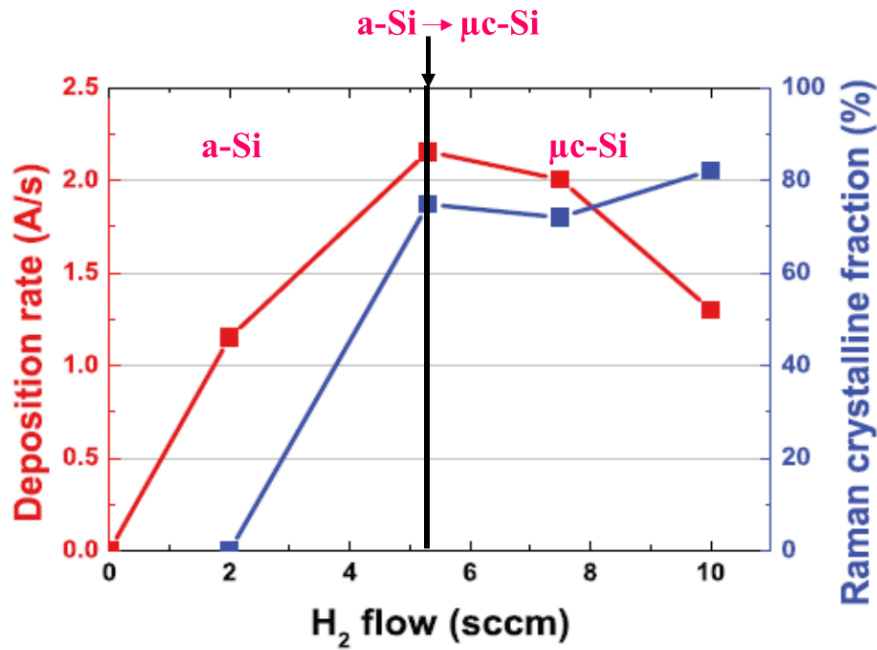


**Figure 1.12** Deposition rate and crystallinity of deposited Si layer as function of  $\text{H}_2$  flow rate. Ar and  $\text{SiF}_4$  flow rates, power, pressure and substrate temperature are constants (taken from ref [75]).

This particular plasma chemistry has been employed in our laboratory for the deposition of  $\mu\text{c-Si:H}$  and epitaxial Si both for thin film transistors TFTs [77] and photovoltaic applications [78, 79]. During the extensive research studies performed, the Ar/ $\text{SiF}_4/\text{H}_2$  plasma chemistry has occasionally displayed selectivity regarding the substrate surface in terms of deposition and morphology. For example, P. Roca i Cabarrocas et al. have demonstrated that  $\mu\text{c-Si:H}$  can be deposited selectively on Cr layers (evaporated on

glass), but only provided that the surfaces are pretreated with a  $H_2$  plasma [77]. In another study, S. Kasouit (in his doctoral thesis) was able to show that the structure of the deposited  $\mu c$ -Si:H layer is dissimilar on the same  $SiN_x$  surfaces when pre-treated with different plasmas; on Ar plasma-treated surfaces, the deposited layer consists of dense grains and is relatively smooth, while on  $N_2$  plasma-treated surfaces, the deposited layer is heterogeneous with a mixture of large agglomerates and small grains. [80]. Recently, this plasma chemistry combined with a non-sinusoidal Tailored Voltage Waveform (TVW) (Fig. 1.13) excitation source displayed electrode-selective deposition and etching [81]. The particularity of this source is in its capability of decoupling plasma density and ion flux and localizing excitation events, creating different plasma conditions near each electrode. This proved useful for Ar/SiF<sub>4</sub>/H<sub>2</sub>, as the local plasma chemistry determines whether there will be deposition or etching. Indeed, it was demonstrated that when the density of F is greater than that of H, an etching process will occur. Under the opposite conditions, at the other electrode, a deposition process occurs.

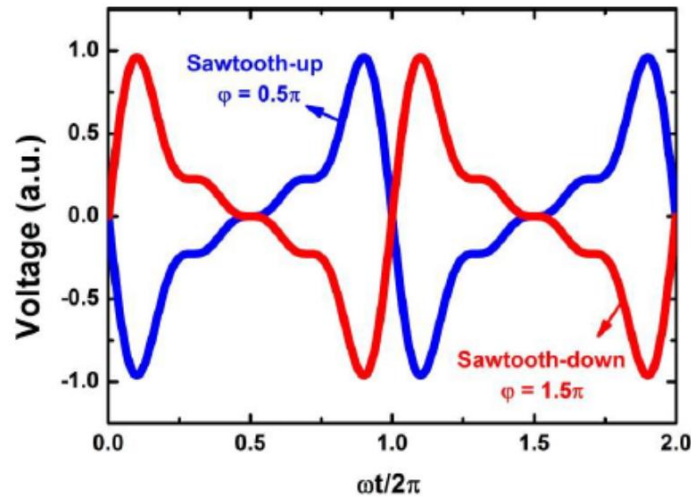


**Figure 1.13** Tailored voltage waveform corresponding to sawtooth-up and sawtooth-down [79]

In summary, microcrystalline silicon thin films deposited using an Ar/SiF<sub>4</sub>/H<sub>2</sub> plasma chemistry have shown sensitivity toward both surface treatments and local gas composition, making this chemistry a promising candidate to explore for Area Selective Deposition processes.

## **1.4 Thesis outline**

Interest in Area Selective Deposition processes is increasing, both for industry and in academic research. The aim of this thesis is to introduce a new ASD approach based on Plasma Enhanced Chemical Vapor Deposition using an Ar/SiF<sub>4</sub>/H<sub>2</sub> plasma chemistry.

The manuscript chapters are organized as follows:

- Chapter 2 describes the numerous deposition techniques used in the thesis, as well as the photolithography process used for substrate preparation. It also includes a description of the experimental PECVD tool setup, and of the main surface and plasma characterization techniques that were used.
- Chapter 3 covers experimental results for the area selective plasma enhanced chemical vapor deposition (AS-PECVD) process. The optimal plasma and experimental parameters used to achieve AS-PECVD on SiO<sub>x</sub>N<sub>y</sub> versus AlO<sub>x</sub> will be detailed for two different plasma reactors. Then, the sensitivity of the selective process to experimental conditions will be discussed. Finally, we investigate the selectivity of the process for other substrate materials.
- Chapter 4 focuses on the likely physical reasons behind our AS-PECVD process based on results from x-ray spectroscopy analyses of the surface. We also show results of plasma characterization under different conditions.
- Chapter 5 discusses the challenges that arose during sample fabrication by photolithography, followed by the solutions that were successfully deployed. This chapter concludes by presenting successful selective deposition on smaller area features.
- Chapter 6 offers a general conclusion and future perspectives for this project.



## References

- [1] [www.hitachi-hightech.com/global/products/device/semiconductor/history.html](http://www.hitachi-hightech.com/global/products/device/semiconductor/history.html)
- [2] Moore, G.E., “Cramming more components into integrated circuits,” *Electronics magazine*, (1965)
- [3] Convertino, C., Zota, C.B., Schmid, H. et al. « A hybrid III–V tunnel FET and MOSFET technology platform integrated on silicon”. *Nat Electron* 4, 162–170 (2021).
- [4] Garzón, E.; Lanuzza, M.; Taco, R.; Strangio, S. “Ultralow Voltage FinFET- Versus TFET-Based STT-MRAM Cells for IoT Applications”. *Electronics* 2021, 10, 1756.
- [5] Khatami, Yasin, and Kaustav Banerjee. "Steep subthreshold slope n-and p-type tunnel-FET devices for low-power and energy-efficient digital circuits." *IEEE transactions on electron devices* 56, no. 11 (2009): 2752-2761.
- [6] Alam, Muhammad A., Mengwei Si, and Peide D. Ye. "A critical review of recent progress on negative capacitance field-effect transistors." *Appl. Phys. Lett.* 114, 090401 (2019)
- [7] Chen, Miin-Jang, Chi-Wen Liu, and Bo-Ting Lin. "Negative Capacitance Field Effect Transistor." U.S. Patent Application 15/183,352, filed December 21, 2017.
- [8] R. Clark, K. Tapily, K.-H. Yu, T. Hakamata, S. Consiglio, D. O’Meara, C. Wajda, J. Smith, and G. Leusink, “Perspective: New process technologies required for future devices and scaling”, *APL Mater.* 6, 058203 (2018)
- [9] ASM Analyst and Investor Report. Presented at Semicon West; 2018
- [10] Ito, T., Okazaki, S. “Pushing the limits of lithography”. *Nature* 406, 1027–1031 (2000)
- [11] Totzeck, M., Ulrich, W., Göhnermeier, A. *et al.* « Pushing deep ultraviolet lithography to its limits”. *Nature Photon* 1, 629–631 (2007).
- [12] Jain, K., Willson, C. G., Lin, B. J, “Ultrafast deep UV Lithography with excimer lasers”. *IEEE Electron Device Letters*, 3(3), 53–55 (1982).
- [13] B. Wu, A. Kumar, “Extreme ultraviolet lithography: A review”, *J. Vac. Sci. Technol. B* Microelectron. Nanom. Struct. 25 (2007) 1743–1761
- [14] Léauté et al., United States Patent : 6,031,598, 1, 1–11 (2004)

- [15] J. Mulkens, M. Hanna, B. Slachter, W. Tel, M. Kubis, M. Maslow, C. Spence, V. Timoshkov, D. Run, N.W. Everygreen, P. Hillsboro, “Patterning Control Strategies for Minimum Edge Placement Error in Logic Devices”, Proc. SPIE 10145 (2017).
- [16] Adrie Mackus, Eindhoven University of Technology, Area Selective Deposition workshop 2018
- [17] G.N. Parsons and R.D. Clark, “Area Selective Deposition: Fundamentals, Applications and Future Outlook”, Chem. Mater. 32, 4920 (2020).
- [18] M. Jenkins, D.Z. Austin, J.F. Conley, J. Fan, C.H. de Groot, L. Jiang, Y. Fan, R. Ali, G. Ghosh, M. Orlowski, and S.W. King, “Review—Beyond the Highs and Lows: A Perspective on the Future of Dielectrics Research for Nanoelectronic Devices”. ECS J. Solid State Sci. Technol. 8, N159 (2019).
- [19] M.J. Hampden-Smith and T.T. Kodas, “Part 2. Overview of Selective CVD of Chemical Vapor Deposition of Metals”. Chem. Vap. Depos. 1, 39 (1995).
- [20] A.J.M. Mackus, A.A. Bol, and W.M.M. Kessels, “The use of atomic layer deposition in advanced nanopatterning”. Nanoscale 6, 10941-10960 (2014).
- [21] B.D. Joyce and J.A. Baldrey, “Selective Epitaxial Deposition of Silicon”, Nature 195, 485 (1962).
- [22] F.W. Tausch and A.G. Lapierre, “A Novel Crystal Growth Phenomenon: Single Crystal GaAs Overgrowth onto Silicon Dioxide”. J. Electrochem. Soc. 112, 706 (1965).
- [23] J.O. Carlsson, “Novel and selective vapor deposition processes”, Vacuum 41, 1077 (1990).
- [24] G. N. Parsons, “Selective deposition of silicon by plasma- enhanced chemical vapor deposition using pulsed silane flow”. Appl. Phys. Lett. 59, 2546 (1991).
- [25] S. Miyazaki, Y. Hamamoto, E. Yoshida, M. Ikeda, and M. Hirose, “Control of self-assembling formation of nanometer silicon dots by low pressure chemical vapor deposition” Thin Solid Films 369, 55 (2000).
- [26] J. Carlsson and M. Boman, “Selective deposition of tungsten—prediction of selectivity”. J. Vac. Sci. Technol. A Vacuum, Surfaces, Film. 3, 2298 (1985).
- [27] S.Y. Shapoval, O.E. Balvinskii, I. V. Malikov, A.A. Chumakov, and L.A. Niselson, “Chemical vapour deposition of tungsten layers at low substrate temperatures”. Appl. Surf. Sci. 45, 257 (1990).

- [28] D.A. Mantell, "Surface mechanisms in aluminum chemical vapor deposition", *J. Vac. Sci. Technol. A Vacuum, Surfaces, Film.* 9, 1045 (1991).
- [29] W.L. Gladfelter, "Selective Metallization by Chemical Vapor Deposition". *Chem. Mater.* 5, 1372 (1993).
- [30] E. Mohimi, Z. V. Zhang, S. Liu, J.L. Mallek, G.S. Girolami, and J.R. Abelson, "Low temperature chemical vapor deposition of superconducting molybdenum carbonitride thin films". *J. Vac. Sci. Technol. A* 36, 041507 (2018).
- [31] Z. V. Zhang, S. Liu, G.S. Girolami, and J.R. Abelson, "Area-selective chemical vapor deposition of cobalt from dicobalt octacarbonyl: Enhancement of dielectric-dielectric selectivity by adding a coflow of NH<sub>3</sub>". *J. Vac. Sci. Technol. A* 38, 033401 (2020).
- [32] T. Suh, Y. Yang, P. Zhao, K.U. Lao, H.Y. Ko, J. Wong, R.A. Distasio, and J.R. Engstrom, "Competitive Adsorption as a Route to Area-Selective Deposition", *ACS Appl. Mater. Interfaces* 12, 9989 (2020).
- [33] Simon, A. H., et al. "Electromigration comparison of selective CVD cobalt capping with PVD Ta (N) and CVD cobalt liners on 22nm-groundrule dual-damascene Cu interconnects." 2013 IEEE International Reliability Physics Symposium (IRPS). IEEE, 2013.
- [34] J. A. Singh, N. F.W. Thissen, W. H. Kim, H. Johnson, W. M. M. Kessels, A. A. Bol, S. F. Bent, A. J. M. MacKus, "Area-Selective Atomic Layer Deposition of Metal Oxides on Noble Metals through Catalytic Oxygen Activation". *Chemistry of Materials*, 30(3), 663–670 **2018**
- [35] Stevens, Eric, et al. "Area-selective atomic layer deposition of TiN, TiO<sub>2</sub>, and HfO<sub>2</sub> on silicon nitride with inhibition on amorphous carbon." *Chemistry of Materials* 30.10 (2018): 3223-3232.
- [36] R. Chen, H. Kim, P.C. McIntyre, D.W. Porter, S.F. Bent, "Achieving area-selective atomic layer deposition on patterned substrates by selective surface modification", *Appl. Phys. Lett.* 86 (2005) 1–3.
- [37] X. Jiang, S.F. Bent, Area-selective ALD with soft lithographic methods: Using self-assembled monolayers to direct film deposition, *J. Phys. Chem. C.* 113 (2009) 17613–17625.

- [38] Yanguas-Gil, Angel, Joseph A. Libera, and Jeffrey W. Elam. "Modulation of the growth per cycle in atomic layer deposition using reversible surface functionalization." *Chemistry of Materials* 25.24 (2013): 4849-4860.
- [39] A. Mameli, M.J.M. Merckx, B. Karasulu, F. Roozeboom, W.E.M.M. Kessels, A.J.M. MacKus, Area-Selective Atomic Layer Deposition of SiO<sub>2</sub> Using Acetylacetone as a Chemoselective Inhibitor in an ABC-Type Cycle, *ACS Nano*. 11 (2017) 9303–9311.
- [40] S. Seo, et al. Reaction Mechanism of Area-Selective Atomic Layer Deposition for Al<sub>2</sub>O<sub>3</sub> Nanopatterns. *ACS Applied Materials and Interfaces*, 2017, 9(47), 41607-41617.
- [41] Bobb-Semple, D., Nardi, K. L., Draeger, N., Hausmann, D. M., & Bent, S. F. (2019). Area-selective atomic layer deposition assisted by self-assembled monolayers: a comparison of Cu, Co, W, and Ru. *Chemistry of Materials*, 31(5), 1635-1645.
- [42] Wojtecki, R., Mettry, M., Fine Nathel, N. F., Friz, A., De Silva, A., Arellano, N., & Shobha, H. (2018). Fifteen nanometer resolved patterns in selective area atomic layer deposition—defectivity reduction by monolayer design. *ACS applied materials & interfaces*, 10(44), 38630-38637.
- [43] Hinckley, A. P., Driskill, M. M., & Muscat, A. J. (2020). Dense Organosilane Monolayer Resist That Directs Highly Selective Atomic Layer Deposition. *ACS Applied Nano Materials*, 3(4), 3185-3194.
- [44] Soethoudt, J., Tomczak, Y., Meynaerts, B., Chan, B. T., & Delabie, A. (2020). Insight into Selective Surface Reactions of Dimethylamino-trimethylsilane for Area-Selective Deposition of Metal, Nitride, and Oxide. *The Journal of Physical Chemistry C*, 124(13), 7163-7173.
- [45] Elina Färm, Marianna Kemell, Mikko Ritala, and Markku Leskelä, Selective-Area Atomic Layer Deposition Using Poly(methyl methacrylate) Films as Mask Layers, *The Journal of Physical Chemistry C* **2008** 112 (40), 15791-15795
- [46] Färm, E., Kemell, M., Santala, E., Ritala, M., & Leskelä, M. Selective-area atomic layer deposition using poly(vinyl pyrrolidone) as a passivation layer. *Journal of the Electrochemical Society*, 157(1), K10-K14, (2010).

[47] Ellinger, C. R.; Nelson, S. F. Selective Area Spatial Atomic Layer Deposition of ZnO, Al<sub>2</sub>O<sub>3</sub>, and Aluminum-Doped ZnO Using Poly(vinyl Pyrrolidone). *Chem. Mater.* (2014), 26, 1514–1522.

[48] A. Haider, P. Deminskyi, T.M. Khan, H. Eren, N. Biyikli, Area-selective atomic layer deposition using an inductively coupled plasma polymerized fluorocarbon layer: A case study for metal oxides, *J. Phys. Chem. C.* 120 (2016) 26393–26401.

[49] Pattison, T. G., Hess, A. E., Arellano, N., Lanzillo, N., Nguyen, S., Bui, H., ... & Wojtecki, R. J. (2020). Surface initiated polymer thin films for the area selective deposition and etching of metal oxides. *ACS nano*, 14(4), 4276-4288.

[50] Merkx, M. J., Sandoval, T. E., Hausmann, D. M., Kessels, W. M., & Mackus, A. J. (2020). Mechanism of precursor blocking by acetylacetone inhibitor molecules during area-selective atomic layer deposition of SiO<sub>2</sub>. *Chemistry of Materials*, 32(8), 3335-3345.

[51] Vallat, R., Gassilloud, R., Salicio, O., El Hajjam, K., Molas, G., Pelissier, B., & Vallée, C. (2019). Area selective deposition of TiO<sub>2</sub> by intercalation of plasma etching cycles in PEALD process: A bottom up approach for the simplification of 3D integration scheme. *Journal of Vacuum Science & Technology A: Vacuum, Surfaces, and Films*, 37(2), 020918.

[52] R. Vallat, R. Gassilloud, O. Salicio, K. El Hajjam, G. Molas, B. Pelissier, and C. Vallée, Area selective deposition of TiO<sub>2</sub> by intercalation of plasma etching cycles in PEALD process: A bottom up approach for the simplification of 3D integration scheme, *J. Vac. Sci. Technol. A* 37, 020918 (2019)

[53] Martijn F. J. Vos, Sonali N. Chopra, Marcel A. Verheijen, John G. Ekerdt, Sumit Agarwal, Wilhelmus M. M. Kessels, and Adriaan J. M. Mackus, Area-Selective Deposition of Ruthenium by Combining Atomic Layer Deposition and Selective Etching, *Chemistry of Materials* **2019** 31 (11), 3878-3882

[54] Seung Keun Song, Holger Saare, and Gregory N. Parsons, Integrated Isothermal Atomic Layer Deposition/Atomic Layer Etching Supercycles for Area-Selective Deposition of TiO<sub>2</sub>, *Chemistry of Materials* (2019) 31 (13), 4793-4804

[55] P.B. Barna, M. Adamik, Fundamental structure forming phenomena of polycrystalline films and the structure zone models. *Thin Solid Films* 317 1998. 27–33

- [56] I. Petrov, P. B. Barna, L. Hultman, and J. E. Greene, Microstructural evolution during film growth. *Journal of Vacuum Science & Technology A* 21, S117 (2003)
- [57] O. Vetterl, F. Finger, R. Carius, P. Hapke, L. Houben, O. Kluth, A. Lambertz, A. Mück, B. Rech, H. Wagner, Intrinsic microcrystalline silicon: A new material for photovoltaics, *Sol. Energy Mater. Sol. Cells.* 62 (2000) 97–108.
- [58] Matsuda, A., & Tanaka, K. (1982). Plasma spectroscopy—glow discharge deposition of hydrogenated amorphous silicon. *Thin Solid Films*, 92(1-2), 171-187. [59] Naoshi Itabashi et al, 1990, *Jpn. J. Appl. Phys.* 29 585
- [60] J. Perrin, "Plasma and surface reactions during a-Si:H film growth". *Non. Cryst. Solids* 137–138, 639 (1991).
- [61] Wronski C.R., Wyrsh N. (2012) Silicon Solar Cells, Thin-film. In: Meyers R.A. (eds) *Encyclopedia of Sustainability Science and Technology*. Springer, New York, NY.
- [62] Vallat-Sauvain E, Shah A, Bailat J (2006) Advances in microcrystalline silicon solar cell technologies. *Wiley series in materials for electronic and optoelectronic applications*, John Wiley & Sons, Ltd, Chichester, pp 133–165
- [63] Droz C, Vallat-Sauvain E, Bailat J, Feitknecht L, Meier J, Niquille X, Shah A (2003) Electrical and microstructural characterization of microcrystalline silicon layers and solar cells. In: *Proceedings of the 3rd world conference on photovoltaic energy conversion*, Osaka, Japan, pp 1544–1547
- [64] Droz C (2003) Thin film microcrystalline silicon layers and solar cells: microstructure and electrical performances. PhD Thesis, University of Neuchâtel
- [65] Strahm B, Howling AA, Sansonnens L, Hollenstein C (2007). Plasma silane concentration as a determining factor for the transition from amorphous to microcrystalline silicon in SiH<sub>4</sub>/H<sub>2</sub> discharges. *Plasma Sources Sci Technol* 16:80–89
- [66] Ferlauto AS, Ferreira GM, Koval RJ, Pearce JM, Wronski CR, Collins RW, Al-Jassim MM, Jones KM (2002) Thickness evolution of the microstructural and optical properties of Si:H films in the amorphous-to-microcrystalline phase transition region. In: *Proceedings of 29th IEEE photovoltaic specialists conference*, New Orleans, LA, p 1076
- [67] J.K. Rath, Low temperature polycrystalline silicon: a review on deposition, physical properties and solar cell applications. *Sol. Energy Mater. Sol. Cells* 76, 431-487 (2003).

- [68] A. Madan and S. Ovshinsky, "A new amorphous silicon-based alloy for electronic applications," *Nature (London)* 276, 482–484 (1978).
- [69] A. Madan and S. R. Ovshinsky, "Properties of amorphous Si:F:H alloys," *J. Non-Cryst. Solids* 35–36(1), 171–181 (1980).
- [70] I. Shimizu, "Reactions on substrate for preparation of silicon-networks from precursors, SiFnHm(n+m<3)," *J. Non-Cryst. Solids* 97–98(1), 257–260 (1987).
- [71] G. Bruno, P. Capezzuto, and G. Cicala, "rf glow discharge of SiF<sub>4</sub>-H<sub>2</sub> mixtures: Diagnostics and modeling of the a-Si plasma deposition process," *J. Appl. Phys.* 69, 7256–7266 (1991).
- [72] G. Cicala, P. Capezzuto, and G. Bruno, Microcrystalline silicon by plasma enhanced chemical vapor deposition from silicon tetrafluoride, *J. Vac. Sci. Technol. A* 19, 515 (2001).
- [73] G. Bruno, P. Capezzuto, M. M. Giangregorio, G. V. Bianco and M. Losurdo (2009), From amorphous to microcrystalline silicon: Moving from one to the other by halogenated silicon plasma chemistry, *Philosophical Magazine*, 89:28-30, 2469-2489,
- [74] J.C. Dornstetter, B. Bruneau, P. Bulkin, E. V. Johnson, and P. Roca i Cabarrocas, Understanding the amorphous-to-microcrystalline silicon transition in SiF<sub>4</sub>/H<sub>2</sub>/Ar gas mixtures, *J. Chem. Phys.* 140, (2014).
- [75] Dornstetter, J. C., Wang, J., Bruneau, B., Johnson, E. V., & Roca i Cabarrocas, P. (2014). Material and growth mechanism studies of microcrystalline silicon deposited from SiF<sub>4</sub>/H<sub>2</sub>/Ar gas mixtures. *Canadian Journal of Physics*, 92(7/8), 740-743.
- [76] Jean-Christophe Dornstetter doctoral thesis, 2014
- [77] P.R. i Cabarrocas, S. Kasouit, B. Kalache, R. Vanderhaghen, Y. Bonnassieux, M. Elyaakoubi, and I. French, Microcrystalline silicon: An emerging material for stable thin-film transistors, *J. Soc. Inf. Disp.* 12, 3 (2004).
- [78] J.C. Dornstetter, B. Bruneau, P. Bulkin, E. V. Johnson, and P. Roca i Cabarrocas, 2014, *IEEE 40th Photovolt. Spec. Conf. PVSC 2014* 2839 (2014).
- [79] R. Leal, J.C. Dornstetter, F. Haddad, G. Poulain, J.L. Maurice, and P. Roca Cabarrocas, 2015 *IEEE 42nd Photovolt. Spec. Conf. PVSC 2015* (2015).
- [80] Samir Kasouit, "Mecanisme de croissance et transport dans le silicium microcrystallin fluore. Application aux transistors en couches minces et transfert technologique », PhD doctoral thesis, Ecole Polytechnique, 17 october 2003.

[81] J. Wang and E.V. Johnson, Electrode-selective deposition/etching processes using an SiF<sub>4</sub>/H<sub>2</sub>/Ar plasma chemistry excited by sawtooth tailored voltage waveforms, Plasma Sources Sci. Technol. 26 (2017) 01LT01





# Chapter 2

## Experimental Techniques

2.1	Sample fabrication.....	30
2.1.1	Deposition techniques used for substrates preparation .....	31
2.1.1.1	Atomic Layer Deposition .....	31
2.1.1.2	Plasma Enhanced Chemical Vapor Deposition.....	33
	a) Chemical Vapor Deposition .....	33
	b) Plasma .....	34
	c) Radio Frequency PECVD .....	35
	d) Electron cyclotron resonance PECVD .....	37
2.1.2	Patterned substrates fabrication.....	39
2.1.2.1	Photolithography steps .....	39
2.1.2.2	Etching .....	42
2.1.2.3	Photoresist removal .....	42
2.2	Experimental setup.....	43
2.2.1	ARCAM .....	43
2.2.2	ATOS .....	44
2.2.3	Ellipsometry .....	45
2.3	Sample and plasma characterization techniques .....	47
2.3.1	Atomic Force Microscopy.....	47
2.3.2	Scanning Electron Microscopy .....	49
2.3.3	Transmission Electron Microscopy.....	50
2.3.4	X-ray Photoelectron Spectroscopy.....	51
2.3.5	Contact angle measurement .....	53
	References .....	56

## 2.1 Sample fabrication

Demonstrating Area Selective Deposition (ASD) requires a particular sample design in which two different surface materials are on the same substrate. In our work, sample substrates were designed and made in two configurations, as shown schematically in Fig. 2.1. The first configuration (Configuration 1) consists of simply masking an  $\text{AlO}_x$  coated Si substrate with a piece of clean c-Si, and then depositing a silicon oxynitride layer. We used this configuration to find the optimal conditions for ASD and to study the mechanisms behind our AS-PECVD process. The second configuration (Configuration 2) uses the photolithography to pattern  $\text{AlO}_x/\text{SiO}_x\text{N}_y$  into a well-defined structure. Photolithography gives the flexibility of varying the dimensions of the growth and non-growth areas on the same substrate, while also being closer to standard wafer processing workflow.

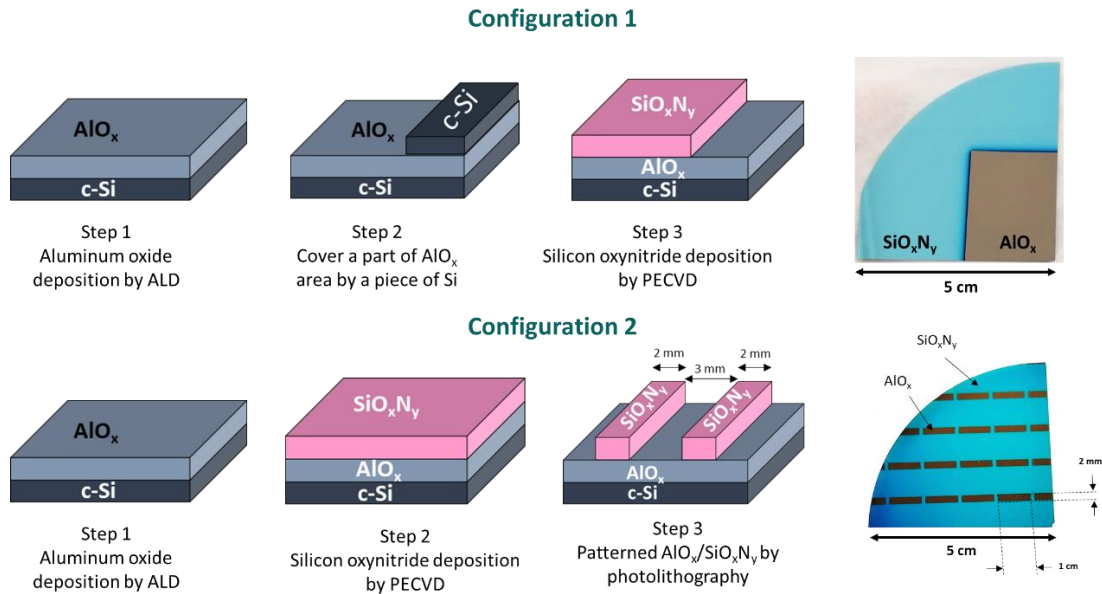


**Figure 2.1** Sample fabrication steps for two experimental configurations, with and without photolithography, along with photo of samples for each configuration

In the following, a detailed description of each fabrication step mentioned in Fig. 2.1, as well as the techniques involved in the sample preparation, will be discussed.

## **2.1.1 Deposition techniques used for substrate preparation**

### **2.1.1.1 Atomic Layer Deposition**

Atomic Layer Deposition (ALD) is a thin film deposition technique providing high quality and perfectly conformal thin layers with atomic scale control [1-4]. It was discovered and developed independently in the 1960s in Finland and the Soviet Union, and patented in the early 1970s by T. Suntola and co-workers in Finland [5, 6]. ALD technology was first developed for ZnS thin film electroluminescent (TFEL) flat panel displays. In the beginning, the name of the technology was Atomic Layer Epitaxy (ALE) where the “epitaxy” appellation refers to “on-arrangement” growth mechanism, rather than any structural relationship between crystalline deposition and crystalline substrate.

An ALD process consists of sequentially alternating exposure to a chemical precursor and to a co-reactant that will react on a surface. Each precursor is pulsed into a chamber under vacuum during a set time (from tens to hundreds of milliseconds) and then the reactor is purged (usually with N<sub>2</sub> to prevent any gas phase reactions). This is followed by a pulse of the second precursor, and subsequent new purge. Those two gaseous precursors react with the surface they face in a way to form a layer of material (close to one monolayer in thickness). Every precursor-surface interaction is considered as a half-reaction step and the two reactions are always separated with a purging step by an inert gas [7]. An example of such a process is illustrated in Fig. 2.2, which describes the deposition of Al<sub>2</sub>O<sub>3</sub> on a silicon substrate from trimethylaluminum or TMA (Al(CH<sub>3</sub>)<sub>3</sub>) and water (H<sub>2</sub>O) precursors. The first half-reaction is the chemical reaction of the TMA precursor that bonds to the surface without fully decomposing. It changes the termination of silicon to a CH<sub>3</sub> surface, enhancing its reaction ability. Afterward, the inert gas is introduced to purge and push the remaining vapor products out of the deposition chamber. The second ALD half-reaction occurs after introducing the water co-reactant, which binds with the surface leading to the removal of the methyl groups (as CH<sub>4</sub>) and deposition of the first Al<sub>2</sub>O<sub>3</sub> monolayer with a surface terminated with OH groups [8, 9]. These two reactions are repeated over and over again during each ALD cycle.

Typically, ALD half-reactions are self-limiting; the precursor reacts only with the available surface sites, and once those sites are saturated, no more deposition will occur, even if the surface is still exposed to the precursor or the co-reactant. The temperature of the surface provides conditions for the chemisorption of a single layer and for the desorption of any physisorbed molecules. Typically, only about one monolayer is formed during each half-reaction.

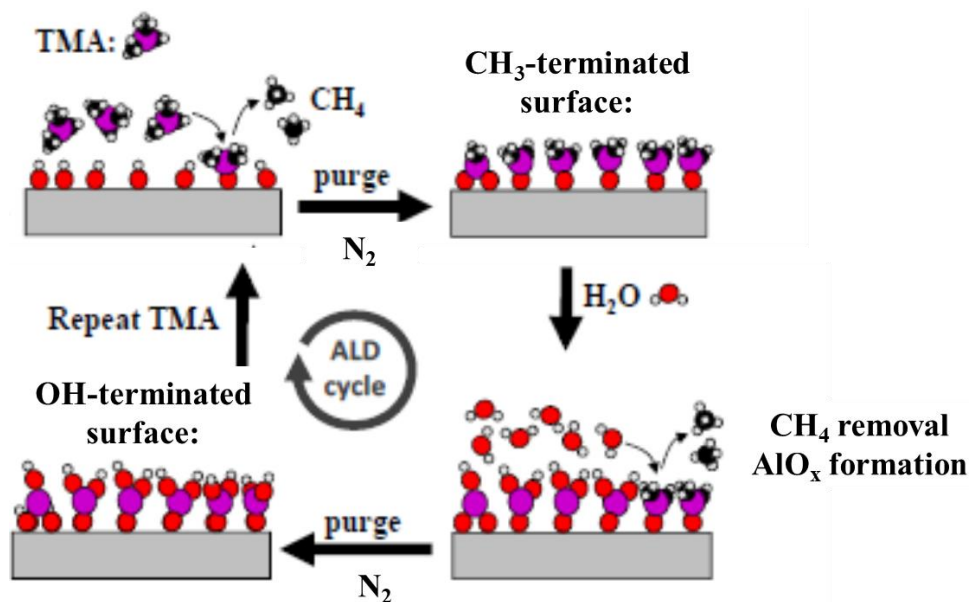


**Figure 2.2** Reactions during AlO<sub>x</sub> deposition by ALD using Trimethylaluminium (TMA) and water (H<sub>2</sub>O) [8]

ALD has numerous advantages, such as the ability to produce highly conformal coatings even over very complex motifs, atomic scale precision, and perfect reproducibility of thin film thickness by simply controlling the number of precursor pulses. As well, it is a deposition technique compatible with soft and organic substrates, in principle, though staying within acceptable ALD temperatures for these substrates may affect result quality.

In this work, we used a Picosun® R-200 ALD system (Fig. 2.3) for the deposition of about 50 nm of AlO<sub>x</sub> using TMA and water precursors. The process reactions are as described above (Fig. 2.2). The temperature was set to 200°C and the process runs for 500 cycles.



**Figure 2.3** Picosun® R-200 ALD system

## **2.1.1.2 Plasma Enhanced Chemical Vapor Deposition**

### **a) Chemical Vapor Deposition**

Chemical vapor deposition is a thin film deposition technique that relies on the chemical reactions of a gas-phase precursor with a heated substrate [10-12]. The principal steps for the mechanism of thin film growth by CVD are illustrated in Fig. 2.4. In short, the reactant gases are first introduced into the reactor. Depending on whether the deposition system is a “hot wall” or “cold wall” system, the gases are either decomposed into intermediate precursors and gaseous by-products before reaching the substrate, or they get cracked on the substrate surface. Then, the reactants adsorb onto the heated substrate surface and diffuse, searching for an energetically favored bonding site. This will lead to the nucleation, coalescence and growth of a continuous thin film. Finally, the reactants that do not react with the surface and by-product are transported away from the chamber by the gas stream.

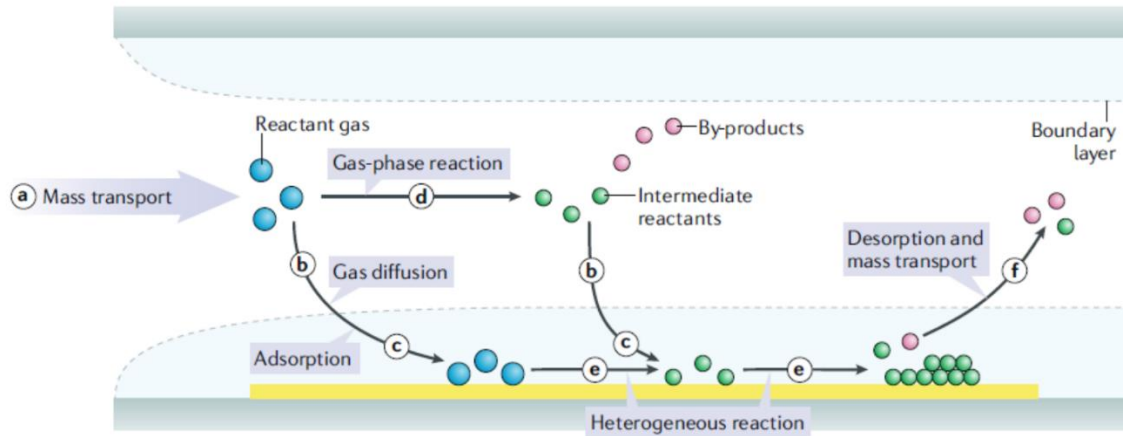


**Figure 2.4** The main important steps for a CVD process [10]

Plasma enhanced chemical vapor deposition is a variant of CVD that uses plasma as an additional energy source to generate reactive species responsible for the growth of thin film. In this case, substrate temperature can be much lower compared to that of conventional CVD.

## b) Plasma

Plasma designates a globally-neutral ionized gas consisting of neutral and charged particles, i.e. electrons and ions. It is considered as the fourth state of matter and the most abundant form of matter in the universe (stars, including our sun, are plasmas). The change from a gaseous to a plasma state can occur gradually with increasing temperature. However, it does not involve any phase transition in the thermodynamic sense, like the transition between solid, liquid and gas. Plasmas can be divided into two categories in terms of temperature: thermal plasmas, where electrons and heavy species (ions and neutrals) have the same temperature, and non-thermal or non-equilibrium plasmas, with electrons having usually a much higher temperature than either neutrals or ions. Thermal plasmas can be found in broad areas of research and manufacturing, from fusion [14] to welding, while non-thermal plasmas are widely applied in industrial research including medicine [15, 16], decontamination removal [17], aeronautics [18] and microelectronics manufacturing [19-21]. We can note, in particular, material processing, for which plasma deposition (PECVD)

and plasma etching (RIE) equipment are used to generate non-thermal plasmas in a vacuum chamber.

In practice, a non-thermal plasma is ignited by applying an electric field to a gas contained within a plasma chamber. The electric field, provided by a direct-current (DC), radio-frequency (RF) or microwave (MW) power source, will be responsible for gas breakdown and acceleration of free electrons. When those electrons gain enough energy, they can collide and excite and ionize neutral gas atoms or molecules and break them into electrons and ions and also generate other reactive species, such as radicals.

c) **Radio Frequency PECVD**

Radio frequency (RF) electric field or voltage sources are widely used in PECVD thin film deposition technologies under different configurations, such as capacitively-coupled plasmas (CCPs) and inductively coupled plasmas (ICPs). As only CCP RF systems have been employed in this work for both deposition and etching, I will describe briefly this configuration only. Therefore, in the CCP configuration, the gas flows between two electrodes; one powered with RF voltage, and a second which is grounded (as can be seen in Fig. 2.5). The matching box in the figure is used to maximize the delivered power, and the capacitor between the matching box and the powered electrode is to allow the powered electrode to take on a DC self-bias voltage.

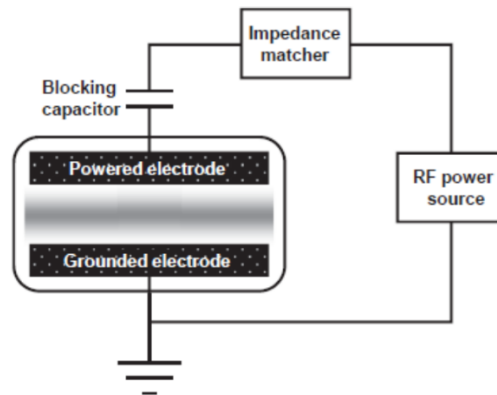


**Figure 2.5** Capacitively coupled plasma configuration [22]



The electric field created by the applied RF voltage initially accelerates any electrons present due to ionizing radiation, starting an avalanche process wherein accelerated free electrons ionize more and more gas particles. This continues until steady state is obtained, when the generation rate of new electrons is equalized by the electron losses to the walls. The particularity of RF non-thermal plasma is that [23-25]:

- (i) the electron mobility in the plasma is much greater than ion mobility due to mass difference between electron and ion
- (ii) the electron follows the electric field variation instantaneously while the ions only respond to the time-averaged electric field. This is because in radiofrequency domain (1-500 MHz), plasma frequency  $\omega$  follows the relationship:

$$\omega_{pi} \ll \omega \ll \omega_{pe}$$

Where  $\omega_{pi} = \left(\frac{n_i e^2}{m_i \epsilon_0}\right)^{1/2}$  and  $\omega_{pe} = \left(\frac{n_e e^2}{m_e \epsilon_0}\right)^{1/2}$  are ion and electron frequencies respectively;  $n_i$  and  $n_e$  are ion and electron densities respectively;  $m_i$  and  $m_e$  are ion and electron masses respectively;  $e$  is the elementary charge;  $\epsilon_0$  is the vacuum permittivity.

Under those conditions, once the plasma is ignited, electrons are lost more quickly to the walls and to the electrodes than the heavier ions, and that process creates the so-called sheath - a positive space charge region. Therefore, the slowest electrons and negative ions are confined in the center of the plasma in about equal concentration, while the positive ions at the sheath boundary are accelerated<sup>1</sup> towards the electrodes (see Fig. 2.6)<sup>1</sup>.

Usually in a CCP PECVD, the substrate is mounted on the grounded electrode. Therefore, on the substrate surface there is (1) a positive ion flux, (2) an electron flux (of electrons that have enough energy to pass the sheath potential barrier at a given point in the RF cycle) and (3) a radical species flux. By these means, a thin film may be built up from radicals and ions arriving on the substrate surface, and whose quality depends on the ion bombardment energies and the flux of other reactive species reaching the surface. However,

---

<sup>1</sup> Especially important for RIE etching, when substrate lies on smaller biased electrode and self-bias adds more energy to the ions

in the CCP configuration, the amplitude of the RF voltage determines both the ion flux and the ion bombardment energy at the substrate, it is impossible to control these two quantities independently.

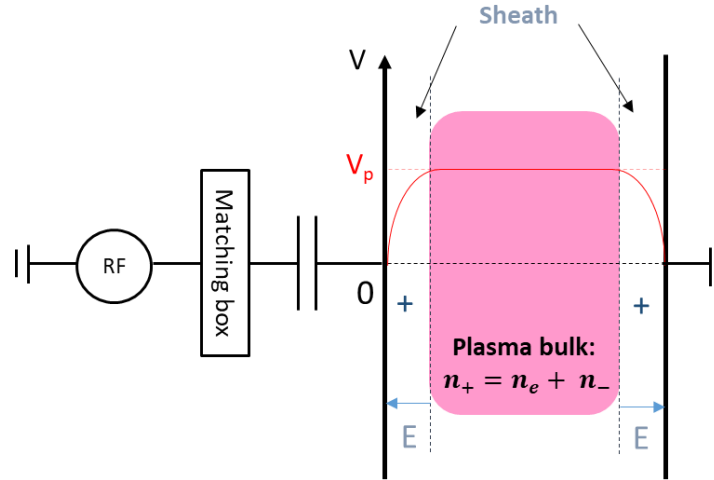


**Figure 2.6** Schematic of RF-PECVD along with voltage profile in the plasma

During my PhD, three CCP reactors were used: two RF-PECVD systems, (nicknamed ARCAM and ATOS), for the Area Selective Deposition of  $\mu\text{c-Si}$  thin films from an  $\text{Ar/SiF}_4/\text{H}_2$  gas mixture, and one reactive ion etching (RIE) system for the  $\text{SiO}_x\text{N}_y$  etching needed for pattern fabrication (configuration 2 in Fig. 2.1). A detailed description of those three systems can be found in the next sections.

#### d) Electron Cyclotron Resonance PECVD

In an Electron Cyclotron Resonance (ECR-) PECVD system, a 2.45 GHz magnetron microwave power source and either Helmholtz coils or permanent magnets are used to generate and confine a high density plasma (electron density higher than  $10^{10} \text{ cm}^{-3}$ ). The mechanism can be described as follows: under a uniform and static magnetic field  $B$ , all moving free electrons, due to the Lorentz force, will gyrate with a radius  $r_L$ :

$$r_L = \frac{m_e V_e}{eB} \quad (2.1)$$

where  $m_e$  and  $e$  are the mass and charge of the electron, respectively, and  $V_e$  is the electron velocity.

The frequency of this gyration is given by the formula (2.2):

$$f_c = \frac{e \cdot B}{2\pi \cdot m_e} \text{ (Hz)} \quad (2.2)$$

Since the frequency of the microwave electric field produced by our generators is 2.45 GHz, the source requires an 875 Gauss magnetic field to have the cyclotron rotation frequency be the same. In addition, if the mean free path is large enough (no collisions with heavy particles during several gyration cycles, which will require relatively low pressure) the electrons will be resonantly heated, gaining significant energy in the ECR conditions and generating a high density plasma as a result.

In this work, an ECR-PECVD system (nicknamed "VENUS") was used for the deposition of  $\text{SiO}_x\text{N}_y$  layers. It is a matrix-distributed (or multi-dipolar) ECR (MDECR) plasma reactor that consists of 16 microwave antennas with integrated permanent magnets, arranged in matrix configuration [26] (for more details about VENUS reactor see B. Haj Ibrahim PhD thesis [27]).

Fig. 2.7 shows a photo of the VENUS system (left hand side) as well as its schematic representation, extracted from reference [28] (right hand side). As seen in the schema, the substrate is placed on an independent electrode that can be biased with a 13.56 MHz RF power source. This allows one to decouple the plasma generation from the ion bombardment energy, to better control the energy of ions impinging on the surface.

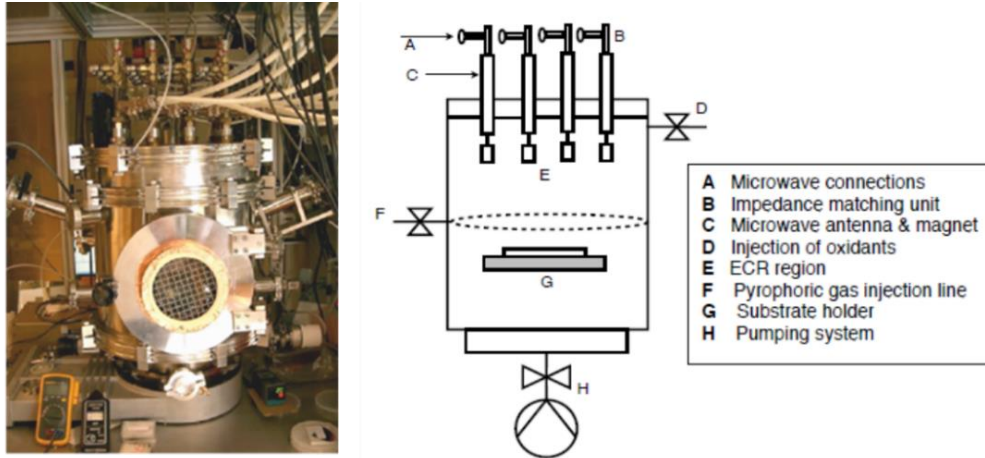


**Figure 2.7** Photo of VENUS ECR-PECVD reactor and its schematic representation, extracted from ref [28].

## 2.1.2 Patterned sample fabrication

### 2.1.2.1 Photolithography steps

As was already mentioned in the introduction, photolithography is the process of replicating the shape of a mask on a substrate through the use of a resist, (a light-sensitive polymer substance) and an ultra-violet light source. During my thesis, the fabrication of patterned samples as in Configuration 2 (Fig. 2.1) was done by me in the Thales TRT clean room, at the Ecole Polytechnique campus in Palaiseau. The fabrication requires multiple steps, starting from coating the substrate with photoresist, and finishing with the substrate having  $\text{AlO}_x/\text{SiO}_x\text{N}_y$  areas with different feature sizes (from several millimeters to 15 micrometers), depending on the chosen photomask (see Fig. 2.8). Each step in the protocol of photolithography and pattern fabrication will be further described below and in chapter 5 section 5.1.1.

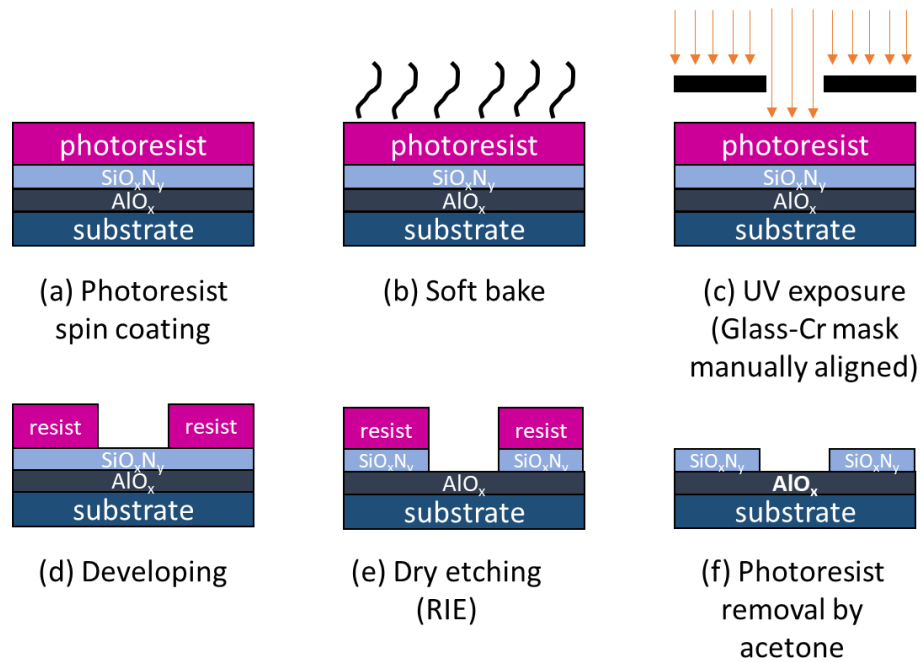


**Figure 2.8** AIO<sub>x</sub>/SiO<sub>x</sub>N<sub>y</sub> pattern fabrication steps

1) Photoresist spin coating

In most cases, the photoresist spin coating step was done after deposition of the desired layer stack. In some cases, if the mask had features of the order of ten micrometers, an additional substrate cleaning step was required. This step aimed to increase surface hydrophilicity by treating the SiO<sub>x</sub>N<sub>y</sub> surface with O<sub>2</sub> plasma, and then spin coating a primer for a better photoresist adhesion.

After surface cleaning (and possible primer application), the substrate and any layer stack was coated with photoresist solution by spin coating. In this method, illustrated in Fig. 2.9, the substrate is placed on a vacuum chuck. The resist is then applied on the surface via a pipette. The chuck accelerates and spins until the film covers whole wafer and dries. The acceleration depends on the viscosity and the desired resist thickness. In most of our cases, we chose 3000 rpm for 30 seconds to deposit 1.3 μm of SPR 700 1.0™ photoresist, which was suitable for features on the order of 2 mm large. For smaller features, the spin coating acceleration was increased to 6000 rpm for 30 seconds in order to have thinner photoresist (of 1 μm of thickness). In this manner, less developing time is needed to reduce the possibility of removing the hard photoresist.

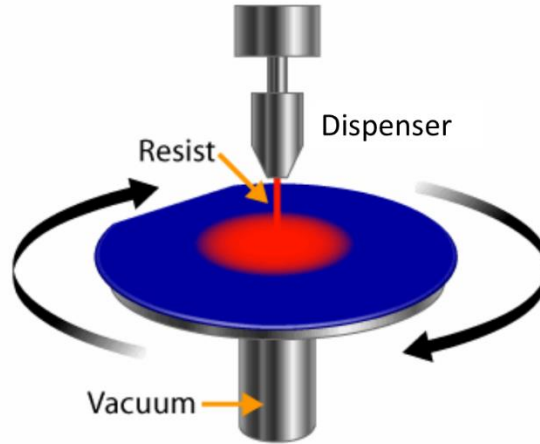


**Figure 2.9** Spin coating process extracted from ref [29]

2) Soft bake

After photoresist coating, the substrate is placed on a hot plate kept at a temperature of 110°C for 1 minute to remove any residual solvents from the photoresist. If this step is done at higher temperature or longer time, the photoresist will become too hard and impossible to be removed by standard solvent-based steps. Afterwards, the substrate is cooled down to room temperature.

3) Ultra-violet light exposure

The substrate is exposed using the 405 nm UV line of a mercury lamp in a Karl Suss MJB3 mask aligner. The photomask is made of glass with the pattern in chromium. During the exposure, the light will pass through the transparent part to the photoresist. The part covered with chromium will protect the surface underneath from UV exposure. This step is crucial for determining pattern resolution. There are two main exposure modes: (i) contact (including hard and soft contact) where the photomask is in direct contact with the surface and (ii) proximity where there is a small air gap between the mask and the substrate surface. In terms of optical resolution, it is always better to reduce the distance between the photomask and the surface to limit the light diffraction in the air gap. However, it leads to a higher risk of mask damage (mask contamination due to particles coming from the substrate or organic photoresist residue partially backed) [30]. In this work, the distance between mask and surface was controlled manually, the mask position was fixed while the substrate holder

was brought closer to the mask. This did not have any impact on the 2 mm minimum feature, but was an issue for the 15  $\mu\text{m}$  features<sup>2</sup> as we lost the resolution quality. This is likely due to the fact that the effect of light diffraction in the air gap between the dark areas of the mask and the substrate is greater for smaller features compared to larger ones.

The photoresist, by its chemical nature, is photosensitive, which means that a chemical reaction occurs between photoresist and UV light. There are two types of photoresist: positive and negative. Positive photoresists become soluble when exposed to UV light, while negative resist is hardened or cross linked when exposed to UV light. For example, in figure 2.8c, since we are using a positive photoresist, the part exposed to UV light will be soluble in the next processing step.

#### 4) Developing

The substrate is totally immersed in MICROPOSIT® MF-319® developer. The exposed areas of the positive photoresist surface were dissolved and removed while the unexposed areas remain on the surface (see Fig. 2.8d).

### **2.1.2.2 Etching**

After lithography, the removal of the part of  $\text{SiO}_x\text{N}_y$  non-covered with photoresist can be performed by wet etching or dry etching. Wet etching refers to the use of chemical solutions such as acids to remove the undesired material. Dry etching designates the use of plasma for the removal of undesired material. In my thesis, we chose a dry etching method, employing a reactive ion etching (RIE) tool (Nextral NE100) installed in Thales TRT, Palaiseau. The RIE system is a CCP plasma system with a 13.56 RF-biased substrate holder. It generates reactive species and controllable directional ion flux assisting in the removal of the material from the surface via volatile species and sputtering [31]. An  $\text{SF}_6$  plasma was used in the RIE, as it is known to etch  $\text{SiO}_x\text{N}_y$  at higher rate than  $\text{AlO}_x$  [32, 33]. Thus, once the  $\text{SiO}_x\text{N}_y$  is totally etched away, the  $\text{SF}_6$  plasma species will not etch the subsequent  $\text{AlO}_x$  area right away. The chosen conditions were based on previous studies: 30 sccm of  $\text{SF}_6$  gas

---

<sup>2</sup> This case will be detailed in chapter 5

flow, a pressure of 10 mTorr and a power of 20 Watts. I optimized the plasma etching time to that required for my sample preparation.

### **2.1.2.3 Photoresist removal**

The photoresist was stripped by acetone, followed by isopropanol rinsing to remove the remaining resist traces from the substrate (Fig 2.8f). Unfortunately, acetone and isopropanol rinsing were not enough to remove all photoresist, so an additional step was required.

All results related to the patterned substrates, including contamination resulting from the fabrication process, will be the subject of chapter 5.

## **2.2 Experimental setups**

### **2.2.1 ARCAM**

The ARCAM system pictured in Fig. 2.10 is a hot wall capacitively-coupled multi-plasma reactor with three reconfigurable deposition chambers of plasma box type [34] and a carousel capable of holding six sets of samples. Five samples of 1x1 inch can be loaded in each set. In our case, ARCAM was used to deposit microcrystalline silicon thin films using an Ar/SiF<sub>4</sub>/H<sub>2</sub> gas mixture and an inter-electrode distance of 22 mm. This reactor configuration allows one to try many conditions in one run.



**Figure 2.10** Photo of ARCAM reactor



## 2.2.2 ATOS

ATOS is a RF-CCP plasma system, like ARCAM, but with a single chamber and no “plasma-box” (Fig. 2.11). It has a load lock and equipped with an in-situ ellipsometry system (J.A Woollam RC2) that capable of measuring a full spectrum (photon energies between 0.5 and 6 eV) in one second. The interelectrode distance was fixed at 25 mm in ATOS. Each electrode is heated independently, but both were set to the same temperature for all experiments (and so "electrode temperature" indicates that of both electrodes). The substrates were always placed on the grounded electrode. An Optical Emission Spectrometer (Maya 2000 Pro compact OES spectrometer from Ocean Optics) was also mounted in the system to measure the intensity of the emission lines in different plasma conditions<sup>3</sup>. This allows one to identify the major plasma species.

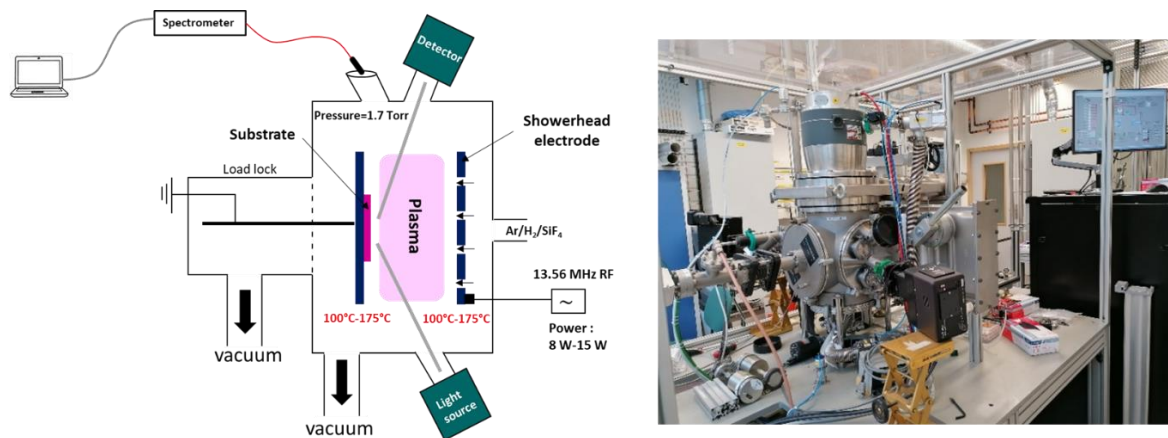


**Figure 2.11** Schematic representation of ATOS plasma reactor (on the left) and its photo (on the right)

Moreover, ATOS is a geometrically asymmetric reactor, which means that the RF electrode has a smaller surface area than the grounded electrode, once one recognizes that chamber walls are also grounded. In such a configuration, the self-bias voltage on the RF electrode is always negative. In addition, the grounded electrode (substrate holder) is bombarded by energetic ions with energies around  $eV_{DC} = eV_{RF}$  and their energy can be

<sup>3</sup> More details about OES technique are found in the appendix

controlled by the RF voltage, though it will not be independent from the power injected to the plasma.

Regarding the power source, we typically used a 13.56 MHz radio frequency generator with an automatic match box and integrated power monitor. For some cases, a variable frequency voltage source replaced the 13.56 MHz source, along with a manual matching box and power monitor to keep constant power<sup>4</sup>. By using a variable frequency source, we could change the excitation frequency, and thus vary ion bombardment energy and power independently. In fact, H. Goto et al. have shown that for a constant power,  $|V_{DC}|$  decreases with the increase of the excitation frequency, as seen in Fig. 2.12 [35], indicating a reduction of ion energy.

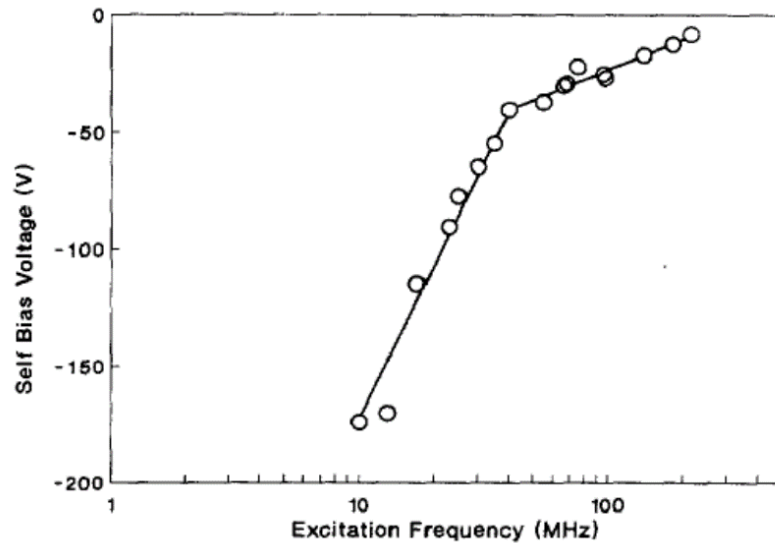


**Figure 2.12** Self-bias voltage as a function of log of excitation frequency for an Ar plasma (pressure = 7mTorr and rf power = 100W) (extracted from ref. [35])

### 2.2.3 Ellipsometry

Ellipsometry is an optical characterization technique that measures the change in polarization state of light reflected from or transmitted through a surface. An example of an

<sup>4</sup> Results are included in chapter 4

ellipsometric measurement is presented in Fig. 2.13 [36]. The elliptically polarized light is incident upon and reflected from the surface of a sample. The ellipsometer measures the change in the polarization of the reflected light, as it is dependent on the optical properties of the material and thickness of any film, if present.

The fundamental equation of ellipsometry is given by the formula (2.3):

$$\rho = \tan \Psi e^{i\Delta} = \frac{r_p}{r_s} \quad (2.3)$$

Where  $\Psi$  and  $\Delta$  are the ellipsometric angles,  $\rho$  is the reflectivity, and  $r_p$  and  $r_s$  are Fresnel reflection coefficients. [37, 38]

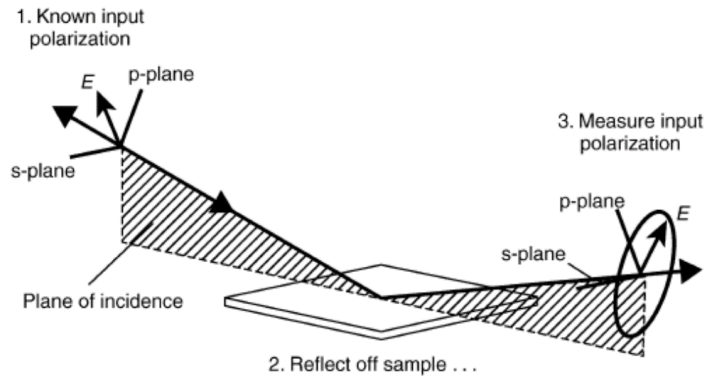


**Figure 2.13** Schematic representation of ellipsometric measurement (extracted from reference 36).

The dielectric function  $\epsilon$  and/or the refractive index  $n$  of the semi-infinite substrate can be determined directly from the ellipsometric angles, unless the roughness is significant. However, the thickness of the film on top of the substrate, as well as the optical constants of the thin film material, are determined by building a model and fitting it to the experimental spectroscopic ellipsometry (SE) data.

In this work we have used both an ex-situ spectroscopic ellipsometer *Uvisel-1* from Horiba Jobin-Yvon in the range 1.5-4.5 eV and in-situ ellipsometry (J.A Woollam, 1.2-5.0 eV photon energy range) mounted on the ATOS reactor.

For both ex-situ and in-situ ellipsometric spectra, the model was built as follows: (i) the substrate layer stack (before any plasma deposition) was measured and modelled. It typically consisted of a crystalline silicon substrate covered with a 55 nm layer of  $\text{AlO}_x$  and

a 70 nm layer of  $\text{SiO}_x\text{N}_y$ , both modeled by a classical dispersion model [39] (Fig 2.14 a). (ii) Next, the thicknesses of those layers were held constant for the modeling after plasma exposure; only the thickness and the optical constants of the deposited material are allowed to vary and be fitted. The material deposited on top of the stack is modelled with a Tauc-Lorentz (TL) dispersion function [40].

For the in-situ ellipsometric spectra, the thickness, surface roughness, and TL parameters were fitted for the layer at the end of the AS-PECVD process. The surface roughness is represented by a mixture of 50% of the deposited material and 50% of void using the Bruggeman effective medium approximation. Then, progressing backward in time from the end point, only the thickness and surface roughness were allowed to vary to achieve a fit for every other point in time (Fig. 2.14b).

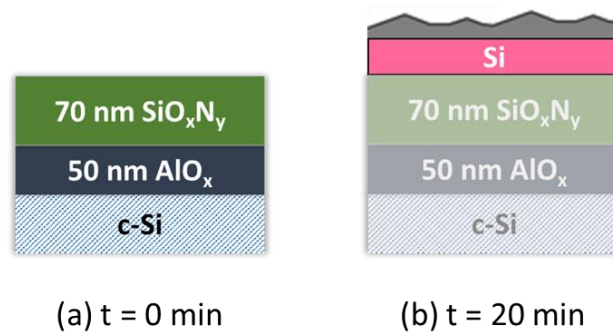


**Figure 2.14** Schema of ellipsometric model built based on the substrate layers (a) before plasma deposition (at  $t = 0$  min), and (b) at end of plasma deposition ( $t = 20$  mins), a “Tauc-Lorentz” layer, representing the Si layer and its roughness, were added to the model.

## 2.3 Sample and plasma characterization techniques

### 2.3.1 Atomic force microscopy

Atomic force microscopy is an imaging tool based on measuring the height of a sample’s surface relief by scanning a probe over the surface. It is mainly used to get access to the surface morphology (topography) and structure (crystallinity) but also can measure further sample properties at nanoscale such as conductivity and hardness.

AFM is based on the interaction between a sharp tip attached to the end of a cantilever and the surface (Fig. 2.15). A laser spot is reflected from the cantilever to a photodiode detector. During the measurement the sample is scanned along the x,y plane. As the probe is kept in proximity to the surface, the surface height variation will change the cantilever deflection resulting in the change in the laser spot position. A feedback system will change the tip height to undo this deflection, and this feedback signal is recorded as a height [41]. Different imaging modes exist:

- (i) contact mode, where the overall force is repulsive as the tip is in direct contact with the surface. This mode is usually used to image delicate structures that require sub-molecular resolution. However, the tip is easily destroyed, as it is sensitive to the surface topography.
- (ii) tapping or intermittent mode, where the cantilever oscillates from top to bottom position at or near its resonant frequency. In this manner, the lateral sample-tip forces are reduced. This mode is the most common imaging mode, as it is gentle on a wide range of materials and it is the one we used for our samples.
- (iii) Non-contact mode, where the cantilever oscillates at or above its resonant frequency. In this mode, the tip does not touch the sample, reducing its degradation, and the Van-der-Walls forces are dominant. However, the imaging resolution is low compared to the other modes.

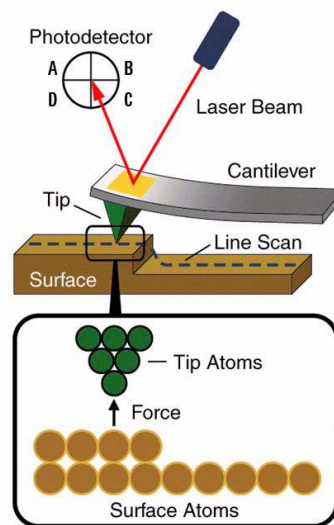


**Figure 2.15** Atomic force microscopy principle (extracted from ref. 42)

AFM applications extend to life science, material science, nanotechnology, energy, electrochemistry and much more.

Three AFM systems has been used (all in tapping mode) during my PhD work.

- Agilent Technologies 5500 scanning probe microscope in “Institut Photovoltaïque d’Ile-de-France”- IPVF. The probe is a n-doped Si tip with a resonant frequency of the cantilever between 200-400 kHz and a radius of around 10 nm. The images taken by this system are presented in chapter 3
- Digital Instruments Dimension 5000 in the LPICM. The probe is n-doped Si with a resonant frequency of the cantilever between 204-497 kHz and a radius of around 10 nm.
- Bruker Dimension Icon with ScanAsyst AFM system in the Laboratory of Mechanical Solid at Ecole Polytechnique. The probe is a n-doped Si tip with a 150 kHz cantilever resonant frequency. The AFM images in chapter 5 were taken from these last two AFM systems.

### **2.3.2 Scanning electron microscope**

Scanning Electron Microscopy (SEM) uses an electron beam to form an image of the sample surface. The electrons interact with the sample materials, generating back-scattered electrons, characteristic X-rays, secondary electrons, transmitted electrons and more (see Fig. 2.16). In the most common imaging mode, emitted secondary electrons (resulting from the inelastic interactions between the electrons and the sample) are detected by a secondary electron detector. The SEM image therefore gives information about sample surface topography and composition.

To image samples during my thesis, I used a HITACHI S-4800 microscope at 10 kV and 5  $\mu$ A (using the upper detector) and the samples were slightly tilted for a better access to the surface structure.

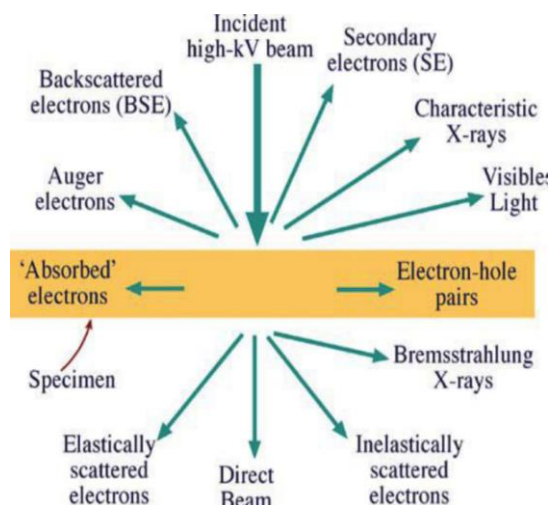


**Figure 2.16** Signals generated after interaction between electron beam with sample. [43]

### 2.3.3 Transmission electron microscopy

Transmission Electron Microscopy (TEM) uses very high electron energies (in the range of 80-300 KeV), under ultra-high vacuum ( $10^{-7}$  to  $10^{-9}$  Pa), to get access to the entire object, including the surface and any internal structures, at high resolution. It requires a special sample preparation to produce thin samples (nanometer scale thickness).

In this work, we used a High Resolution-TEM (HR-TEM)-imaging mode, which gives images with an atomic resolution. Bright and dark imaging modes were both used. In the bright mode, the electrons transmitted through the sample are detected, while in the dark mode, scattered electrons are detected [44].

TEM and energy dispersive spectroscopy (EDX) analysis were performed on two different microscopes (both FEI Titan Themis 200 TEM) either at the Center for Nanosciences and Nanotechnologies (C2N) or at the LPICM, using 300 kV and 200 kV accelerating voltages, respectively. For such analysis, a specific specimen preparation is required. Therefore, cross-section-lamellas have been prepared using a standard lift-out procedure within a Focus Ion Beam dual beam microscope (FIB, FEI-Scios Dual Beam). FIB is a system that uses ions to sputter material from a surface in a way to mill it, and then to extract a specimen from a large sample, in order to transfer it to a TEM grid for imaging

and characterization. The dual beam microscope is equipped with a gallium ion source and an electron beam. It has the advantage of combining a FIB for the milling process, and an SEM for imaging. Carbon and platinum protective layers have been deposited on top of the sample prior to the FIB milling process in order to prevent Ga ion implantation during the milling process.

For the chemical analyses, we used a Titan-Themis operating at 200 kV equipped with a Cs probe corrector and a SuperX detector that allows chemical analyses of light and heavy elements with a spatial resolution within the nm range.

### **2.3.4 X-ray photoelectron spectroscopy**

X-ray photoelectron spectroscopy (XPS) is a surface analysis technique used to get access to the elemental composition of a material (at its surface) as well as the chemical environment of those elements (character of chemical bonds and oxidation state). By these means, it allows one to identify and quantify the elemental composition of a sample under analysis, as well as quantifying the distribution of bonding arrangements. The principle of the technique is as follows: the kinetic energies of electrons ejected from a surface irradiated by a soft X-ray beam are measured. The interest of using X-rays lies in their capability to access the core electrons of the atoms on the sample surface, as they have enough energy to excite those electrons to the vacuum energy level.

XPS analysis is done under high vacuum conditions, and its principle is illustrated in Fig. 2.17a. X-rays are firstly generated by irradiating a solid anode, commonly made of Al or Mg, with a high energy electron beam, generating X-rays termed Mg  $K_{\alpha}$  (1253.6 eV) or Al  $K_{\alpha}$  (1486.6 eV). When these X-rays interact with the sample, the penetration depth in the solid is on the order of 1-10  $\mu\text{m}$  and the sampling depth is in the 10 nm range.

The interaction between x-ray photons and the surface atoms is illustrated in Fig. 2.17b. The x-ray photons are absorbed by the material atoms. An energetic photoelectron is ejected from the core shells of the surface atom to the vacuum state. The kinetic energy of



the ejected photoelectron can be defined from the Einstein photoelectric effect equation (2.4):

$$BE = h\nu - KE - \Phi_{XPS} \quad (2.4)$$

where  $KE$  is the kinetic energy of the emitted electron,  $h\nu$  is the energy of the incident photons,  $BE$  is the binding energy and  $\Phi_{XPS}$  is the spectrometer work function. The photoelectrons energy is expressed in binding energy and allows to determine the atomic nature. In XPS, the drift in the elemental binding energy is referred to as the chemical shift, and is used to identify the chemical environment in the absence of charging effect.

In practice, the kinetic energy of the emitted photoelectron is recorded by an electron energy analyzer. Knowing the binding energies of each element at the surface, the elemental composition and the chemical state of the surface can be determined and quantified<sup>5</sup>.

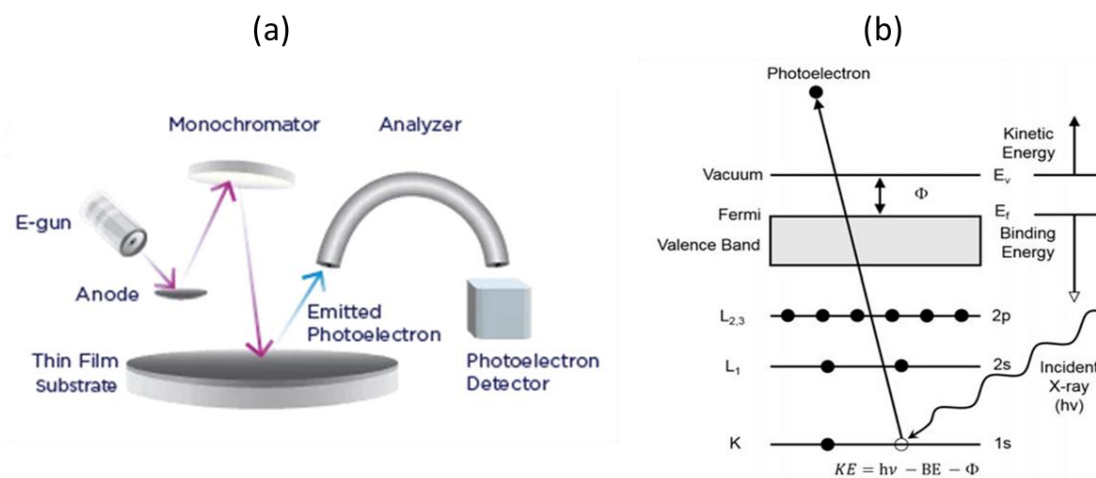


**Figure 2.17** (a) X-ray photoelectron spectroscopy instrumentation [46] and (b) illustration of photoemission process (extracted from ref [47])

A sample surface analysis relies first on an XPS survey, wherein the energy spectra of all detected photoelectron signals is collected. From the intensity of the peaks, the quantity of each type of atom in the surface layer is extracted. In order to identify the chemical environment of the element, a high energy resolution spectra showing the

<sup>5</sup> Further details about this technique can be found in ref 45.

photoelectron peak of interest is fitted and reconstructed with a Gaussian-Lorentzian convoluted functions representative of each environment.

In addition, XPS can determine the atomic composition in a multi-layer stack by depth profiling. In this case, Ar ions bombard the surface to sputter the layers during sequential measurement. After each sputtering sequence, the surface is analyzed by XPS.

In this work, XPS measurements were carried out at Institut Lavoisier, Versailles, on a ThermoFisher Scientific NEXSA spectrometer equipped with a monochromatic Al-K $\alpha$  anode (1486.6 eV) and a dual flood gun (low energy electron and ion) for AlO $_x$  and SiO $_x$ N $_y$  surface chemical analyses. Despite the use of charge compensation, a differential charging effect could not be avoided. Consequently, spectra are presented without any specific energy scale recalibration and, therefore, are interpreted comparatively. High-energy-resolution spectral windows of interest were recorded with a 400  $\mu$ m spot size. Photoelectron detection was performed using a constant analyzer energy (CAE) mode (20 eV pass energy) and a 0.1 eV energy step.

For XPS depth profiling, a ThermoFisher Scientific MAGCIS dual-beam ion gun has been used where argon ions (Ar $^+$ ) were accelerated to reach the sample with a kinetic energy of 2000 eV and at an angle of 30° from the surface normal. The thin films were irradiated over an area of 2  $\times$  2 mm $^2$ . Quantification was performed based on the Al2p, Si2p, C1s, N1s, O1s, and F1s photopeak areas after a Shirley-type background subtraction using the ThermoFisher Scientific Avantage© software and its “ALTHERM01” library as the sensitivity factor collection.

### **2.3.5 Contact angle measurement**

The contact angle is defined as the angle between the liquid-vapor interface and a solid surface at their intersection [48]. The measurement of this angle is of particular importance as it indicates the wettability of the solid (hydrophilic or hydrophobic) and can provide the value of surface energy. The surface free energy of a solid in mJ/m $^2$  and surface tension of a liquid in mN/m are the applied forces to the system to reduce its energy and

increase entropy. A high surface energy produces non-wetting of the liquid on the solid surface, while a low surface energy allows the spreading of the liquid on the solid surface (wetting the surface) [56]. Regarding the wettability, it is quite easy to determine: if the contact angle between water and the solid surface is smaller than  $90^\circ$  then the surface is hydrophilic, whereas if the water contact angle is greater than  $90^\circ$  then the surface is hydrophobic. However, determining surface energy is not as simple, and requires some calculation based on Young's equation [49], as shown in Fig. 2.18.

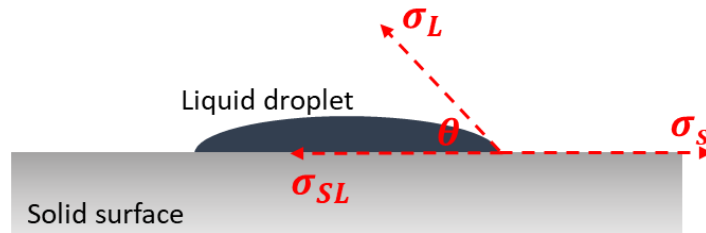


**Figure 2.18** Definition of angles and vectors of interest for contact angle measurement

This figure shows the relationship between surface energies, tension, and the contact angle, as:

$$\sigma_s = \sigma_{SL} + \sigma_L \cos \theta \quad (2.5)$$

where  $\sigma_s$  is the surface energy of the solid,  $\sigma_{SL}$  is the interfacial tension between the liquid and the solid,  $\sigma_L$  is the surface tension of the liquid and  $\theta$  is the contact angle.

There are four main theories for surface energy calculation: Zisman [50], Owens/Wendt [51], Fowkes [52] and Van Oss [53] (each theory is described in ref 54). During my PhD, an Attension® Theta Optical Tensiometer (part of the Platine platform at the Ecole Polytechnique) was used to record contact angles. The collected values are analyzed using the OneAttension software, which allows one to calculate the surface free energies. We chose the Owens/Wendt theory for the calculation, as it is simple and is the most common method for inorganic and metal surfaces. It is based on defining  $\sigma_{SL}$  as by Good's equation [55]:

$$\sigma_{SL} = \sigma_s + \sigma_L - 2(\sigma_L^D \sigma_s^D)^{1/2} - 2(\sigma_L^P \sigma_s^P)^{1/2} \quad (2.6)$$

Where  $\sigma_L^D$  and  $\sigma_S^D$  are the dispersive component of the surface tension of the liquid and the surface energy of the solid, respectively.  $\sigma_L^P$  and  $\sigma_S^P$  are the polar component of the liquid surface tension and the solid surface energy, respectively.

By combining the two equations, one can extract the values of  $\sigma_S^D$  and  $\sigma_S^P$  assuming that the surface tension of the liquid is known and can be found in the literature:

$$\frac{\sigma_L(\cos \theta + 1)}{2(\sigma_L^D)^{1/2}} = (\sigma_S^P)^{1/2} \frac{(\sigma_L^P)^{1/2}}{(\sigma_L^D)^{1/2}} + (\sigma_S^D)^{1/2} \quad (2.7)$$

in the form of  $y = mx + b$

Consequently, the methodology for measuring the surface energies of  $\text{AlO}_x$  and  $\text{SiO}_x\text{N}_y$  areas is as follows: (i) measure the contact angle of four solvents: water, ethylene glycol and n-hexane with the surfaces. (ii) input their values into the Attension© program that automatically calculate the surface free energy using liquid surface tensions listed in table 2.1 and Owens method. It is necessary that at least one of the three liquids be non-polar (having  $\sigma_L^D = 0$ ). In most applications, diiodomethane is known to be the best, but we chose n-hexane as the non-polar liquid instead, as it was readily available in the lab.

Liquids	Surface tension (mN/m)	Dispersive component (mN/m)	Polar component (mN/m)
Water	72.8	26.4	46.4
n-hexane	18.4	18.4	0
Ethylene Glycol	47.7	26.4	21.3

**Table 2.1** Surface tensions, decomposed into their dispersive and polar components, of three liquids used for the calculation of  $\text{AlO}_x$  and  $\text{SiO}_x\text{N}_y$  surface energies (from ref. 54).

## References

- [1] Pinna Nicola and Mato Knez, (EDS). "Atomic layer deposition of nanostructured materials". John Wiley & Sons, 2012.
- [2] Ritala Mikko, and Markku Leskelä. "Atomic layer deposition." Handbook of Thin Films. Academic Press, 2002. 103-159.
- [3] R.W. Johnson, A. Hultqvist, and S.F. Bent, "A brief review of atomic layer deposition: from fundamentals to applications", Materials Today 17, 236 (2014).
- [4] Leskelä, Markku, and Mikko Ritala. "Atomic layer deposition (ALD): from precursors to thin film structures." Thin solid films 409.1 (2002): 138-146.
- [5] Suntola, T. and Antson, J., Method for producing compound thin films, US Patent 4 058 430 (1977).
- [6] Esko Ahvenniemi, Andrew R. Akbashev, Saima Ali, et al., Review Article: Recommended reading list of early publications on atomic layer deposition —Outcome of the "Virtual Project on the History of ALD". J. Vac. Sci. Technol. A 35, 010801 (2017)
- [7] George, Steven M. "Atomic layer deposition: an overview." Chemical reviews 110.1 (2010): 111-131.
- [8] Q. Peng, X.Y. Sun, J.C. Spagnola, G.K. Hyde, R.J. Spontak, and G.N. Parsons, "Atomic Layer Deposition on Electrospun Polymer Fibers as a Direct Route to Al<sub>2</sub>O<sub>3</sub> Microtubes with Precise Wall Thickness Control", Nano Lett. 7, 719 (2007).
- [9] G.N. Parsons, S.M. George, and M. Knez, "Progress and future directions for atomic layer deposition and ALD-based chemistry", MRS Bull. 36, 865 (2011).
- [10] Sun, Luzhao, Guowen Yuan, Libo Gao, Jieun Yang, Manish Chhowalla, Meysam Heydari Gharahcheshmeh, Karen K. Gleason, Yong Seok Choi, Byung Hee Hong, and Zhongfan Liu. "Chemical vapour deposition." Nature Reviews Methods Primers 1, no. 1 (2021): 1-20.
- [11] Hugh O. Pierson, "Handbook of chemical vapor deposition (CVD), Principles, Technology, and Applications", Second Edition, NOYES PUBLICATIONS Park Ridge,

New Jersey, U.S.A. and WILLIAM ANDREW PUBLISHING, LLC Norwich, New York, U.S.A. (1997)

[12] Chemical Vapor Deposition: Principles and Applications, M. L. Hitchman and K. F. Jensen (Ed.), London: Academic Press, 1993.

[13] M. Ohring, Materials Science of Thin Films: Deposition and Structure (second edition), San Diego: Academic Press, 2002.

[14] Federici, Gianfranco, Charles H. Skinner, Jeffrey N. Brooks, Joseph Paul Coad, Christian Grisolia, Anthony A. Haasz, Ahmed Hassanein et al. "Plasma-material interactions in current tokamaks and their implications for next step fusion reactors." Nuclear Fusion 41, no. 12 (2001): 1967.

[15] Fridman, Gregory, Gary Friedman, Alexander Gutsol, Anatoly B. Shekhter, Victor N. Vasilets, and Alexander Fridman. "Applied plasma medicine." Plasma processes and polymers 5, no. 6 (2008): 503-533.

[16] Brullé, Laura, Marc Vandamme, Delphine Riès, Eric Martel, Eric Robert, Stéphanie Lerondel, Valérie Trichet, Serge Richard, Jean-Michel Pouvesle, and Alain Le Pape. "Effects of a non thermal plasma treatment alone or in combination with gemcitabine in a MIA PaCa2-luc orthotopic pancreatic carcinoma model." PloS one 7, no. 12 (2012): e52653.

[17] Moreau, M., N. Orange, and M. G. J. Feuilleux. "Non-thermal plasma technologies: new tools for bio-decontamination." Biotechnology advances 26, no. 6 (2008): 610-617.

[18] Moreau, Eric. "Airflow control by non-thermal plasma actuators." Journal of physics D: applied physics 40, no. 3 (2007): 605.

[19] Tarraf, Amer, J. Daleiden, S. Irmer, D. Prasai, and H. Hillmer. "Stress investigation of PECVD dielectric layers for advanced optical MEMS." Journal of Micromechanics and Microengineering 14, no. 3 (2003): 317.

[20] Battiston, G. A., R. Gerbasi, A. Gregori, M. Porchia, S. Cattarin, and G. A. Rizzi. "PECVD of amorphous TiO<sub>2</sub> thin films: effect of growth temperature and plasma gas composition." Thin solid films 371, no. 1-2 (2000): 126-131.

- [21] Babcock, Jeffrey A., Scott G. Balster, Angelo Pinto, Christoph Dirnecker, Philipp Steinmann, Reiner Jumpertz, and Badih El-Kareh. "Analog characteristics of metal-insulator-metal capacitors using PECVD nitride dielectrics." *IEEE Electron Device Letters* 22, no. 5 (2001): 230-232.
- [22] E. Despiau-Pujo, Journées du Réseau Plasmas Froids 2014, La Rochelle, France
- [23] P. Chabert and N. Braithwaite *Physics of Radio-Frequency Plasmas* 2011 (see chapter 5)
- [24] M. A. Lieberman and A. J. Lichtenberg. *Principles of plasma discharges and materials processing*. Wiley, 2005. (see pp. 11, 13, 19)
- [25] Y. Setsuhara, "Plasma Sources in Thin Film Deposition" in *Comprehensive Materials Processing*, Pages 307-324, Elsevier, 2014.
- [26] A. Lacoste, T. Lagarde, S. Béchu, Y. Arnal, J. Pelletier, *Multi-dipolar plasmas for uniform processing: physics, design and performance*, *Plasma Sources Science and Technology*, Vol. 11, pp. 407 – 412, (2002)
- [27] Bicher Haj Ibrahim. *The deposition of multilayer and gradient index thin films by Matrix Distributed Electron Cyclotron Resonance Plasma Enhanced Chemical Vapor Deposition MDECR-PECVD*. PhD in Physics. Ecole Polytechnique X, 2007.
- [28] Roelene Botha. *Deposition of thin films in a high-density low-pressure plasma system: the influence of the SiH<sub>4</sub> injection on the deposition kinetics and material properties of SiO<sub>2</sub>*. PhD in Physics. Ecole Polytechnique X, 2008.
- [29] [https://nanoscale.unl.edu/pdf/Photolithography\\_Powerpoint.pdf](https://nanoscale.unl.edu/pdf/Photolithography_Powerpoint.pdf)
- [30] S. Franssila and S. Tuomikoski, "chapter twenty two: MEMS Lithography", *Handbook of Silicon Based MEMS Materials and Technologies*, V. Lindroos, M. Tilli, A. Lehto and T. Motooka, William Andrew, 2010
- [31] Jansen, H., Gardeniers, H., de Boer, M., Elwenspoek, M. and Fluitman, J., 1996. "A survey on the reactive ion etching of silicon in microtechnology". *Journal of micromechanics and microengineering*, 6(1), p.14.

- [32] Williams, K.R. and Muller, R.S., 1996. "Etch rates for micromachining processing". *Journal of Microelectromechanical systems*, 5(4), pp.256-269.
- [33] Williams, Kirt R., Kishan Gupta, and Matthew Wasilik. "Etch rates for micromachining processing-Part II." *Journal of microelectromechanical systems* 12, no. 6 (2003): 761-778.
- [34] P. Roca i Cabarrocas, J.B. Chévrier, J. Huc, A. Lloret, J.Y. Parey, J.P.M. Schmitt, A fully automated hot-wall multiplasma-monochamber reactor for thin film deposition, *J. Vac. Sci. Technol. A Vacuum, Surfaces, Film.* 9 (1991) 2331–2341
- [35] Goto, H. H., Löwe, H. D., & Ohmi, T. (1992). Dual excitation reactive ion etcher for low energy plasma processing. *Journal of Vacuum Science & Technology A: Vacuum, Surfaces, and Films*, 10(5), 3048-3054.
- [36] J.N. Hilfiker, J.A. Woollam, "Ellipsometry" Instrumentation in *Encyclopedia of Modern Optics*, Edited by R. D. Guenther, D. G. Steel, L. Bayvel, J. E. Midwinter, Academic Press, Elsevier, 2005
- [37] [www.jawoollam.com](http://www.jawoollam.com)
- [38] Fujiwara, Hiroyuki. *Spectroscopic ellipsometry: principles and applications*. John Wiley & Sons, 2007.
- [39] [www.horiba.com](http://www.horiba.com), classical dispersion model
- [40] G.E. Jellison and F.A. Modine, "Parameterization of the optical functions of amorphous materials in the interband region", *Appl. Phys. Lett.* 69, 371 (1996).
- [41] Peter Eaton, Paul West, "Atomic force microscopy", Oxford University Press, USA, 2010
- [42] Agilent technologies 5500 scanning probe microscope, user's guide
- [43] David B. Williams and C. Barry. Carter. *Transmission Electron Microscopy*. In *Transmission Electron Microscopy A Textbook for Materials Science*, pages 3-7. Plenum press New York and London, 1996, 2009



[44] Thomas LaGrange, High Resolution Transmission Electron Microscopy (HRTEM), Doctoral Course MS-637, ÉCOLE POLYTECHNIQUE FÉDÉRALE DE LAUSANNE EPFL, April 10-12th, 2017

[45] Paul van der Heide, “X-ray Photoelectron Spectroscopy: An Introduction to Principles and Practices”, First Edition, Published 2012 by John Wiley & Sons, Inc.

[46] <https://www.novami.com/nova-technology/x-ray-photospectroscopy-xps/>

[47] Zhen Qiu, Transition Metal-Based Electrocatalysts for Alkaline Water Splitting and CO<sub>2</sub> Reduction, PhD thesis, May 2019, Uppsala University.

[48] Huhtamäki, T., Tian, X., Korhonen, J. T., and Ras, R. H. “Surface-wetting characterization using contact-angle measurements”. *Nature Protocols* 13, 1521–1538 (2018).

[49] Young, T. “An essay on the cohesion of fluids”. *Philos. Trans. R. Soc. Lond.* 95, 65–87 (1805)

[50] Zisman, William A. "Relation of the equilibrium contact angle to liquid and solid constitution.", *Contact Angle, Wettability, and Adhesion*, Chapter 1, pp 1-51, January 1 1964.

[51] Owens, Daniel K., and R. C. Wendt. "Estimation of the surface free energy of polymers." *Journal of applied polymer science* 13, no. 8 (1969): 1741-1747.

[52] Fowkes, Frederick M. "Attractive forces at interfaces." *Industrial & Engineering Chemistry* 56, no. 12 (1964): 40-52.

[53] Van Oss, C. J., R. J. Good, and M. K. Chaudhury. "The role of van der Waals forces and hydrogen bonds in “hydrophobic interactions” between biopolymers and low energy surfaces." *Journal of colloid and Interface Science* 111, no. 2 (1986): 378-390.

[54] Technical notes, TN306e, “Models for Surface Free Energy Calculation”, KRUSS©, 06/1999.

[55] Good, Robert J., and L. A. Girifalco. "A theory for estimation of surface and interfacial energies. III. Estimation of surface energies of solids from contact angle data." *The Journal of Physical Chemistry* 64, no. 5 (1960): 561-565.

[56] K.L. Mittal (ed.) *Advances in Contact Angle, Wettability and Adhesion*, volume 1 (19–48) 2013 © Scrivener Publishing LLC



# Chapter 3

## Area Selective Deposition Process

3.1	Optimal plasma parameters .....	64
3.1.1	Area selective plasma conditions in ARCAM-PECVD reactor .....	65
3.1.2	Ex-situ ellipsometry and SEM of the selective silicon deposition samples .....	66
3.1.3	Area selective plasma conditions in ATOS reactor .....	71
a)	Monitoring deposition by in-situ ellipsometry .....	73
b)	Microcrystalline nature of the deposited silicon layer .....	76
3.2	Losing selectivity .....	79
3.2.1	Effect of gas flow rates .....	80
3.2.2	Effect of plasma power and substrate electrode temperature .....	81
3.2.3	Surface contamination .....	83
3.3	AS-PECVD for different materials .....	85
3.4	Summary .....	89
	References .....	91

### **3 Area Selective Deposition process**

In this chapter, the Area Selective Deposition of  $\mu\text{-Si:H}$  using a plasma-based deposition technique will be addressed. The first section covers the experimental parameters and conditions of an  $\text{Ar/SiF}_4/\text{H}_2$  PECVD process used to achieve selective deposition on  $\text{SiO}_x\text{N}_y$  areas while preventing any deposition on adjacent  $\text{AlO}_x$  areas. These are referred as AS-PECVD conditions. These results have been published in our article in Applied Surface Science (reference [1])

For certain reasons, previously determined AS-PECVD conditions may result in silicon deposition on the non-growth area, ( $\text{AlO}_x$  in our case), leading to a loss of selectivity. Those non-selective events will be detailed in the second part of this chapter, as they may help to understand the reason behind selectivity and the loss of it.

In the third part of this chapter, we will discuss the results of our AS-PECVD process on several other materials, including metals, in order to check their potential for selective deposition.

#### **3.1 Optimal plasma parameters**

Microcrystalline silicon deposition using a fluorine-based plasma chemistry requires special caution, especially in terms of F concentration, to avoid etching. As was mentioned previously in the introduction (section 1.3), the  $\text{H}_2$  flow rate has to be above a certain value (strongly dependent on each set of experimental conditions) to promote growth. In addition, the H concentration has to be in excess to that of fluorine, so that the deposition of silicon is microcrystalline in nature.

The appropriate PECVD conditions have been determined for two custom-built Radio-Frequency PECVD (RF-PECVD) reactors in the LPICM laboratory, namely ARCAM and ATOS<sup>1</sup>. AS-PECVD conditions are slightly different between these two reactors and are

---

<sup>1</sup> Described in section 2.2.1

discussed in the following sections. The selectivity of the process was checked mainly by spectroscopic ellipsometry (ex-situ for ARCAM and in-situ for ATOS) and SEM.

### **3.1.1 Area Selective plasma conditions in ARCAM PECVD reactor**

The ARCAM reactor was used first to help identify the process parameters most suitable to achieve selectivity. The main advantage of this reactor is in its design, wherein one can load four groups of five samples (each of 1×1 inch) at a time to test many process conditions, and it can then be cleaned easily by sandblasting its stainless steel parts once the thickness of deposition on the walls leads to delamination. However, the ARCAM does not have in-situ diagnostics, nor a load lock.

Based on previous studies in the lab, the ARCAM chamber walls were coated with amorphous silicon in SiH<sub>4</sub>/H<sub>2</sub> plasma prior to Ar/SiF<sub>4</sub>/H<sub>2</sub> plasma ignition to avoid contamination. After several trials, we found plasma parameters resulting in selective μc-Si deposition on a SiO<sub>x</sub>N<sub>y</sub> area without deposition on AlO<sub>x</sub>. These parameters are summarized in Table 3.1, as determined for patterned samples (Configuration 1) on a c-Si substrate. The electrode temperatures (and that of the entire reactor) were set at 175°C for all runs, to limit the creation of powders in the chamber, and the deposition time was varied between 4 and 8 minutes.

<b>Electrode temperature</b>	<b>Ar gas flow</b>	<b>H<sub>2</sub> gas flow</b>	<b>SiF<sub>4</sub> gas flow</b>	<b>Pressure</b>	<b>Power</b>	<b>Time</b>
175°C	100 sccm	9 sccm	7 sccm	2 Torr	10 W	4-8 mins

**Table 3.1** Baseline area selective PECVD conditions in ARCAM reactor

### 3.1.2 Ex-situ ellipsometry and SEM of selective silicon deposition

Selective  $\mu\text{-Si:H}$  deposition was first confirmed by ex-situ ellipsometry and then by scanning electron microscopy. Spectroscopic ellipsometry (SE) studies rely on comparing experimentally recorded ellipsometric parameters, such as  $I_s$  and  $I_c$  ( $I_s = \sin 2\Psi \sin \Delta$  and  $I_c = \sin 2\Psi \cos \Delta$ ), with those theoretically predicted from the optical model, both before and after plasma deposition for both  $\text{SiO}_x\text{N}_y$  and  $\text{AlO}_x$  areas. The upper left part of Fig. 3.1 displays a photo of the patterned substrate after 4 minutes of plasma process under the conditions presented in table 3.1. Already, from visual observation, one can notice a change in the color on the patterned features (blue) compared to that before the deposition (violet). This fact led us to do SE measurements on three different zones of the substrate (referred to as a, b and c) to check whether the color change was due to a deposition, an etching, or some other optical artefact. A clear change in the spectra is observed only for the  $\text{SiO}_x\text{N}_y$  area (Fig 3.1a and 3.1c), while the spectrum for the  $\text{AlO}_x$  area (Fig 3.1b) remains unchanged, as closed and open symbols indicate the spectra acquired before and after the process, respectively. This indicates that the plasma did not significantly modify the structure of  $\text{AlO}_x$ , and that no etching occurred. Furthermore, in Fig. 3.1a and 3.1c, the shift of the interference peaks towards lower photon energy (indicating increase in optical thickness) clearly indicates that a deposition process has occurred on top of the  $\text{SiO}_x\text{N}_y$  area<sup>2</sup>.

In order to quantify the change in the spectra observed for the  $\text{SiO}_x\text{N}_y$  areas, the SE spectra were modelled. The post-deposition model used, unchanged, the model of the substrate stack before any plasma exposure (a crystalline silicon substrate with a 50 nm layer of  $\text{AlO}_x$  and a 200 nm layer of  $\text{SiO}_x\text{N}_y$ ). The material deposited on top of the stack was modelled with a Tauc-Lorentz dispersion function where the dielectric function  $\varepsilon$  is given by (3.1) [2]:

$$\varepsilon = \varepsilon_1 + i \varepsilon_2 \tag{3.1}$$

$$\varepsilon_2 = \begin{cases} \frac{1}{E} \cdot \frac{A E_0 C (E - E_g)^2}{(E^2 - E_0^2)^2 + C^2 E^2} & E > E_g \\ 0 & E \leq E_g \end{cases}$$

---

<sup>2</sup> Displaying SE data in this way allows one to unambiguously observe etching/deposition, without any modelling

$$\varepsilon_1 = \varepsilon_\infty + \frac{2}{\pi} P \int_{E_g}^{\infty} \frac{\xi \cdot \varepsilon_2(\xi)}{\xi^2 - E^2} d\xi$$

where  $\varepsilon_1$  and  $\varepsilon_2$  are the real and imaginary parts of the dielectric function of the material, respectively,  $E_g$  is the optical band gap,  $E$  is the photon energy,  $E_0$  is the peak transition energy,  $A$  and  $C$  are fitting parameters, and  $P$  is the Cauchy principal part of the integral. This generic dispersion curve is usually reserved for amorphous films at greater thicknesses, but can also be used for microcrystalline silicon when the layers are very thin [2, 3].

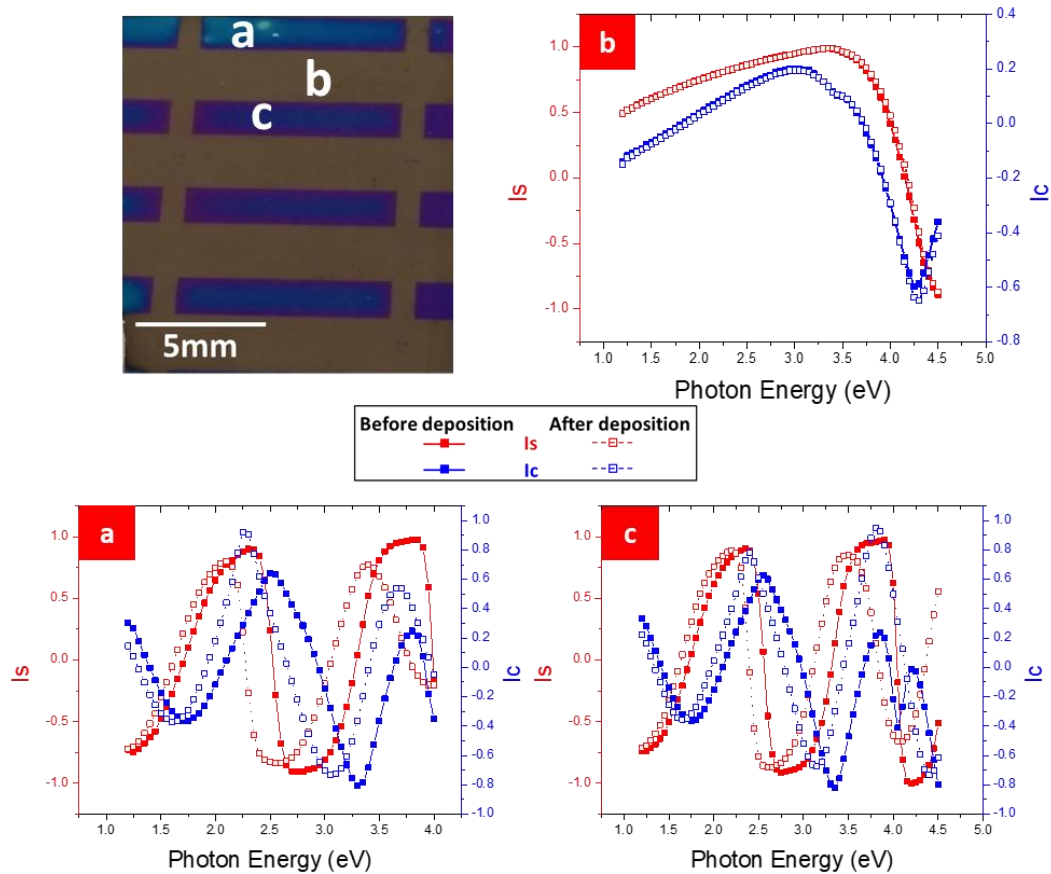


**Figure 3.1** Photo of the patterned  $\text{SiO}_x\text{N}_y / \text{AlO}_x$  sample after 4 minutes of AS-PECVD (upper left). Comparison of ellipsometric spectra for zones *a*, *b* and *c* indicated in the photo before (solid line) and after (dashed line) AS-PECVD process. Zones *a* and *c* are  $\text{SiO}_x\text{N}_y$  and zone *b* is  $\text{AlO}_x$



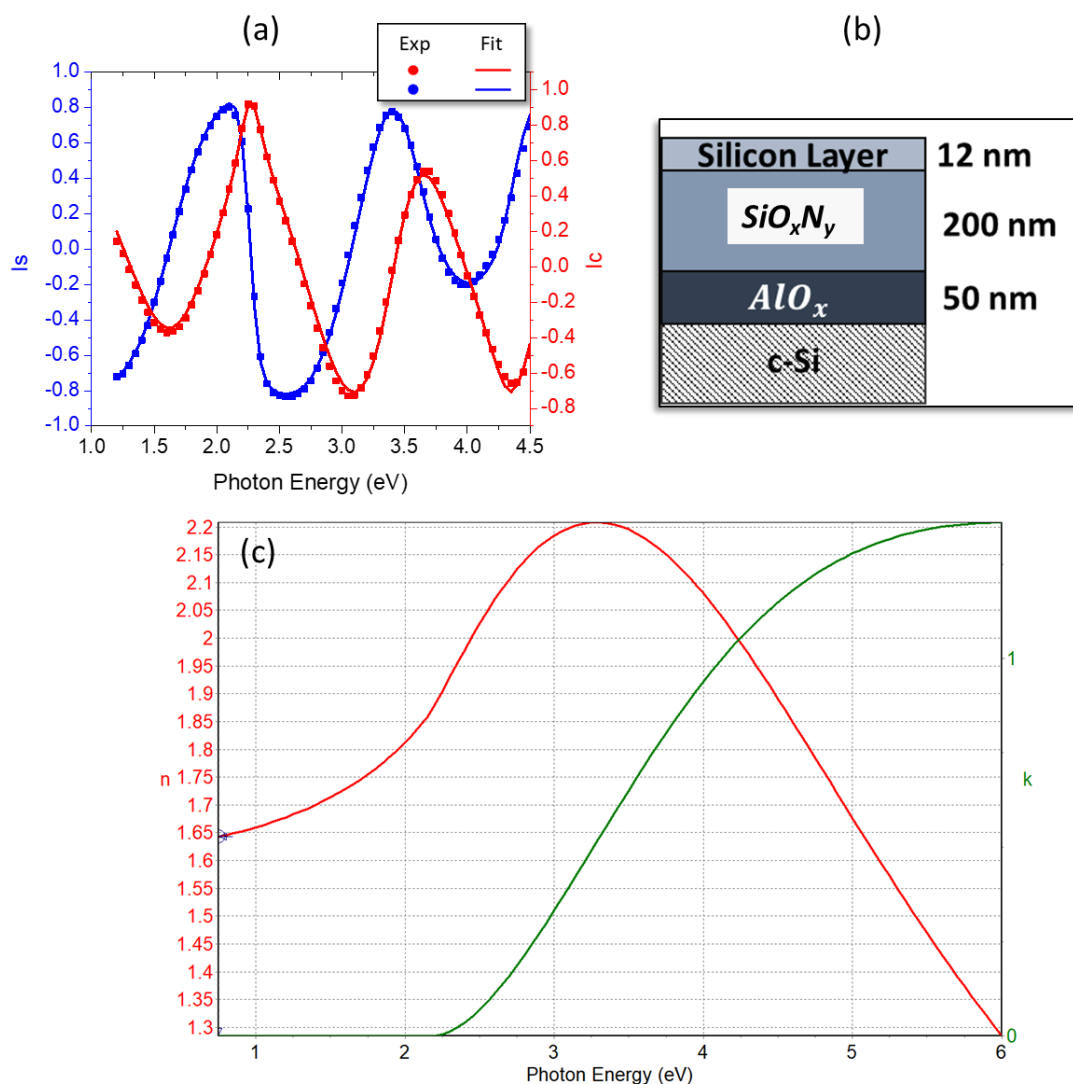


**Figure 3.2** (a) Experimental ellipsometric spectra for a silicon layer deposited on top of  $\text{SiO}_x\text{N}_y$  zone *a* represented by Blue and Red circles. Solid lines show the fitting spectra from the optical model of the substrate schematically presented on (b). (c) The optical constants (n and k) of the silicon layer given by the model

A schematic presentation of the model for a zone *a* is given in Fig. 3.2, where the  $\text{AlO}_x$  and  $\text{SiO}_x\text{N}_y$  thicknesses are fixed, while the optical constants of the silicon layer as well as the thickness are fitted. The deposited layer has a thickness of 15 nm in zone *a* and 12 nm in the zone *c*, and furthermore appears to be of rather low density, as indicated by the low refractive index of the material provided by the model.

To directly observe the nature of the growth that is occurring on the  $\text{SiO}_x\text{N}_y$ , SEM images of the  $\text{SiO}_x\text{N}_y$  and  $\text{AlO}_x$  areas of the patterned substrate were acquired and are presented in

Fig. 3.3. The  $\text{SiO}_x\text{N}_y$  area is completely covered with densely packed grains of about 60 nm in diameter. However, on the  $\text{AlO}_x$  area, there is a negligible amount of nuclei, particularly in comparison with the  $\text{SiO}_x\text{N}_y$  area. The importance of the few nuclei observed is not clear; no special care was taken to keep the substrate ultra-clean (no clean room in LPICM), so these may simply be the consequence of dust particles or other surface contamination. The morphology of the growth on the  $\text{SiO}_x\text{N}_y$  area, with a high roughness and small dense grains, is consistent with  $\mu\text{c-Si:H}$  growth.

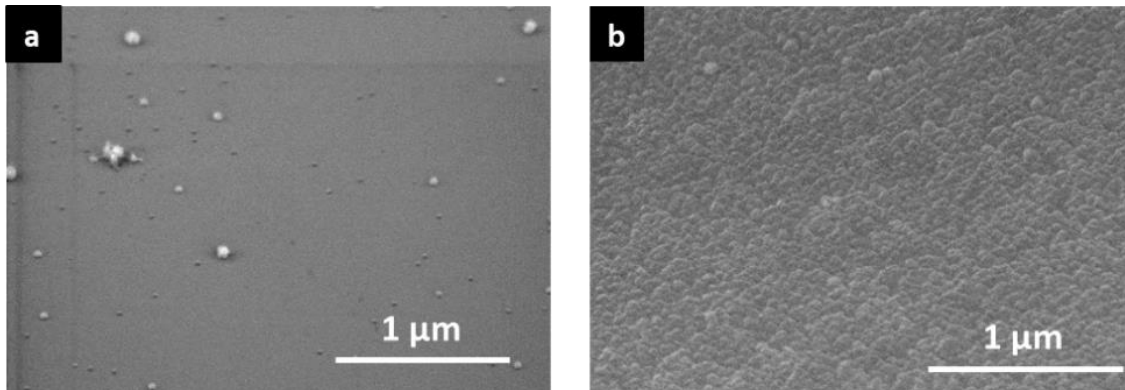


**Figure 3.3** Top view SEM images of (a)  $\text{AlO}_x$  and (b)  $\text{SiO}_x\text{N}_y$  area. Only a few sparse features are observable on the  $\text{AlO}_x$  area, while many small grains cover the  $\text{SiO}_x\text{N}_y$  area. The presence of these grains is related to the microcrystalline nature of the deposited film.

The same study was carried out on patterned substrates after 8 minutes of plasma process (see table 3.1). One can recognize from the photo in Fig. 3.4 that a loss of selectivity has occurred at the edges (deposition on both types of surface area) and that the  $\mu\text{c-Si}$  deposition is quite different between two  $\text{SiO}_x\text{N}_y$  pattern feature areas on the same sample. This can be also seen in Fig. 3.4a and 3.4c, where the shift in the spectra before and after deposition is much greater on zone **a** compared to zone **c**. While zone **a** and zone **c** are both  $\text{SiO}_x\text{N}_y$  initially, it seems that the resulting Si film is thicker on zone **a**. Acknowledging these differences, one notes that a shift in the SE spectra is only observed on  $\text{SiO}_x\text{N}_y$  areas, but not at all on the  $\text{AlO}_x$  area (similar to what was observed for the 4 minute results).

In the case of 8 minutes of deposition, particularly in zone **a**, the deposited silicon layer is denser than after 4 minutes of process, and is now 44 nm thick.

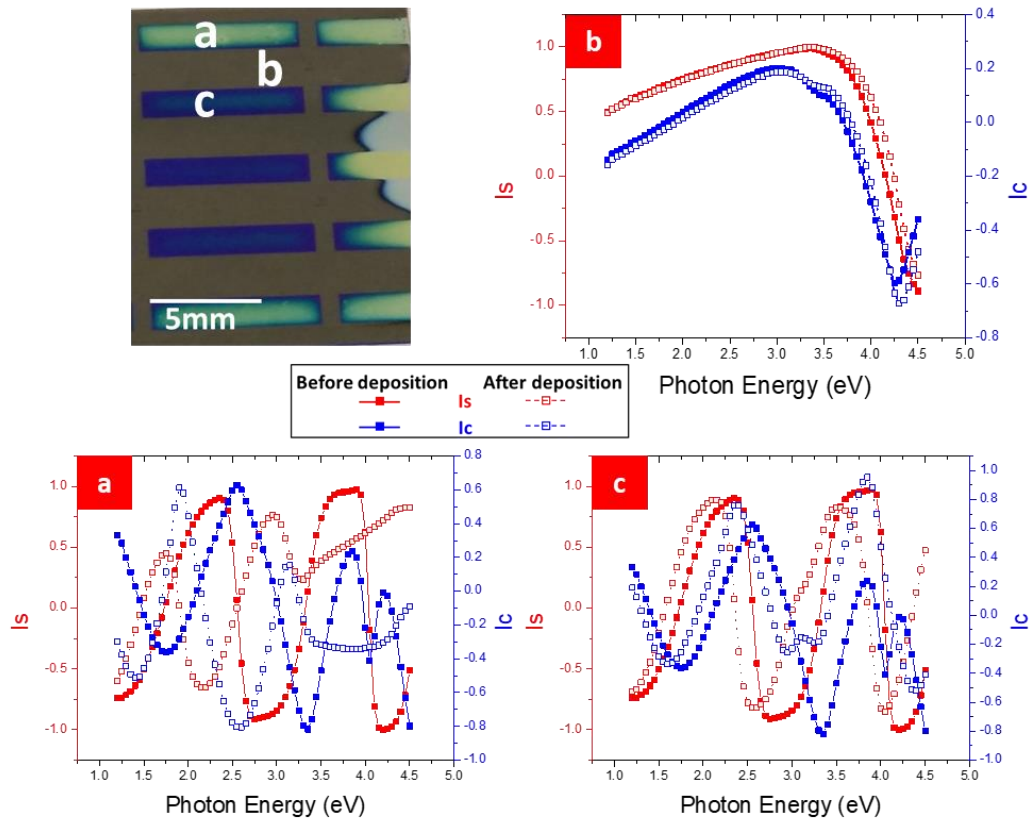


**Figure 3.4** Photo of patterned  $\text{SiO}_x\text{N}_y/\text{AlO}_x$  sample after 8 minutes of area selective PECVD process (upper left). Comparison of ellipsometric spectra for zone *a*, *b* and *c* before (solid line) and after (dashed line) AS-PECVD process. Zone *a* and *c* are  $\text{SiO}_x\text{N}_y$  and zone *b* is  $\text{AlO}_x$

Scanning Electron Microscopy (SEM) images of the  $\text{AlO}_x/\text{SiO}_x\text{N}_y$  patterned sample (Fig. 3.5), confirms a selective silicon deposition, where only some nuclei are found on  $\text{AlO}_x$  areas. However, under these growth conditions, one can also observe that on the  $\text{SiO}_x\text{N}_y$  area, the density of grains (resulting from  $\mu\text{c-Si}$  deposition) decreases gradually when getting closer to the  $\text{AlO}_x$  area.

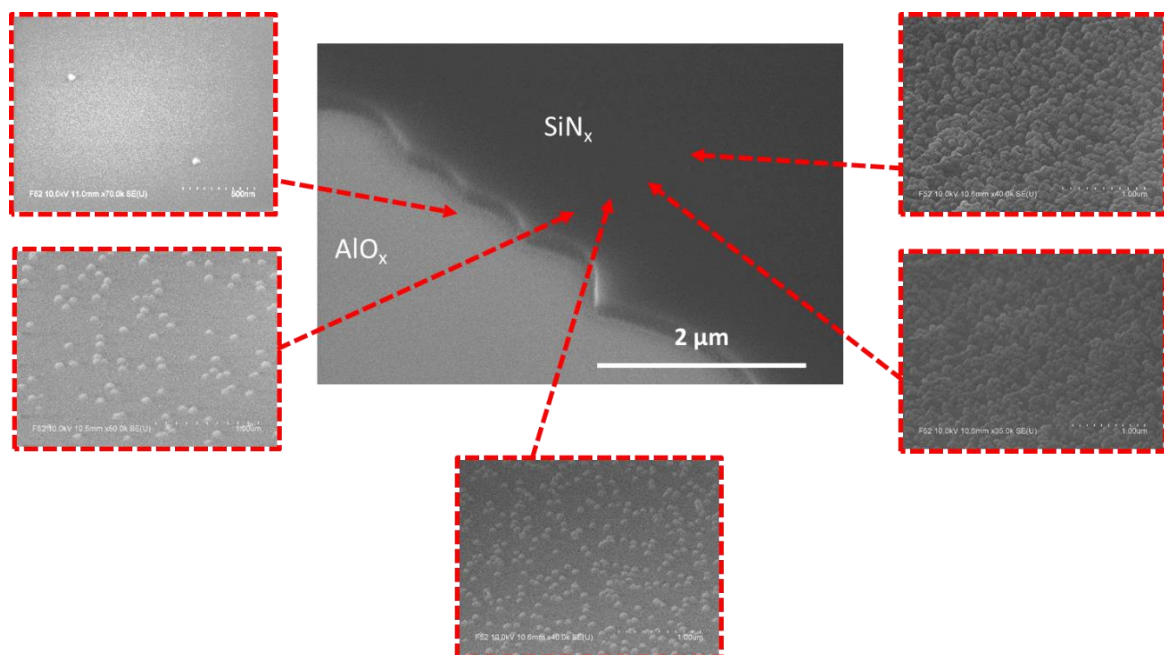


**Figure 3.5** SEM images of  $\text{AlO}_x/\text{SiO}_x\text{N}_y$  patterned sample after 8 min AS-PECVD process in ARCAM for five different areas. Grain density decreases when approaching the  $\text{AlO}_x$  area

The measurements presented above unequivocally identify the potential of an  $\text{Ar}/\text{SiF}_4/\text{H}_2$  PECVD process to provide Area Selective Deposition. The process conditions outlined in the ARCAM reactor require further refinement to enhance the uniformity of the deposition. To do so, we chose to use another RF-PECVD reactor, ATOS, which has a load lock and is equipped with a fast spectroscopic ellipsometer (RC2 from J. Woollam company), capable of measuring full spectrum (0.5 eV-6.0 eV) in one second. This was necessary to build a complete picture of the AS-PECVD process.

### 3.1.3 Area selective PECVD conditions in ATOS

For the ATOS reactor, the first set of experiments was done on non-patterned substrates, or those using Configuration 2<sup>3</sup>. No pre-coating of the walls was needed to obtain deposition, but selectivity was lost (i.e. deposition occurs on both areas) for any AS-PECVD process done after a process containing any trace of  $\text{SiH}_4$  gas. This is contrary to what was

<sup>3</sup> See section 2

obtained when developing the AS-PECVD process in the ARCAM reactor. There are, however, two main differences between these reactors: the hot walls of ARCAM (that is not the case for ATOS) and presence of load lock chamber on ATOS. These differences are likely the cause of this observed behaviour.

Based on the process parameters determined for the ARCAM reactor, table 3.2 summarizes the main experimental parameters that led to selective Si deposition on  $\text{SiO}_x\text{N}_y$  only and not on  $\text{AlO}_x$  when using Corning Glass substrates. The temperature of both electrodes was varied from  $100^\circ\text{C}$  to  $175^\circ\text{C}$  on Corning Eagle Glass substrates without really affecting the selectivity. However, upon changing the Corning Glass substrate to a crystalline silicon (c-Si) wafer, the selectivity for the same PECVD process is lost for temperatures above  $100^\circ\text{C}$ <sup>4</sup>, making our AS-PECVD process less flexible. These results are summarized in table 3.2, where **Yes** means the deposition occurs only on  $\text{SiO}_x\text{N}_y$  area, **Yes/No** means that Si grew on some spots of the  $\text{AlO}_x$  area and **No** means that deposition occurs on both  $\text{SiO}_x\text{N}_y$  and  $\text{AlO}_x$  areas.

<b>Experiment Number</b>	<b>1</b>	<b>2</b>	<b>3</b>	<b>4</b>
<b>Ar gas flow (sccm)</b>	200	200	200	200
<b>H<sub>2</sub> gas flow (sccm)</b>	20	20	20	20
<b>SiF<sub>4</sub> gas flow (sccm)</b>	14	14	14	14
<b>Pressure (Torr)</b>	1.7	1.7	1.7	1.7
<b>Power (W)</b>	10	10	10	10
<b>Electrode temperature</b>	$100^\circ\text{C}$	$125^\circ\text{C}$	$150^\circ\text{C}$	$175^\circ\text{C}$
<b>Selectivity on c-Si substrate</b>	<b>Yes</b>	<b>Yes/No</b>	<b>Yes/No</b>	<b>No</b>
<b>Selectivity on Corning Glass substrate</b>	<b>Yes</b>	<b>Yes</b>	<b>Yes</b>	<b>Yes</b>

**Table 3.2** Area selective process conditions used in ATOS-PECVD for Corning Glass substrate

---

<sup>4</sup> This case is discussed in section 3.2.2

Consequently, the optimized area selective deposition conditions henceforth used in the ATOS-PECVD reactor are the experiment conditions labelled number 1 in Table 3.2, unless otherwise indicated.

Photos of the substrate after AS-PECVD process number 4 for both Corning Glass and c-Si substrates are shown in Fig. 3.6. Microcrystalline silicon is only deposited on  $\text{SiO}_x\text{N}_y$  in case of Corning glass (CG) ( $\text{AlO}_x$  did not change color and remains transparent even after the plasma process) whereas on c-Si it grows both on  $\text{SiO}_x\text{N}_y$  and  $\text{AlO}_x$  ( $\text{AlO}_x$  becomes white instead of black).

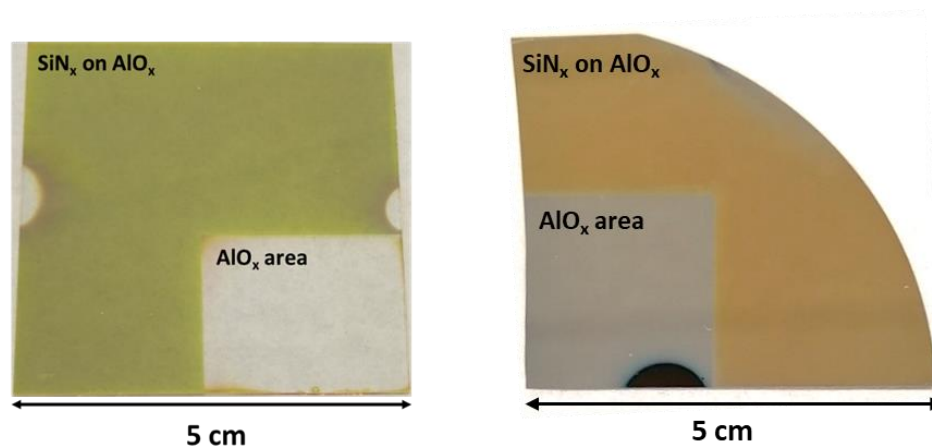


**Figure 3.6** Photo of  $\text{AlO}_x/\text{SiO}_x\text{N}_y$  in Configuration 1 on (a) Corning Glass substrate and on (b) c-Si substrate for 200/14/20 sccm of  $\text{Ar}/\text{SiF}_4/\text{H}_2$  gas flow rates, respectively, pressure of 1.7 Torr, 10 W power and electrode temperature of 175°C

In subsequent studies (and in almost all my PhD experimental work), c-Si substrates were chosen as they are easier to model in the ellipsometry analyses, and they reduce charging effects for TEM, SEM and XPS measurements.

### a) Monitoring deposition by in-situ ellipsometry

During the AS-PECVD process using the experimental parameters given in table 3.3 with an electrode temperature of 100°C (since we are using c-Si substrates), deposition was monitored by in-situ ellipsometry. Ellipsometric spectra were acquired every second and

were fitted using the COMPLETE\_EASE software in the manner explained in section 2.2.3. The underlying substrate layers were first measured and modeled prior to plasma ignition. The model comprises a silicon substrate (taken from R.C. Herzinger et al. ref. 4), an  $\text{AlO}_x$  layer (of a thickness approximately  $55 \text{ nm}^5$ ) as well as a  $\text{SiO}_x\text{N}_y$  layer (of a thickness approximately  $70 \text{ nm}$ ), which were modeled by classical dispersion model. The values determined for layer optical constants and thicknesses for the substrate layers were not allowed to vary when fitting the subsequent data during growth. As in the previous ex-situ study, the deposited silicon layer was modeled using a Tauc–Lorentz (TL) dispersion function, but in this case, a surface roughness was added to the model, represented by a mixture of 50% of  $\mu\text{-Si}$  with 50% of void using the Bruggeman effective medium approximation. The role of the roughness layer in improving the reliability of the model compared with the experimental data has been pointed out in previous studies [5, 6] and it was significant for our model as well. The TL optical constants that were obtained in the fit with the thickest layer (inset of Fig. 3.7) at the end of the deposition, are shown in terms of  $n$  and  $k$  in Fig. 3.7.

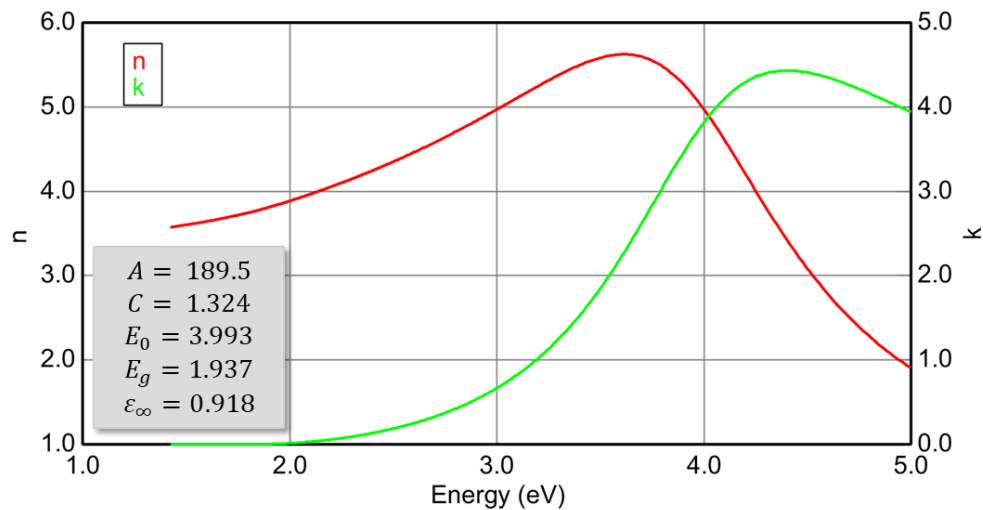


**Figure 3.7** Optical constants ( $n$  and  $k$ ) of the silicon layer deposited locally on  $\text{SiO}_x\text{N}_y$  area. In the inset, the Tauc Lorentz fitted parameters based on formula (3.1)

<sup>5</sup> The thickness slightly changes from sample to another.

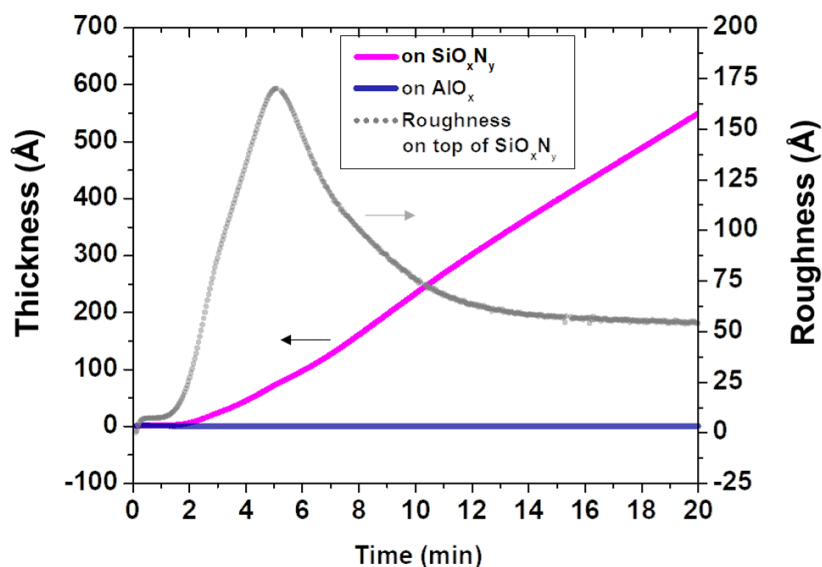


**Figure 3.8** Evolution of silicon layer thickness and surface roughness with time measured by in-situ ellipsometry and modeled on CompleteEASE software on SiO<sub>x</sub>N<sub>y</sub> and AlO<sub>x</sub> surfaces.

For the same AS-PECVD conditions, the in-situ ellipsometric spectra of both SiO<sub>x</sub>N<sub>y</sub> and AlO<sub>x</sub> surfaces were measured in separate runs (with the final spectra confirmed ex situ). Fig. 3.8 shows the thicknesses of the deposited silicon along with its corresponding roughness versus time for both areas. A 55 nm thick silicon film grows only on the SiO<sub>x</sub>N<sub>y</sub> layer, while no deposition occurs on the AlO<sub>x</sub>, despite the fact that both areas have seen the same plasma and were under the same experimental conditions. In addition, one can note a deposition delay of two minutes after starting the plasma. This effect is known as nucleation delay, and it is a critical parameter in one of the approaches to achieve AS-ALD [7]. In our case, the nucleation delay is of 2 minutes for SiO<sub>x</sub>N<sub>y</sub> while for AlO<sub>x</sub> it is far longer (more than one hour).

The optical constants of the silicon layer (Fig. 3.7) as well as the dynamics of the roughness evolution were consistent with the growth of microcrystalline silicon on SiO<sub>x</sub>N<sub>y</sub>. The values of  $n$  and  $k$  are closer to small grain polycrystalline silicon than to amorphous silicon (using values from reference [8]). Furthermore, the same roughness dynamics of the  $\mu\text{-Si}$  layer growth was seen by Fujiwara et al [9, 10]. In their studies,  $\mu\text{-Si}$  deposition on silicon oxide from SiH<sub>4</sub>/H<sub>2</sub> plasma was also characterized by in-situ spectroscopic



ellipsometry. It was found that the nucleation starts immediately on the substrate which leads to the rapid increase of the roughness. When the nuclei collide, roughness decreases and a continuous layer results.

In order to verify the microcrystalline nature of the selectively deposited silicon layer on  $\text{SiO}_x\text{N}_y$ , AFM, XRD and TEM were performed after plasma deposition process.

**b) Ex-situ characterization of the deposited silicon layer (on  $\text{SiO}_x\text{N}_y$  area)**

Atomic force microscopy (AFM) was performed on two non-patterned samples at two different stages of the growth (in the beginning and in the end of the growth) to see if the morphology of the surfaces is typical of that of microcrystalline Si. The Root Mean Square (RMS) roughnesses were calculated on  $2 \times 2 \mu\text{m}^2$   $\text{SiO}_x\text{N}_y$  area after 2 minutes growth (Fig. 3.9a) and after 20 minutes growth (Fig. 3.9b) using the AS-PECVD process. The low value of RMS even after two minutes of plasma exposure is in good agreement with the roughness value calculated from the ellipsometric model (Fig. 3.8) where the roughness values increased only after approximately 2 minutes. After 20 minutes of plasma deposition, the RMS value is 2.1 nm while the roughness from the SE data is around 5.2 nm. This difference in values can be attributed to the distinct definitions of the surface roughness for both techniques. For AFM, the RMS roughness is half of the peak-to-valley height of a "bump" on the surface [11], whilst the "effective" roughness in the COMPLETEEASE software is a 50/50 mix of the top layer material with voids [12]. For example, a similar RMS roughness for two surfaces but with different profile shapes, can yield different SE roughness as the shape of profile is important in SE characterisation [13]. In addition, the measured surface area is much bigger for SE compared to AFM, which also can somehow affect the extracted information due to small sampling effects.

Despite these discrepancies, one can consider that roughness values from AFM and ellipsometry are relatively close, and that the SE model is still a good representation of the sample.

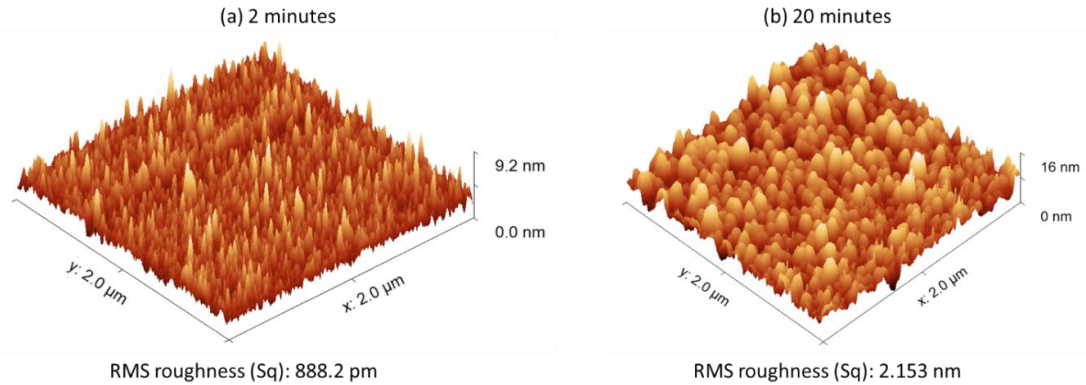


**Figure 3.9** Atomic Force Microscope images in 3D representation of  $\text{SiO}_x\text{N}_y$  areas after (a) 2 minutes and (b) 20 minutes of AS-PECVD process.

Subsequently, the structure of the selectively deposited Si layer was examined by Transmission Electron Microscopy (TEM). In Fig. 3.10 a and b, high resolution TEM (HR-TEM) images of the cross-sectional lamella of two  $\text{SiO}_x\text{N}_y$  areas are presented: one after 8 minutes and another after 20 minutes of Ar/SiF<sub>4</sub>/H<sub>2</sub> plasma exposure time in the ATOS reactor. The images clearly show the multi-layer stack on a Corning Glass substrate (Fig. 3.10a) and on a c-Si substrate (Fig. 3.10b). The silicon thin film grown on top of the  $\text{SiO}_x\text{N}_y$  area after 8 minutes of AS-PECVD process is amorphous (Fig 3.10a). However, the silicon layer deposited selectively on top of the  $\text{SiO}_x\text{N}_y$  area after 20 minutes of plasma (Fig. 3.10b) has different appearance compared to that of the Si layer in figure 3.10a. A closer analysis by Fast Fourier Transform (FFT) brings into evidence its microcrystalline structure (as was expected from SE, AFM and SEM analyses) with crystallite dimensions of few nanometers.

The TEM image in Fig. 3.10a is in contradiction with the ellipsometry data and the SEM measurements on the same sample. The in-situ ellipsometry fitting indicated that the layer deposited selectively on top of  $\text{SiO}_x\text{N}_y$  area after 8 minutes of AS-PECVD process is of microcrystalline nature. Furthermore, the SEM image on top of the same sample showed a surface consisting of small grains (similar to Fig. 3.3b) also indicating a  $\mu\text{c-Si}$  layer. To resolve this contradiction, Grazing Incidence X-Ray Diffraction (GIXRD) with a Cu-K $\alpha$ 1 x-ray source was performed in order to confirm if the selectively deposited silicon layer on top of  $\text{SiO}_x\text{N}_y$  area is of amorphous or microcrystalline nature.

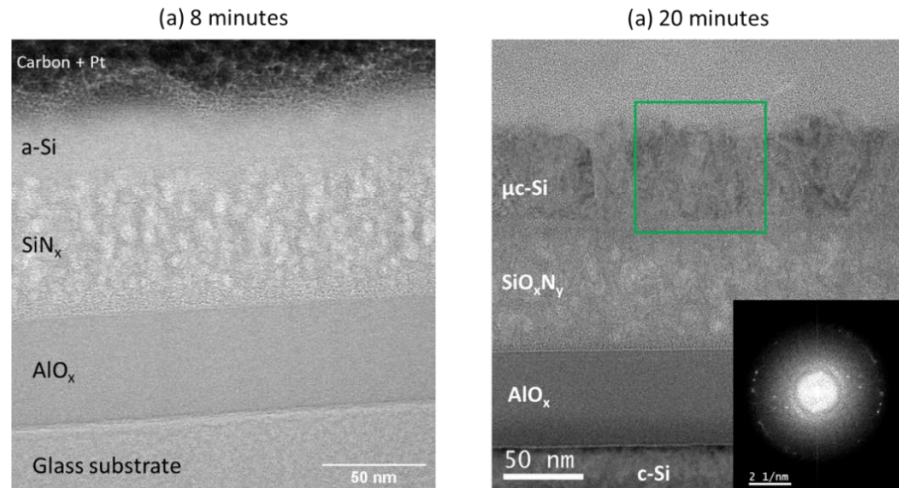


**Figure 3.10** High Resolution bright field TEM images of  $\text{SiO}_x\text{N}_y$  area after (a) 8 minutes and (b) 20 minutes of AS-PECVD. The silicon layer deposited on top of the  $\text{SiO}_x\text{N}_y$  area is amorphous in (a) but microcrystalline in (b).

Measurements were carried out on a high resolution diffractometer (*Bruker D8 Discover* in *DIFFRAX* platform at the Ecole Polytechnique) using different angles of incidence. The analyzed area was  $20 \times 20 \text{ mm}^2$ . Fig. 3.11 presents the GIXRD of  $\text{SiO}_x\text{N}_y$  area after 8 minutes of  $\text{Ar}/\text{SiF}_4/\text{H}_2$  plasma exposure recorded at a grazing angle of  $0.4^\circ$ . Under this condition, four peaks can be extracted from the spectrum, centered at  $2\theta = 21.6^\circ$ ,  $28.4^\circ$ ,  $47.3^\circ$  and  $56^\circ$ . They correspond to silicon nitride (the first peak) and silicon (for the other three) [14, 15]. The broad peak at  $21.6^\circ$  results from the amorphous  $\text{SiO}_x\text{N}_y$  material. The remaining three sharp peaks indicate the presence of nano-crystallites in the film (FWHM around  $1^\circ$ ).

Nevertheless, GIXRD analysis cannot rule out the possibility of having a mixture of amorphous silicon and Si nanocrystallites in the same surface because even a small amount of Si crystallites (compared to amorphous silicon) would give a sharp peak at  $28.4^\circ$ . Not to mention that the measurements are local (in a specific location on the substrate) and the spot is likely to be on an area mostly composed of crystallites. Consequently, we believe that after 8 minutes of plasma exposure, the layer consists of nanocrystals which can be easily amorphized by the TEM electron beam or during FIB preparation. To conserve the crystallinity of the layer under high energy electrons, a thicker layer was found to be a solution, as demonstrated in fig 3.10 b, where the  $\mu\text{c-Si}$  layer was not impacted by the

electron beam, and remains stable. Therefore, the process time was extended to 20 minutes for subsequent experiments.

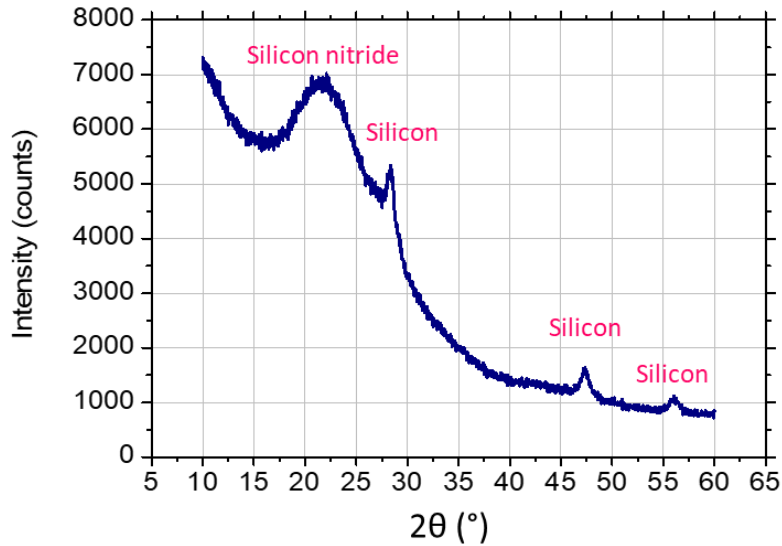


**Image 3.11** X-ray diffraction pattern of  $\text{SiO}_x\text{N}_y$  area after 8 minutes AS-PECVD on Corning Glass substrate. The detected peaks correspond to amorphous silicon nitride (broad peak) and crystallites of silicon (sharp peaks)

### 3.2 Losing selectivity

During the multiple trials to determine the optimal ASD parameters (represented in table 3.2 as "Experimental Conditions # 1"), selectivity was found to be sensitive to some plasma parameters. A small change in these parameters will result in a deposition on the non-growth  $\text{AlO}_x$  area, thus losing selectivity. In the next section we will focus specifically on  $\text{Ar/SiF}_4/\text{H}_2$  gas flow rates, plasma power and temperatures of both electrodes.

### 3.2.1 Effect of H<sub>2</sub> gas flow rate

In this study, the concentration of hydrogen in the Ar/SiF<sub>4</sub>/H<sub>2</sub> plasma chemistry is varied to check the sensitivity of the selective deposition process to this parameter. For this purpose, we only changed the H<sub>2</sub> gas flow (16, 18, 20 and 22 sccm) while keeping the rest of the AS-PECVD parameters unchanged (table 3.3). The samples were prepared in Configuration 1 and on Corning Glass substrates. One can notice from table 3.3 that a small variation in the H<sub>2</sub> flow rate affects the selectivity, and that process 3 represents the optimal selective plasma deposition conditions (corresponding to experimental conditions #1 in table 3.2).

Experiment Number	1	2	3	4
Ar gas flow (sccm)	200	200	200	200
H <sub>2</sub> gas flow (sccm)	16	18	20	22
SiF <sub>4</sub> gas flow (sccm)	14	14	14	14
Pressure (Torr)	1.7	1.7	1.7	1.7
Power (W)	10	10	10	10
Electrode temperature	175°C	175°C	175°C	175°C
Selectivity	No	No	Yes	No

**Table 3.3** Influence of H<sub>2</sub> flow rate on AS-PECVD process when using Corning Glass substrates. In the selectivity row, *Yes* refers to the case where there is deposition only on SiO<sub>x</sub>N<sub>y</sub> area and *No* indicates the case where deposition occurs on both SiO<sub>x</sub>N<sub>y</sub> and AlO<sub>x</sub> areas.

The same study was also done for substrates prepared in Configuration 1 but on **c-Si** substrates, and for electrode temperature of **100°C**. Similarly, the selectivity was lost for 16, 18 and 22 sccm of H<sub>2</sub> flow rates for constant power (10 W), pressure (1.7 Torr), electrode temperature (100°C) and Ar and SiF<sub>4</sub> gas flow rates 200 sccm and 14 sccm respectively.

Comparing our process with previously published data on Ar/SiF<sub>4</sub>/H<sub>2</sub> PECVD, selectivity in our case is determined much in the same way as the phase transition from a-Si to  $\mu$ c-Si, which is strongly dependent on the concentration of hydrogen (Fig. 1.2). This

means that the concentration of  $H_2$  in the gas phase is playing another important role in the AS-PECVD process. It does not just scavenge the fluorine atoms resulting from the dissociation of  $SiF_4$ , but also determines whether there will be deposition on the  $AlO_x$  area or not. If  $H_2$  is in great excess to F atoms, one will obtain  $\mu c$ -Si deposition on every type of surface (which means everywhere). Therefore, it appears that a small quantity of F (that does not react with H to form HF) is still needed to react with the surfaces and favor the selective deposition of  $\mu c$ -Si on  $SiO_xN_y$  area vs  $AlO_x$  area.

### **3.2.2 Effect of plasma power and electrode temperature**

Plasma power and electrode temperature were varied to check their effect on the selectivity of the deposition process. For this study, *c*-Si substrates coated with  $\sim 50$  nm of  $AlO_x$  were used, and the Ar,  $SiF_4$  and  $H_2$  gases flow rates and pressure are kept constant at 200/14/20 sccm and 1.7 Torr, respectively. Two set of experiments were done: (1) the temperature was kept constant at  $100^\circ C$  and the plasma power was changed to 5, 8, 10 and 15 Watts; and (2) the plasma power was set to 10 W, and the electrode temperature was changed from  $100^\circ C$  to  $125^\circ C$ ,  $150^\circ C$  and  $175^\circ C$ . The results can be split in terms of electrode temperature as follows:

- At  $100^\circ C$ : selective deposition of  $\mu c$ -Si on  $SiO_xN_y$  area was obtained for 5, 8 and 10 W plasma powers with no deposition on  $AlO_x$  area, while a power of 15 W causes the growth of a  $\mu c$ -Si film on both surfaces.
- At  $125^\circ C$  and  $150^\circ C$ , a plasma power of 10 W resulted in unpredictable selectivity, which depends on factors such as wall conditions and substrate storage time before processing.
- At  $175^\circ C$  and for a plasma power of 10 W,  $\mu c$ -Si was grown everywhere on the sample, irrespective of the nature of the surface or chamber history.

Relative to the optimized ASD plasma conditions summarized in table 3.2, we found that many parameters could interfere with the selectivity, namely the  $H_2$  concentration in the gas

mixture, plasma power and electrode temperature. We now examine two specific cases where the selectivity is lost.

Fig. 3.12 presents the evolution of the  $\mu\text{c-Si}$  thickness on  $\text{c-Si}$  coated  $\text{AlO}_x$  with time for two non-selective deposition process cases: one with a power of 15 W and electrode temperatures of  $100^\circ\text{C}$ , and the second is with a power of 10 W and electrode temperatures of  $175^\circ\text{C}$ . These data have been obtained using in-situ ellipsometry and the modelling protocol described in the previous chapter.

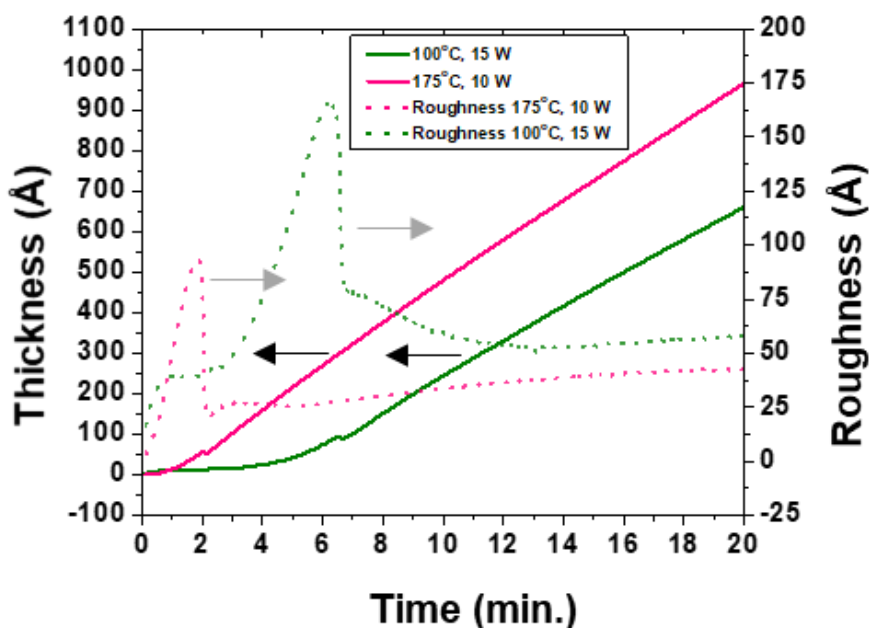


**Figure 3.12** Microcrystalline silicon ( $\mu\text{c-Si:H}$ ) film thickness and roughness evolution with time when depositing on aluminum oxide ( $\text{AlO}_x$ ) using an increased power of 15 W (green) or an increased temperature of electrodes of  $175^\circ\text{C}$  (pink).

It is clear that deposition on the  $\text{AlO}_x$  area displayed in Fig. 3.12 (as modelled by in-situ ellipsometry) evolves very differently from that on  $\text{SiO}_x\text{N}_y$  as was shown in Fig. 3.8; the roughness and thickness display very distinct, abrupt changes and non-monotonicity, respectively. The plot of Si thickness with time has an inflection point at the moment when the roughness drops dramatically. This could represent a real phenomenon, such as a difference in deposition mode, where the layer in the beginning is amorphous and then becomes crystalline with a smaller roughness. Alternatively, if the composition of the layer is a mixture of crystallites and void and does not include an amorphous phase, the abrupt

change could correspond to the direct decrease of void fraction in the phase where the layer become denser after coalescence of large crystallites (as studied by S. Kassout et al. in reference 16). However, this could also represent a modeling artefact.

Summarizing these results, in order to get good selectivity (preventing any deposition on  $\text{AlO}_x$  areas while enabling it on  $\text{SiO}_x\text{N}_y$  areas), it is important to choose RF power and electrode temperature conditions that are in the process window represented by the dark green area (selective area) in Fig. 3.13. In this same figure, the pink area regroups the non-selective cases and in between both, selectivity becomes unpredictable.

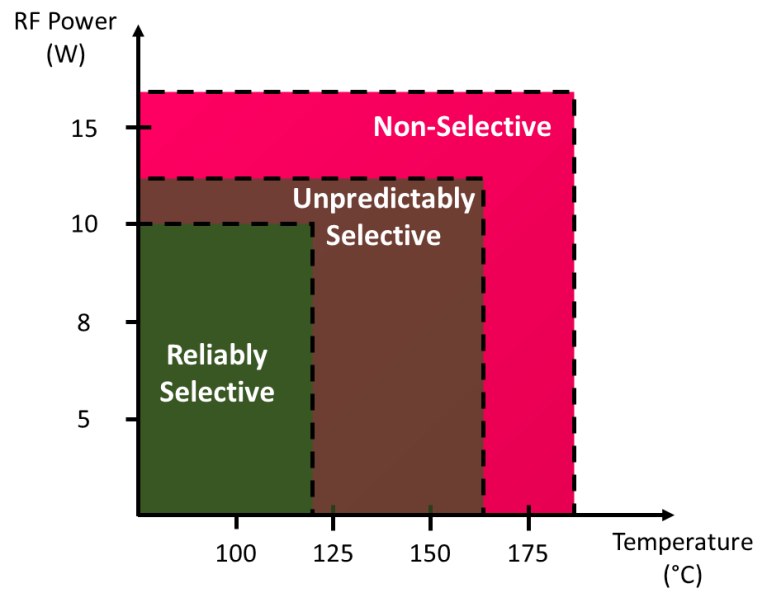


**Figure 3.13** Process window providing selective deposition in terms of radio frequency power and temperature of the electrodes with Ar/SiF<sub>4</sub>/H<sub>2</sub> flow rates equal 200/14/20 sccm respectively and the pressure of 1.7 Torr (for c-Si substrates)

### 3.2.3 Surface contamination

The area selective PECVD parameters summarized in table 3.2 occasionally result in unexpected deposition on  $\text{AlO}_x$  areas, for reasons beyond the effect of the plasma processing parameters. In this section, we document these selectivity-failed examples to allow future work to avoid these problems.



Typically, such kinds of unwanted events occur because of external contamination. This can take place either (i) from a long storage of the sample in the ambient environment, or (ii) after a sudden shut down of the system due to an unscheduled power cuts while samples are inside the plasma chamber. One example of  $\text{AlO}_x$  surface contamination was observed in cross section TEM images in the form of an interlayer between  $\text{AlO}_x$  and  $\mu\text{c-Si}$  (see Fig. 3.14 a). We were not able to determine the reason with certainty. Based on the EDX chemical analysis, traces of oxygen and fluorine were detected in the interlayer (Fig. 3.14b and 3.14c). However, the interlayer was extremely sensitive to the electron beam and was easily removed when moving to the scanning TEM (STEM) mode which uses higher electron energy.

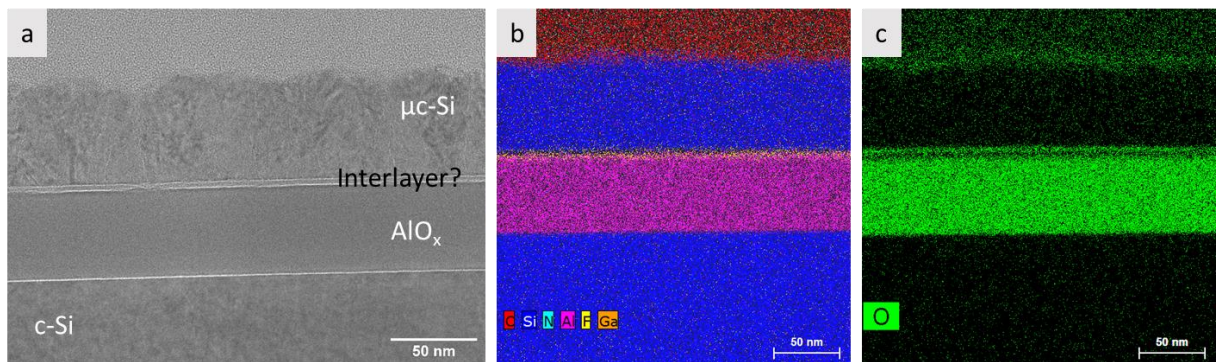


**Figure 3.14** (a) Cross sectional High Resolution TEM (HR-TEM) image of a contaminated  $\text{AlO}_x$  surface (represented by the interlayer) allowing the growth of  $\mu\text{c-Si}$  layer along with its corresponding STEM-EDX chemical mapping (b and c)

For these reasons, the habit was adopted to only use "fresh" substrates, and if ever a sudden power shutdown occurred, to perform multiple "dummy" runs until selectivity was again observed for optimized AS-PECVD conditions. It should also be noted that an unwanted Si layer deposited on an  $\text{AlO}_x$  area (due to surface contamination) adheres very weakly to the surface, and can be peeled off easily by acetone rinsing (in an ultra-sound bath). However, when the deposition of Si on  $\text{AlO}_x$  occurred due to increasing electrode temperature or power or when changing  $\text{H}_2$  gas concentration, the layer was not removed by acetone rinsing.

### 3.3 Selective process for other materials

So far, selective  $\mu\text{-Si}$  deposition on  $\text{SiO}_x\text{N}_y$  versus  $\text{AlO}_x$  in a specific  $\text{Ar/SiF}_4/\text{H}_2$  plasma process (AS-PECVD) has been discussed. To help understand the reason behind this selectivity, the same AS-PECVD base process has been tried on numerous other materials (mostly metals). Nickel (Ni), copper (Cu), chromium (Cr) and aluminum (Al) were deposited using a Boc Edwards A306 thermal evaporator<sup>6</sup>. Silver (Ag) and aluminum<sup>7</sup> were sputtered using Alliance Concept DP650 Magnetron Sputtering System.

The Al, Ni and Cr surfaces were prepared by depositing a 50 nm layer of metal directly on the silicon substrate. Before evaporating Cu, the native oxide on the c-Si substrate was removed by 5 percent HF solution. This cleaning step improves the adhesion of the Cu layer to the substrate and prevents delamination due to the temperature of the electrode in the PECVD system during the selective deposition process<sup>8</sup>.  $\text{SiO}_2$  was deposited in the ECR-PECVD reactor VENUS at 2 mTorr pressure using  $\text{SiH}_4$  and  $\text{O}_2$  gases and microwave power 1 kW.

In-situ ellipsometry was used to check the selectivity on each of metal surfaces. Firstly, the evolution of silicon thickness on top of evaporated Al and Cu surfaces is presented in Fig. 3.15. The model used was built in Complete\_EASE software and metal layers represented by materials data from the library [17]. It was obvious that both metals act differently when exposed to the same plasma process conditions. As occurs with  $\text{AlO}_x$  surfaces,  $\mu\text{-Si}$  does not grow on top of the Al surface, while on Cu, it grows in a way similar to the growth on  $\text{SiO}_x\text{N}_y$  surface. In addition, on the Cu surface, there is a longer nucleation delay compared to  $\text{SiO}_x\text{N}_y$  areas. From the analysis of SE experimental data and modelling, the growth of silicon layer starts after 4 minutes of plasma while on  $\text{SiO}_x\text{N}_y$  area Si starts to

---

<sup>6</sup> For more details about thermal evaporation and sputtering techniques, see appendix

<sup>7</sup> Aluminum was prepared for two different techniques: sputtering and evaporation

**Note:** We tried to deposit Indium (In) film by evaporation but it peeled off after loading the sample into the PECVD system, even after HF cleaning of the c-Si piece. We also tried to evaporate Pt but we couldn't evaporate more than a couple of nm before the crucible cracked. This is due to the fact that liquid Pt reacts with W at the temperature required to evaporate platinum, which is around 2100°C, which is close to maximal for resistive heating in W boats. [21]

grow after 2 minutes of plasma (see Fig. 3.8). Similarly, there was no detected silicon layer on top of Al sputtered surfaces after 20 minutes of AS-PECVD.

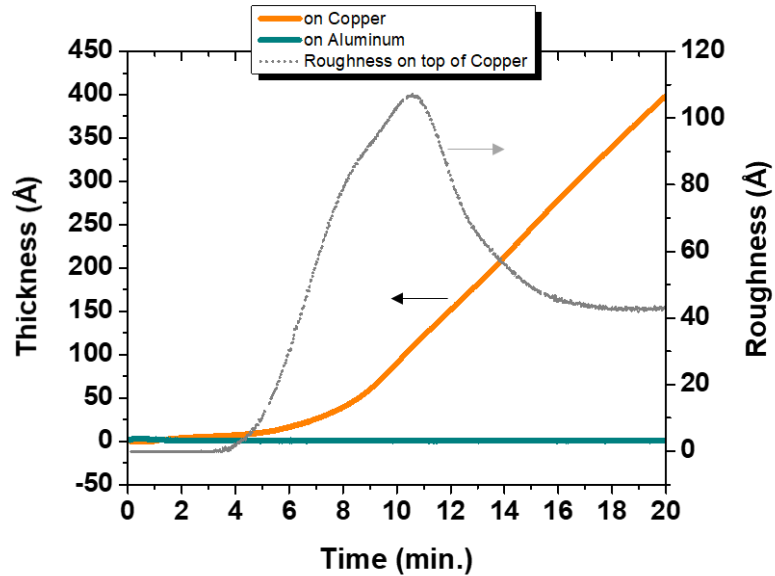


**Figure 3.15** Silicon film thickness evolution (from SE) with time while depositing on aluminum (Al) and copper (Cu) using area selective PECVD conditions described in table 3.3

Secondly, the change in ellipsometric spectra after 20 mins of AS-PECVD process for Cr and Ni surfaces has been explored. As indicated in Fig. 3.16, the comparison of SE before and after deposition shows minor changes after the completion of plasma process. It is hard to confirm whether the changes are due to a very thin layer on top of Cr and Ni surfaces or due to modification in the metal layer caused by ion bombardment produced by the plasma. In order to determine which change is occurring, I tried to add a thin  $\mu\text{-Si}$  layer on top of the metal layer in the ellipsometric model, having the same optical constant as obtained when fitting the thickest silicon layer deposited on top of  $\text{SiO}_x\text{N}_y$  during an ASD process (Fig. 3.7). However, it did not reduce the MSE value, and thus the most likely explanation is that ion bombardment induced a modification in the structure of the metal surface, or alternatively, a reaction has occurred between the metal and silicon, which prevented correct modeling of the deposition. Nevertheless, no  $\mu\text{-Si}$  deposition occurred.

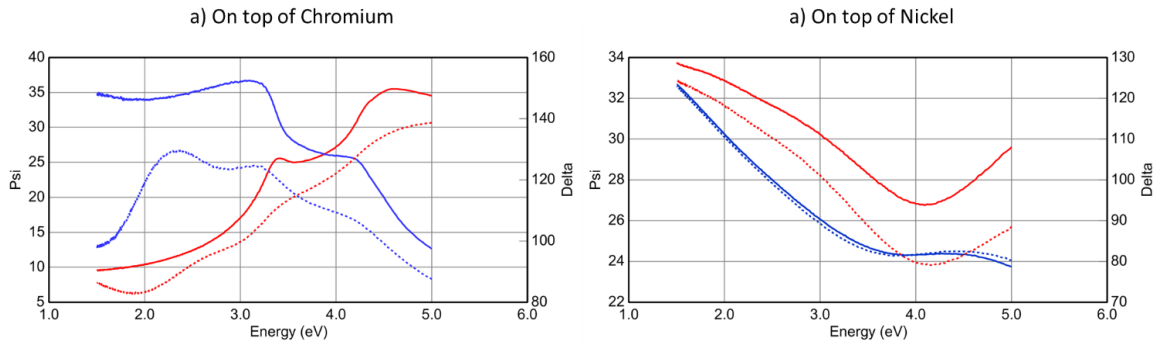


**Figure 3.16** Comparison of ellipsometric spectra for (a) chromium surface and (b) nickel surface before (solid line) and after (dashed line) AS-PECVD process represented by ellipsometric angles  $\Delta$  and  $\Psi$

Subsequently, selectivity was investigated for silver surfaces before and after 20 minutes of Ar/SiF<sub>4</sub>/H<sub>2</sub> AS-PECVD process. The modification in the surface indicates deposition on top of Ag surface (Fig. 3.17). However, as it is an extremely rough layer, the SE data were not exploitable. The “strange” silicon layer on top of Ag can be due to the high reactivity of silver towards halogens, which is a frequent issue in silver mirror applications [18, 19].

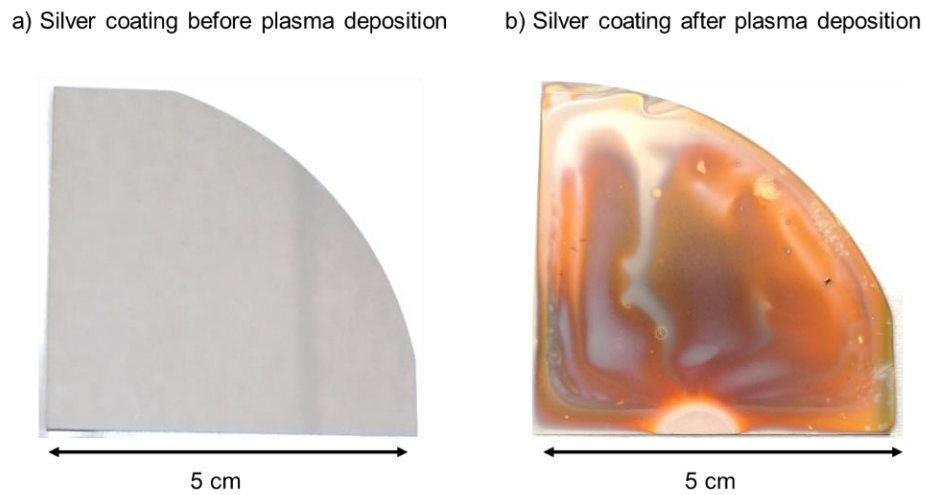


**Figure 3.17** Photos of silver surface (a) before and (b) after AS-PECVD process

Last but not least, SiO<sub>2</sub>/AlO<sub>x</sub> samples were prepared for selective plasma deposition process. The same Configuration 1<sup>9</sup> design for SiO<sub>x</sub>N<sub>y</sub>/AlO<sub>x</sub> was used, but replacing the

<sup>9</sup> See chapter 2 section 2.1

SiO<sub>x</sub>N<sub>y</sub> film by SiO<sub>2</sub>. Fig. 3.18 presents the evolution of the μc-Si layer with time on both SiO<sub>2</sub> and AlO<sub>x</sub> areas. The SiO<sub>2</sub> layer was represented by a classical Lorentz oscillator dispersion function in the SE model. As expected, no growth was observed on AlO<sub>x</sub> during 20 minutes of plasma exposure. In contrast, around 52 nm of microcrystalline silicon layer is deposited on SiO<sub>2</sub>. This means that SiO<sub>2</sub> and SiO<sub>x</sub>N<sub>y</sub> surfaces act similarly towards Ar/SiF<sub>4</sub>/H<sub>2</sub> plasma, and both materials can be considered as “growth areas” for microcrystalline silicon thin film.

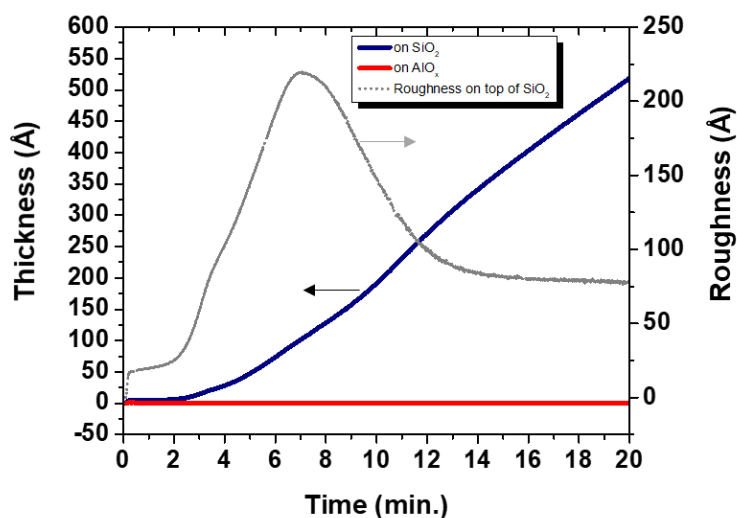


**Figure 3.18** Silicon layer thickness and surface roughness evolution with time measured by in-situ ellipsometry on SiO<sub>2</sub> and AlO<sub>x</sub> surfaces after 20 minutes of AS-PECVD.

The results after 20 minutes of AS-PECVD process for all previously described materials are summarized in table 3.4

Materials	Silicon deposition
Ni	No
Cu	Yes (0.33 Å/s)
Cr	No
Al	No
Ag	Yes (non-uniform layer)
SiO <sub>2</sub>	Yes (0.44 Å/s)

**Table 3.4** Results after AS-PECVD process on different materials

### **3.4 Summary**

In this chapter, we have demonstrated Area Selective PECVD of silicon thin films on  $\text{SiO}_x\text{N}_y$  surfaces, while preventing the deposition on an  $\text{AlO}_x$  area, leaving it pristine. Two radio frequency PECVD reactors (ARCAM and ATOS) were used to perform the depositions from  $\text{Ar/SiF}_4/\text{H}_2$  gas mixture. For both reactors, the selective deposition conditions were found in the transition phase between depositing amorphous silicon and microcrystalline silicon. The selectively deposited layer on top of  $\text{SiO}_x\text{N}_y$  is of microcrystalline nature.

Varying plasma process conditions around these selective parameters allowed us to determine a process window (Fig. 3.13) that delineates selectivity breakdown, manifesting as silicon growth on an  $\text{AlO}_x$  surface. Specifically, deposition occurs on an  $\text{AlO}_x$  surface when increasing the RF power (from 10 to 15 W) or the temperature of the electrodes (from 100 to 175 °C). Notably, the AS-PECVD process is quite sensitive to surface contamination as well as to the plasma chamber wall condition. It is important to have a-Si coated walls for ARCAM reactor (hot walls), and to have no traces of  $\text{SiH}_4$  in the ATOS chamber (cold walls) prior to AS-PECVD process. This means that even 1 sccm of  $\text{SiH}_4$  in the gas mixture or any prior deposition using this same gas will result in the deposition of  $\mu\text{c-Si}$  on  $\text{AlO}_x$  area, so a loss of selectivity.

Along with  $\text{SiO}_x\text{N}_y$  and  $\text{AlO}_x$  surfaces, our AS PECVD process also shows selectivity for other materials. Indeed, microcrystalline silicon thin films can be grown on copper and silicon oxide surfaces under AS-PECVD conditions, allowing them to be considered as a “growth area”. Conversely, aluminum, nickel and chromium can be considered as “non-growth area” as their surfaces prevent the growth of silicon.

The remaining question is as follows: what is occurring on only the  $\text{AlO}_x$  surface that is preventing Si growth, despite the fact that the plasma deposition technique is well known for its non-selectivity due to the nature of species fluxes generated by the plasma (ions, electrons, radicals...). Two possibilities exist for a selectivity between the two surfaces:

(1) the plasma, very locally (in the immediate vicinity), is different due to some influence from the surface, such as different secondary electron emission properties or molecular recombination rates on that particular surface. If this were the case, however, one would expect a more gradual transition in nucleation rate at the boundary between the two surfaces, which is not our case [20].

(2) The precursors involved in the process (either  $\text{SiF}_x$ , F or H) react with the two surface areas in different ways. On  $\text{AlO}_x$  area, it is either Al atoms or O atoms that react with Ar/SiF<sub>4</sub>/H<sub>2</sub> plasma differently than the N, and Si atoms in  $\text{SiO}_x\text{N}_y$  towards that particular plasma chemistry. Furthermore, as we obtained deposition on  $\text{SiO}_2$  surface without deposition on Al, one could eliminate the possibility of O reacting with the plasma precursors. It is this question that we aim to answer in the next chapter.

## References

- [1] G. Akiki, D. Suchet, D. Daineka, S. Filonovich, P. Bulkin and E. V. Johnson, “Area selective deposition of silicon by plasma enhanced chemical vapor deposition using a fluorinated precursor”. *Applied Surface Science* 531 (2020) 147305.
- [2] G.E. Jellison, F.A. Modine, Parameterization of the optical functions of amorphous materials in the interband region, *Appl. Phys. Lett.* 69 (1996) 371–373.
- [3] G.E. Jellison Jr., V.I. Merkulov, A.A. Puretzky, D.B. Geohegan, G. Eresa, D.H. Lowndes, J.B. Caughman, Characterization of thin-film amorphous semiconductors using spectroscopic ellipsometry, *Thin Solid Films* 377–378 (2000) 68.
- [4] C. M. Herzinger, B. Johs, W. A. McGahan, J. A. Woollam, and W. Paulson, Ellipsometric determination of optical constants for silicon and thermally grown silicon dioxide via a multi-sample, multiwavelength, multi-angle investigation, *Journal of Applied Physics* 83, 3323 (1998);
- [5] F. K. Urban III, P. Ruzakowski Athey and Md. S. Islam, Modelling of surface roughness in variable-angle spectroscopic ellipsometry, using numerical processing of atomic force microscopy images, *Thin Solid Films* 315, 186 (1994).
- [6] P. Ruzakowski Athey, F. K. Urban III, and P. H. Holloway, Use of multiple analytical techniques to confirm improved optical modeling of SnO<sub>2</sub>:F films by atomic force microscopy and spectroscopic ellipsometry, *Journal of Vacuum Science & Technology B* 14, 3436 (1996); doi: 10.1116/1.588776
- [7] R. Vallat, R. Gassilloud, B. Eychenne, and C. Vallée, “Selective deposition of Ta<sub>2</sub>O<sub>5</sub> by adding plasma etching super-cycles in plasma enhanced atomic layer deposition steps”. *J. Vac. Sci. Technol. A Vacuum, Surfaces, Film.* 35, 01B104 (2017).
- [8] Jellison, Jr, G E, Chisholm, M F, and Gorbatkin, S M. Optical functions of chemical vapor deposited thin-film silicon determined by spectroscopic ellipsometry. *Applied Physics Letters* 62, 3348 (1993); doi: 10.1063/1.109067
- [9] H. Fujiwara, M. Kondo, and A. Matsuda, “Real-time spectroscopic ellipsometry studies of the nucleation and grain growth processes in microcrystalline silicon thin films Hiroyuki”. *Phys. Rev. B* 63, 115306 (2001).



- [10] H. Fujiwara, M. Kondo, and A. Matsuda, “Interface-layer formation in microcrystalline Si:H growth on ZnO substrates studied by real-time spectroscopic ellipsometry and infrared spectroscopy”. *J. Appl. Phys.* 93, 2400 (2003).
- [11] Q. Liu, J.F. Wall, E.A. Irene, Si/SiO<sub>2</sub> interface studies by spectroscopic immersion ellipsometry and atomic force microscopy, *J. Vac. Sci. Technol. A* 12 (1994) 2625.
- [12] CompleteEASE software manual, chapter 3, J.A. Woollam Co. 2004-2014.
- [13] P. Petrik, L.P. Biro, M. Fried, T. Lohner, R. Berger, C. Schneider, J. Gyulai, H. Ryssel, Comparative study of surface roughness measured on polysilicon using spectroscopic ellipsometry and atomic force microscopy, *Thin Solid Films* 315, 1998. 186–191
- [14] Yanhui Li, Li Wang, Shaowu Yin, Fuming Yang, Crystallization behavior of amorphous silicon nitride added with silicon powder, *Materials Chemistry and Physics* 141 (2013) 874e881
- [15] P. Reinig, B. Selle, F. Fenske, W. Fuhs, V. Alex, and M. Birkholz, “Highly <100> oriented growth of polycrystalline silicon films on glass by pulsed magnetron sputtering”, *J. Vac. Sci. Technol. A Vacuum, Surfaces, Film.* 20, 2004 (2002).
- [16] S. Kasouit, S. Kumar, R. Vanderhaghen, P. Roca i Cabarrocas, and I. French, “Fluorine and hydrogen effects on the growth and transport properties of microcrystalline silicon from SiF<sub>4</sub> precursor”, *J. Non. Cryst. Solids* 299–302, 113 (2002).
- [17] E.D. Palik. “Handbook of optical constants of solids”. Volume 1, Pages 284-285, (1998).
- [18] Bulkin, P.; Gaiaschi, S.; Chapon, P.; Daineka, D.; Kundikova, N. Protective coatings for front surface silver mirrors by atomic layer deposition. *Opt. Exp.* 2020, 28, 15753,
- [19] P. Bulkin, P. Chapon, D. Daineka, G. Zhao, and N. Kundikova, PECVD SiN<sub>x</sub> Thin Films for Protecting Highly Reflective Silver Mirrors: Are They Better Than ALD AlO<sub>x</sub> Films, *Coatings*, 2021, 11, 771.
- [20] A. J. Dekker, Secondary Electron Emission. *Solid State Physics*, (1958). 251–311.
- [21] Deposition materials, Evaporation materials, Platinum (Pt) Pellets Evaporation Materials, Thermal evaporation, <https://www.lesker.com>

# Chapter 4

## Origins of Area selective PECVD process

4.1	Chemical characterization of substrate surfaces .....	94
4.1.1	Energy dispersive X-ray (EDX) chemical analysis on $\text{SiO}_x\text{N}_y$ and $\text{AlO}_x$ areas after plasma deposition process .....	94
4.1.2	X-ray photoelectron spectroscopy (XPS) chemical analysis for $\text{SiO}_x\text{N}_y$ and $\text{AlO}_x$ areas .....	97
4.1.3	Surface-wetting characterization of $\text{AlO}_x$ and $\text{SiO}_x\text{N}_y$ areas .....	101
4.2	Plasma characteristic .....	104
4.2.1	Plasma optical emission spectra .....	104
4.2.2	Peak to peak and $V_{\text{DC}}$ measurements for different plasma conditions .....	107
4.3	Summary .....	111
	References .....	113

## **4 Origins of Area Selective PECVD process**

In the previous chapter, area selective plasma deposition has been achieved for very specific experimental conditions. It has been shown that some materials promote the deposition of microcrystalline silicon thin film (such as silicon oxynitride, copper and silicon oxide) while others inhibit it (namely aluminum oxide, aluminum, nickel and chromium). We have yet to determine whether this ASD effect may be due to local differences in the plasma chemistry or in the surface chemistry.

The present chapter is devoted to the attempt to identify the reason behind our area selective PECVD process of microcrystalline silicon. For this, Ar/SiF<sub>4</sub>/H<sub>2</sub> plasma characterization and surface chemical analyses were done. A part of this work was published in a peer-reviewed journal (see reference [1])

We will focus on AlO<sub>x</sub> and SiO<sub>x</sub>N<sub>y</sub> areas present next to each other on the same c-Si substrate. Based on the results obtained, the mechanism or the model for our selective process will be suggested.

### **4.1 Chemical characterization of substrate surfaces**

#### **4.1.1 Energy dispersive X-ray (EDX) chemical analysis on SiO<sub>x</sub>N<sub>y</sub> and AlO<sub>x</sub> areas after plasma deposition process.**

Structural and chemical characterizations at high resolution were performed using the TEM and Scanning TEM High-Angle Annular Dark Field (STEM-HAADF) imaging modes of two representative samples containing SiO<sub>x</sub>N<sub>y</sub> and AlO<sub>x</sub> layers after an AS-PECVD process.

A STEM-HAADF image of the cross sectional lamella containing first only the AlO<sub>x</sub> area is presented in Fig. 4.1. As it can be observed, even though the sample was exposed to the PECVD process using the SiF<sub>4</sub> precursor, no trace of any Si layer is observed near the surface (there is only the protective layer, which is a carbon layer deposited prior to the FIB

fabrication of the lamella). Another typical finding that can be observed from the STEM-HAADF EDX mapping involves the presence of fluorine, in very small amount, detected primarily on the surface of the  $\text{AlO}_x$  layer. It is likely that those F atoms are bonded to Al atoms because otherwise fluorine is expected to be difficult to detect once the surface is exposed to the atmosphere for any length of time. However, the bonding configuration of F can't be determined using EDX.

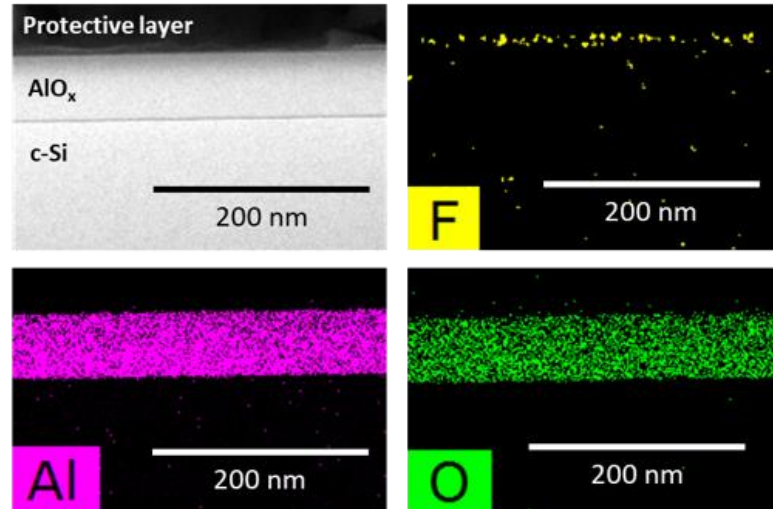


**Figure 4.1** HAADF image of  $\text{AlO}_x$  area with corresponding STEM-EDX chemical mapping for three elements of interest F (yellow), Al (pink), and O (green)

For the  $\text{SiO}_x\text{N}_y$  area, a TEM image of its corresponding cross-sectional lamella clearly shows the multi-layered stack (Fig. 4.2a). A closer analysis by Fast Fourier Transform (FFT) of the silicon layer deposited on top of  $\text{SiO}_x\text{N}_y$  brings into evidence it's microcrystalline structure (as was expected from SE and GIXRD analysis) with crystallite dimensions of few nanometers. Moreover, the  $\text{SiO}_x\text{N}_y$  layer was found to be very sensitive to the electron beam exposure, especially when working with scanning TEM mode as it is seen by the “black spots” in Fig. 4.2b.

From the STEM-HAADF EDX chemical analysis in Fig. 4.3, one can notice that fluorine is present mostly inside the  $\text{SiO}_x\text{N}_y$  layer (unlike the  $\text{AlO}_x$  layer, where F was only present at the surface). This must be the result of the diffusion of F atoms into  $\text{SiO}_x\text{N}_y$  layer during the deposition of  $\mu\text{c-Si:H}$  (using an  $\text{SiF}_4$  plasma precursor), as no F is present in the precursors for  $\text{SiO}_x\text{N}_y$  growth. In addition, the quantity of F is very low in the  $\mu\text{c-Si:H}$ , which

is normal when using Ar/SiF<sub>4</sub>/H<sub>2</sub> precursor, as it is effectively scavenged by H. One can also note the absence of F in the silicon substrate in both cases.

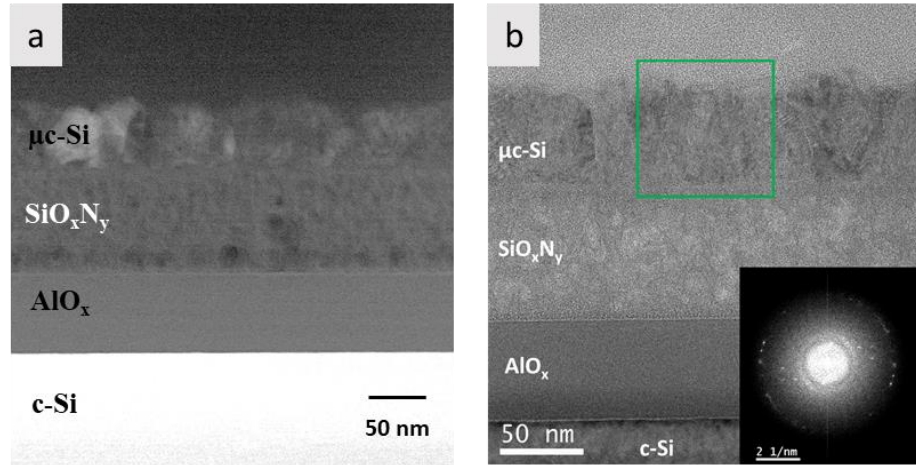


**Figure 4.2** (a) Dark Field scanning and (b) Bright Field TEM images of the SiO<sub>x</sub>N<sub>y</sub> area. The inset on the right edge of the TEM image shows the FFT profile corresponding to the green area confirming the microcrystalline structure of the top layer

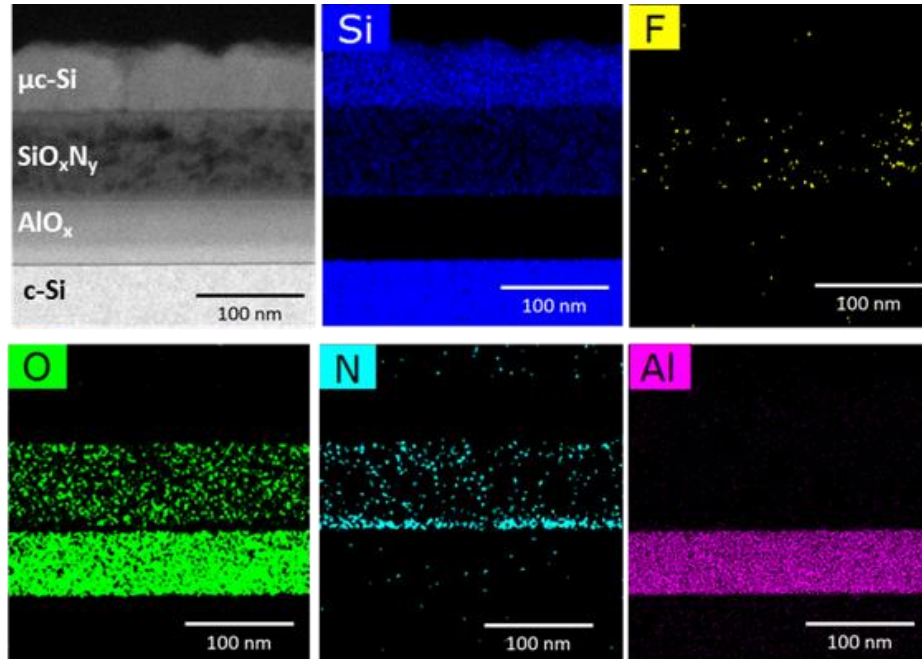


**Figure 4.3** HAADF image with its corresponding STEM-EDX chemical mapping of SiO<sub>x</sub>N<sub>y</sub> area with the chosen element of interest Si (dark blue), F (yellow), O (green), N (blue), Al (pink)

The diffusion of F into  $\text{SiO}_x\text{N}_y$  indicates that this layer could have a columnar structure. To verify this hypothesis, we deposited an  $\text{AlO}_x$  layer on top of the  $\text{SiO}_x\text{N}_y/\text{AlO}_x$  stack and the HR-TEM image in Fig. 4.4 shows the resulting  $\text{AlO}_x/\text{SiO}_x\text{N}_y/\text{AlO}_x$  stack. This image confirms the columnar structure of  $\text{SiO}_x\text{N}_y$  layer as the  $\text{AlO}_x$  material could penetrate inside the layer (red arrows).

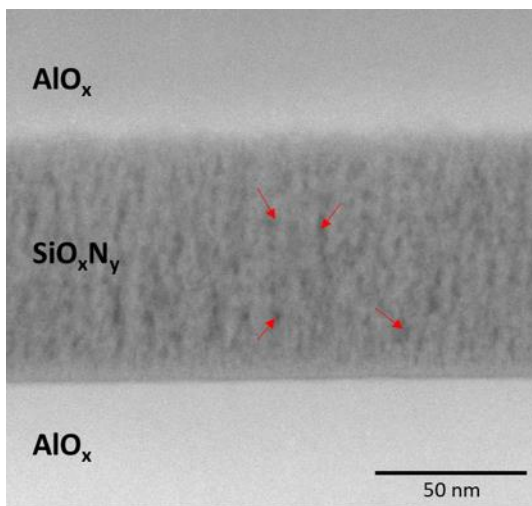


**Figure 4.4** STEM-HAADF image of  $\text{AlO}_x/\text{SiO}_x\text{N}_y/\text{AlO}_x$  showing the columnar structure of  $\text{SiO}_x\text{N}_y$  layer. The red arrows show the  $\text{AlO}_x$  material (white) penetrating into  $\text{SiO}_x\text{N}_y$  (black)

The TEM images allow one to verify the microcrystalline silicon nature of the Si deposited on top of  $\text{SiO}_x\text{N}_y$  and to show the columnar structure of this final layer. EDX shows the presence of fluorine on top of the  $\text{AlO}_x$  layer. However, to understand the reason behind selectivity, some necessary information about surface chemistry is still missing. Therefore, XPS chemical analyses were carried out for the same substrate and will be shown in the next chapter.

#### **4.1.2 X-ray photoelectron spectroscopy (XPS) chemical analysis for $\text{SiO}_x\text{N}_y$ and $\text{AlO}_x$ areas**

The  $\text{SiO}_x\text{N}_y$  and  $\text{AlO}_x$  surface chemistries resulting from the selective deposition process with  $\text{Ar}/\text{SiF}_4/\text{H}_2$  plasma (described in chapter 3) have been also investigated using X-ray Photoelectron Spectroscopy (XPS). In order to preserve the integrity of the chemical

information and minimize surface contamination, an encapsulation layer consisting of 10 nm of amorphous silicon layer was deposited on top, using a  $\text{SiH}_4/\text{H}_2$  plasma, immediately after the AS-PECVD process and in the same plasma reactor (ATOS) (Fig. 4.5).

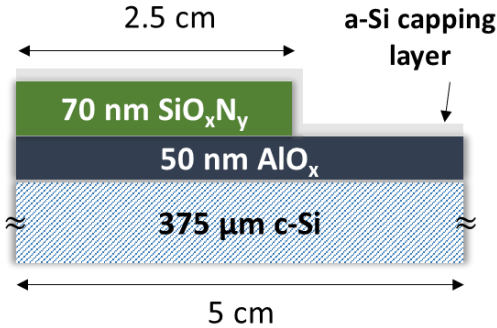
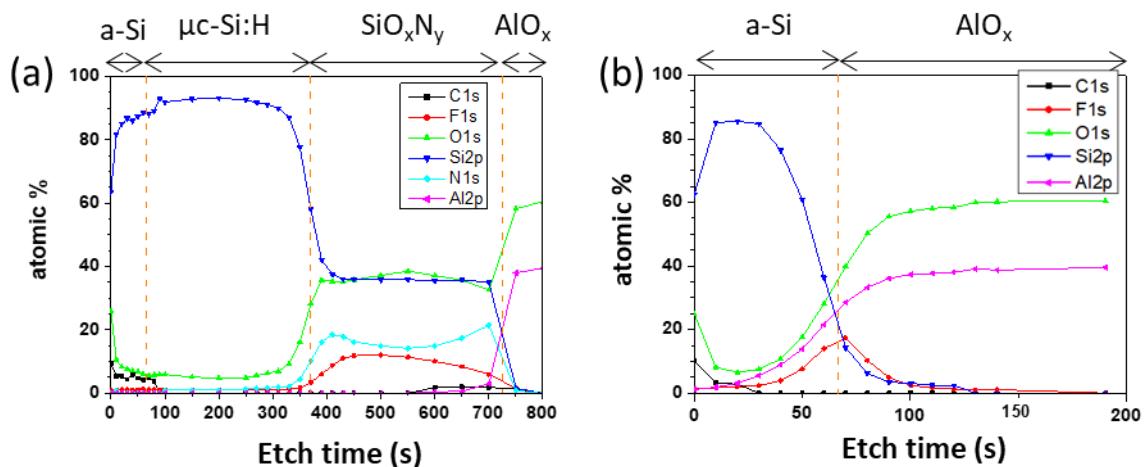


**Figure 4.5** Schema of the substrate used for XPS chemical analyses

The chemical composition at the buried interfaces was determined by sequential depth profiling of each stack, and the corresponding in-depth overall atomic percentage profiles are presented in Fig. 4.6. For both  $\text{SiO}_x\text{N}_y$  and  $\text{AlO}_x$  areas, C and O are present at the initial, top surface and correspond to the adventitious carbon layer inherent to ambient air exposure. The XPS shows that no trace of fluorine is observed within the  $\mu\text{c-Si:H}$  layer (similar to EDX). This means that the F from the  $\text{SiF}_4$  precursor is fully scavenged by H during the growth process, at least to a level below the XPS detection threshold. This result is consistent with the model of  $\text{Ar/SiF}_4/\text{H}_2$  plasma chemistry described in the introduction and observed in previous section. All the different interfaces are sharp and clearly identified.

Concerning the  $\text{SiO}_x\text{N}_y$  area, the  $\mu\text{c-Si:H} / \text{SiO}_x\text{N}_y$  interface is reached after 370 s of sputtering. During the profiling of this  $\text{SiO}_x\text{N}_y$  layer, the O and Si contents are roughly constant although the F profile demonstrates a gradient (12 atomic percent at maximum value), negatively correlated with the N distribution. This confirms the trend evidenced by the STEM-EDX analysis, also showing F incorporation.

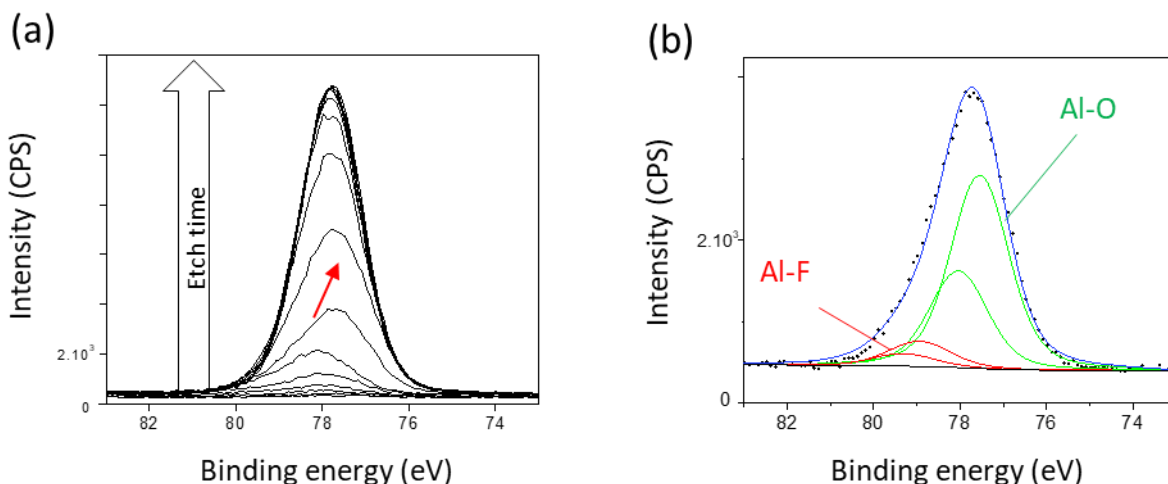
For the  $\text{AlO}_x$  area, F is only present at the a-Si/ $\text{AlO}_x$  interface, and reaches a content of 18 at%. The  $\text{AlO}_x$  layer is composed of 60% of O and 40% of Al, and the F does not diffuse into this layer (as it does into the  $\text{SiO}_x\text{N}_y$  one).



**Figure 4.6** XPS depth profiles of (a) SiO<sub>x</sub>N<sub>y</sub> and (b) AlO<sub>x</sub> areas on c-Si substrate. (Note: x axis scales are not the same for both graphs).

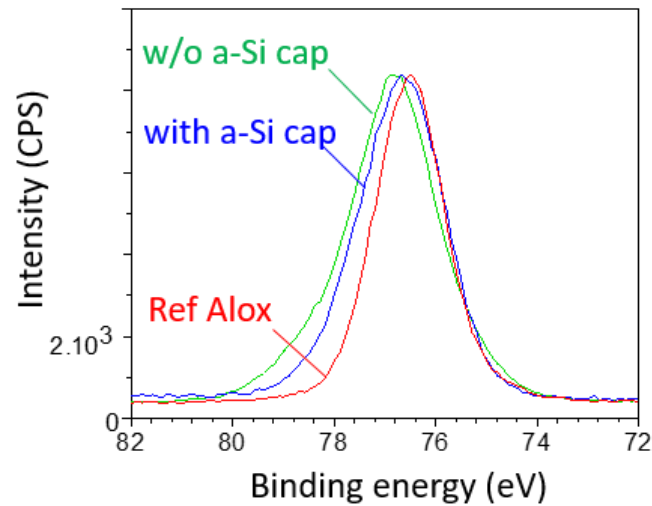
In addition to these elemental chemical composition profiles, a more precise XPS analysis was conducted using high-energy-resolution spectral windows in order to access information on the chemical environments of each element. We will focus on the AlO<sub>x</sub> area where no deposition occurred. The evolution of the Al2p peak during profiling is shown in Fig. 4.7 (a). Note that the capping a-Si layer is very thin (less than the escape depth of Al2p photoelectrons), so the Al is detected even before sputtering. The Al2p peak position is progressively shifted toward lower binding energies with increased sputtering time, i.e. when probing the bulk AlO<sub>x</sub> layer. This behavior is consistent with the presence of a more electronegative element at the surface compared to the bulk, and clearly suggests the formation of Al-F bonds at the surface of the AlO<sub>x</sub> layer. Indeed, a fit of the Al2p photopeak representative of the AlO<sub>x</sub> surface (70 s etching time on the profile of Fig. 4.7 (a)) is presented in Fig. 4.7 (b). The Al2p spectra are reconstructed using a Gaussian–Lorentzian convolved function with L/G = 30%. The spin–orbit coupling Al2p<sub>1/2</sub>–Al2p<sub>3/2</sub> was set to 0.44 eV. For Al2p, there are two possible states having two different binding energies. Consequently, the fitting requires two doublets, attributed to Al–O and Al–F bonds, whose energy positions are shifted by 1.5 eV. The expected energy difference is around 2.0 eV for pure Al<sub>2</sub>O<sub>3</sub> and AlF<sub>3</sub> compounds [2] suggesting a rather mixed Al–O–F environment at the surface of the AlO<sub>x</sub> layer. An Al–O/Al–F ratio of 2.66 is estimated, leading to a ratio of F/Al=2.9. This indicates that the amount of F in fact exceeds the number of Al sites available, so in fact only a part of the F is really bonded, and the rest is likely adsorbed on top.





**Figure 4.7** (a) Al<sub>2</sub>p photopeak evolution with etching time for a-Si/AlO<sub>x</sub>/c-Si sample and (b) typical Al<sub>2</sub>p fit at the AlO<sub>x</sub> surface, *i.e.* 70 s etching time.

The same analyses have been carried out on two other samples: one before any plasma process (as a reference, labelled “Ref AlO<sub>x</sub>”) and another with a selective deposition process but without any capping layer (labelled “w/o a-Si cap”). Fig. 4.8 shows the Al<sub>2</sub>p photopeaks for those three samples. It is clear that after exposure to the Ar/SiF<sub>4</sub>/H<sub>2</sub> plasma, a new contribution at high binding energy, attributed to Al-F bonds, is detected. It is also interesting to note that according to Al-O/Al-F atomic percentage ratio, the amount of Al-F bonds is higher on the sample without the a-Si capping (Al-O/Al-F=3.21) compared to the one with (Al-O/Al-F=5.44). This indicates that some of the Al-F bonds created during the selective deposition process are removed from the AlO<sub>x</sub> surface to allow the deposition of the a-Si:H film. It can be concluded that the more Al-F bonds and absorbed F that are present, the better selectivity is obtained, which is consistent with the lack of deposition on AlO<sub>x</sub> and metallic Al as was observed in section 3.4.

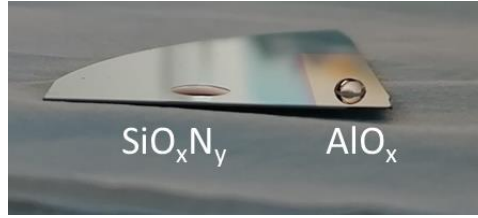


**Figure 4.8** Comparison of Al<sub>2</sub>p photopeaks of AlO<sub>x</sub> area before plasma process (red) and after (green without a-Si capping layer, and blue with).

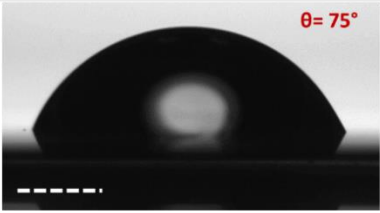



### 4.1.3 Surface-wetting characterization of AlO<sub>x</sub> and SiO<sub>x</sub>N<sub>y</sub> areas

Aluminum oxide and silicon nitride (or oxynitride) have numerous common properties. Both are highly transparent dielectrics, electrical insulators and are used as silicon passivation layer for solar cells applications [3-8]. However, they act very differently towards Ar/SiF<sub>4</sub>/H<sub>2</sub> plasma under AS-PECVD conditions. Looking for further explanations of this phenomenon, we performed water contact angle measurements on our samples.

By doing measurements on both AlO<sub>x</sub> and SiO<sub>x</sub>N<sub>y</sub> before any plasma exposure, we found that those two materials have distinct wetting characteristics, indicated by the difference in the water contact angle (WCA). This is immediately evident even from visual observation (Fig. 4.9).



**Figure 4.9** Photo of the  $\text{AlO}_x/\text{SiO}_x\text{N}_y$  substrate during contact angle measurement using de-ionized water before plasma deposition

	Before area-selective plasma deposition process	After area-selective plasma deposition process
Non-growth area ( $\text{AlO}_x$ )	 $\theta = 75^\circ$	 $\theta = 45^\circ$
Growth area ( $\text{SiO}_x\text{N}_y$ or $\mu\text{c-Si}$ )	 $\text{SiO}_x\text{N}_y$ surface $\theta = 38^\circ$	 $\mu\text{c-Si}$ surface $\theta = 34^\circ$

**Figure 4.10** Water contact angle of  $\text{AlO}_x$  and  $\text{SiO}_x\text{N}_y$  areas before and after AS-PECVD.  $\text{SiO}_x\text{N}_y$  area becomes covered with  $\mu\text{c-Si}$  after AS-PECVD (scale bar: 200  $\mu\text{m}$ ).

More precise contact angle measurements were done on an Attension® Theta Optical tensiometer. The volume of the water droplet used in this study is approximately 4  $\mu\text{L}$ . Fig. 4.10 shows the microscope images as well as WCA on  $\text{SiO}_x\text{N}_y$  and  $\text{AlO}_x$  areas before and after AS-PECVD.

- Before AS-PECVD process, the WCA of the as-deposited  $\text{SiO}_x\text{N}_y$  is  $38^\circ$  and that of as-deposited  $\text{AlO}_x$  (after ALD) is  $75^\circ$ , meaning that  $\text{SiO}_x\text{N}_y$  is more hydrophilic than  $\text{AlO}_x$ . From those WCA values we were able to calculate the surface free energies (SFE)<sup>1</sup> and found, as we expected, that  $\text{SiO}_x\text{N}_y$  has a greater SFE ( $55.5 \text{ mJ/m}^2$ ) compared to that of  $\text{AlO}_x$  ( $31.6 \text{ mJ/m}^2$ ).

<sup>1</sup> The method for SFE calculation is detailed in chapter 2 section 2.3.5

- After the AS-PECVD process, if we compare the  $\text{AlO}_x$  area before and after AS-PECVD, we can notice that the Ar/SiF<sub>4</sub>/H<sub>2</sub> plasma led to some modification to the surface as the WCA is reduced from 75° (before plasma) to 45° (after plasma). This means that the surface free energy was enhanced. Based on XPS and EDX previous analyses, this modification is attributed to the excess of F on  $\text{AlO}_x$  surface and the presence of Al-F bonds. Therefore, in our case, fluorination makes the surface more hydrophilic by reducing its water contact angle. A similar effect has been seen by K. Roodenko et al. as they showed that XeF<sub>2</sub> plasma (used to etch silicon) produces a hydrophilic Al surface due to its saturation with Al-F bonds [9]. Although, this is not true for all fluorine terminated surfaces, as in some cases, a decrease of fluorine content leads to a wettability transition from superhydrophobicity to superhydrophilicity [10, 11].

The correlation between surface-wettability and selective deposition has been investigated in previous studies. Awaya et al. showed that silicon oxide could be selectively deposited on the Si, SiO<sub>2</sub> and OFPR resist surfaces by the hydrolysis reaction of SiCl<sub>4</sub>. Under the same conditions, there is no growth of silicon oxide on Poly-perfluoro-alkyl acrylate (PPFAA) or conventional resist treated with NF<sub>3</sub> plasma, as such surfaces have lower surface energies [12, 13]. Another example is the selective deposition of poly(acrylates) on a SiO<sub>2</sub>/Cu line space patterns using spin coating. In fact, poly(acrylates), containing semifluorinated groups, selectively deposit on Cu without any chemical modification of the underlying substrate. The authors suggest that fluorinated polymers are repelled from the most hydrophilic surface (which is SiO<sub>2</sub> in their case) [14].

Surface wettability is usually useful for liquid-surface interaction, as the greater the surface energy the better the liquid adhesion to the surface. Only a few groups have investigated the relationship between surface energy and thin film growth by PECVD [15, 16]. At this point, the dependence on surface wettability of our AS-PECVD is not clear and remains a topic for further study.

## **4.2 Plasma characteristics**

### **4.2.1 Plasma optical emission spectra**

In order to determine the composition of Ar/SiF<sub>4</sub>/H<sub>2</sub> plasma and to see if this could be a good predictor of AS-PECVD conditions, optical emission spectroscopy measurements were performed through a sapphire viewport in the ATOS reactor using an Ocean Optics Maya 2000 Pro fiber optic spectrometer. The fiber optic collection system position allows one to detect the emission from the plasma bulk rather than from the sheath<sup>2</sup> and integrates an optical signal over large volume of the plasma. OES spectra were registered in the spectral range 200 nm-1000 nm after plasma ignition under the following ASD conditions: 200/14/20 sccm for Ar/SiF<sub>4</sub>/H<sub>2</sub> gas flow rates respectively, a pressure of 1.7 Torr, electrode temperature of 100 °C and a power of 10 W. For the sake of clarity, we choose to show OES spectrum in the spectral range 200 nm-730 nm (Fig. 4.11). The most intense detected emission lines with their correspondent plasma species are listed in table 4.1. The obtained OES spectrum is coherent with the OES analyses of Ar-SiF<sub>4</sub>-H<sub>2</sub> plasmas from previous studies [17-19] with a small difference in terms of the intensity doublets at 415 nm and 420 nm as are relatively intense in our case.

Qualitatively, SiF<sub>3</sub> are the most abundant species among SiF<sub>x</sub>, resulting from the dissociation of SiF<sub>4</sub> in the plasma (considering that the intensity of the optical emission lines is directly linked to the density of the plasma species and the electron energy distribution function [20]). Therefore, SiF<sub>3</sub> is the most likely growth precursor under ASD conditions, confirming the statement mentioned in the introduction about the growth mechanism from Ar/SiF<sub>4</sub>/H<sub>2</sub> plasma chemistry.

---

<sup>2</sup> The fiber optic collects the light from the volume that is relatively far from the substrate electrode as seen in figure 2.11 in chapter 2

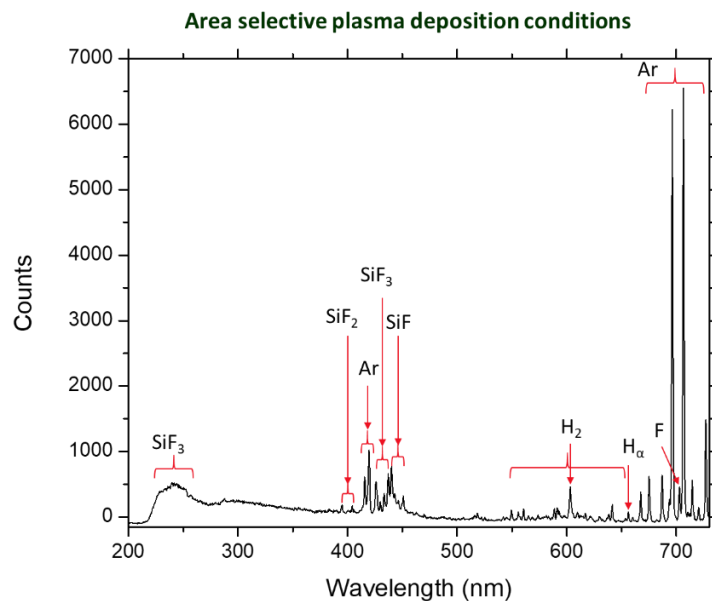


**Figure 4.11** Typical optical emission spectrum observed for an Ar/SiF<sub>4</sub>/H<sub>2</sub> under area selective deposition conditions

Species	Wavelength
SiF <sub>3</sub>	240 nm
	427 nm
SiF <sub>2</sub>	395 nm
SiF	449 nm
H <sub>2</sub>	602 nm
H $\alpha$	656 nm
F	703 nm
Ar	415.8 nm
	419.5 nm
	696 nm
	706.51 nm

**Table 4.1** Plasma species detected from OES with their corresponding emission wavelength. [21-

24]

Intensities of the emission lines for SiF<sub>3</sub> (240.2 nm), F (703 nm) and Ar (706.51 nm) were tracked during the AS-PECVD process. As shown in Fig. 4.12 the intensities of the chosen species remain constant for the whole ASD process. This means that no additional species are detected after plasma-surface interaction, or at least not in the detection region where the signals are collected by the OES fiber optic. Moreover, no change in signals occurs when the nucleation delay ends (i.e. after 2 minutes of AS-PECVD process).

In addition, we have tried to register OES emission lines for a non-selective PECVD process - that is to say, by setting the same AS-PECVD conditions except for the plasma power which was changed to 15 W. By comparing the OES spectra corresponding to the selective and non-selective plasma process (Fig. 4.13), we found that no new emission line appears and it is just a minor change in the light intensity of the all emission lines given in table 4.1. The role of RF power on plasma deposition using SiF<sub>4</sub>/H<sub>2</sub> plasma has been previously interpreted using OES. It was shown that an increase in RF power leads to a rise in the total electron density and deposition rate. However, in that study, the Ar concentration in the plasma was low which is the reverse of our plasma conditions [21].

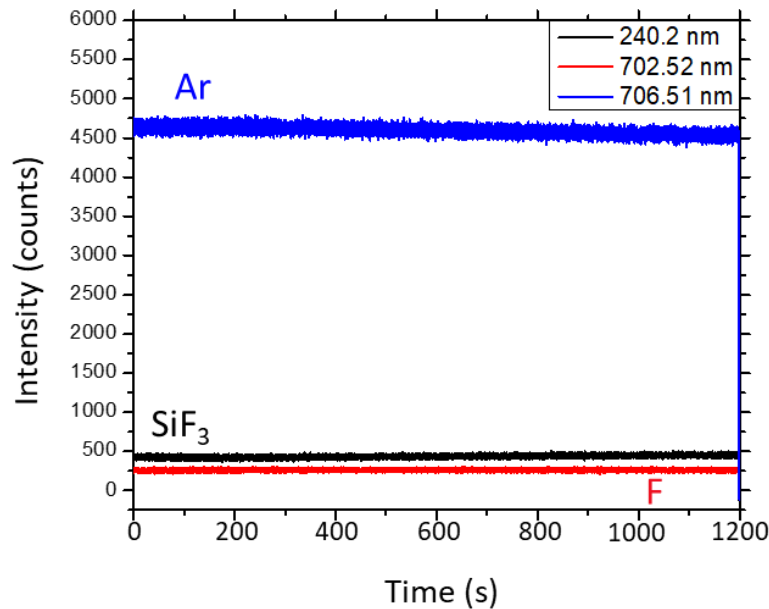


**Figure 4.12** Time resolved OES emission lines at 240.2 nm (SiF<sub>3</sub>), 703 nm (F) and 706.51 nm (Ar) wavelengths during an area selective PECVD process

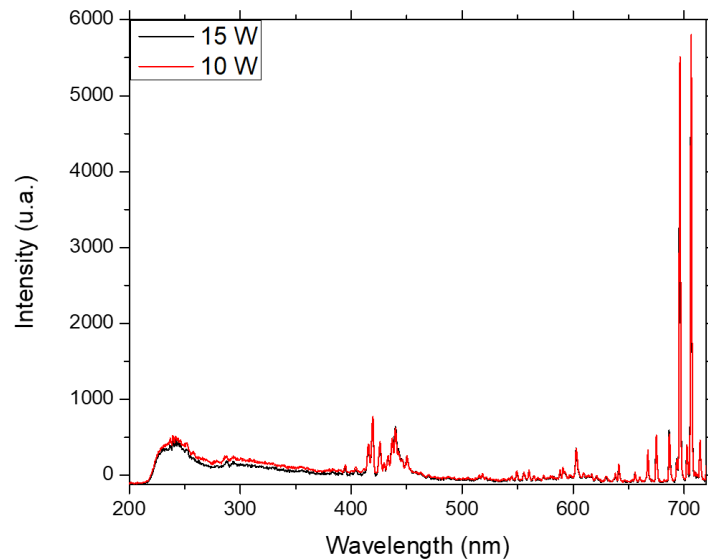


**Figure 4.13** Optical emission spectra for 10 W and 15 W plasma power

This OES study shows no change in the emission lines during the whole AS-PECVD process. Also, OES spectra for AS-PECVD process is similar to that for non-selective process conditions. Therefore, it is not the plasma composition that is the important factor changing with time or with plasma power, but rather something else. In the next section, we look at another potential cause: the ion energy or flux.

#### **4.2.2 Peak to peak and $V_{DC}$ measurements for different plasma conditions**

In chapter 3, we have shown that selectivity is lost when increasing the temperature of the electrodes (from 100 °C to 175 °C) and/or plasma power (from 10 W to 15 W). It was expected that this may be due to an increase in ion bombardment energy leading to the removal of Al-F bonds. In order to confirm or disprove this hypothesis, a variable frequency source was used to vary the ion energy by changing the frequency [25-27]. By increasing the frequency, one can decrease the average ion energy at a constant power, and see if for the non-selective plasma conditions, deposition on the non-growth  $AlO_x$  area can be prevented at lower ion bombardment energies.



For this purpose, the 13.56 MHz radio frequency voltage source was replaced by a function generator (AFG) along with a tunable matching box, a Bird RF power probe, and a Textronix HV voltage probe in order to measure the peak-to-peak voltage  $V_{PP}$  and the DC self-bias voltage  $V_{DC}$  on the powered electrode. For a sinusoidal voltage source, the time-averaged plasma potential  $V_{pl}$  can be estimated directly from  $V_{PP}$  and  $V_{DC}$  through the formula (4.1) [28-31]:

$$V_{pl} = \frac{1}{2} \left( \frac{1}{2} V_{PP} + V_{DC} \right) \quad (4.1)$$

This formula is true if one considers that (1) no voltage drop exists in the plasma bulk, (2) no sheath reversal, (3) the sheath completely collapses during the sinusoidal cycle and (4) the potential in the center of the plasma follows the applied voltage. Under those conditions, the maximum kinetic energy of ions arriving to the grounded electrode (ie the maximum ion bombardment energy) is approximately equivalent to the plasma potential.

A series of Ar/SiF<sub>4</sub>/H<sub>2</sub> plasma conditions were investigated for three frequencies: 10, 13.56 and 27 MHz<sup>3</sup>. We focused on a range of plasma conditions from the optimized AS-PECVD conditions, to those that lead to  $\mu$ c-Si deposition on both AlO<sub>x</sub> and SiO<sub>x</sub>N<sub>y</sub> areas, that is by increasing electrode temperature to 175 °C or plasma power to 15 W.

Fig. 4.14 summarizes the plasma potential for each plasma condition named above. We have also tracked the selectivity of the PECVD process on SiO<sub>x</sub>N<sub>y</sub>/AlO<sub>x</sub> samples on c-Si substrate, prepared in the configuration 1 (see section 2.1), for experimental conditions that are represented by a symbol. For the rest of the points, we only calculated the plasma potential as there was no sample loaded inside the reactor.

---

<sup>3</sup> We choose 27.12 MHz as it is the double of 13.56 MHz and 10 MHz was the smallest possible frequency to generate the plasma as we reached the limit values of the impedances in the matching box.

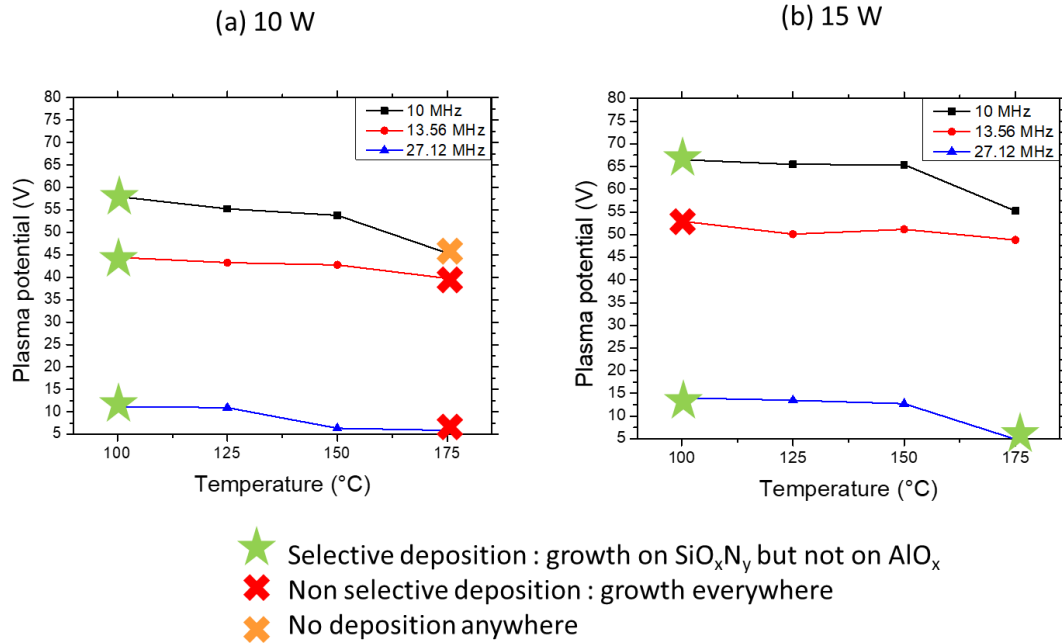


**Figure 4.14** Plasma potential as a function of four electrode temperature (100, 125, 150 and 175 °C) for three frequencies (10, 13.56 and 27.12 MHz) and for two plasma powers (a) 10 Watts and (b) 15 Watts

In Fig. 4.14a, plasma potentials are calculated for 100°C, 125°C, 150°C and 175°C substrate electrode temperatures, for a plasma power of **10 W**, 200/14/20 sccm of Ar/SiF<sub>4</sub>/H<sub>2</sub> gas flows, a pressure of 1.7 Torr and for three frequencies 10, 13.56 and 27.12 MHz. While, Fig. 4.14b shows the calculated plasma potentials for the same set of electrode temperatures but for a plasma power of **15 W**, 200/14/20 sccm of Ar/SiF<sub>4</sub>/H<sub>2</sub> gas flows, a pressure of 1.7 Torr and for three frequencies 10, 13.56 and 27.12 MHz. The star symbol stands for the selective deposition cases, the red X indicates the cases where Si grow on both AlO<sub>x</sub> and SiO<sub>x</sub>N<sub>y</sub> areas and the orange X indicates the cases where Si did not grow nor on AlO<sub>x</sub> or SiO<sub>x</sub>N<sub>y</sub> areas.

- **At 10 W**, for an electrode temperature of 100°C, selectivity is maintained even if the plasma potential changed. For 175 °C, (i)  $\mu\text{-Si}$  grows on AlO<sub>x</sub> area for both 13.56 MHz and 27.12 MHz frequencies. As already stated in chapter 2 (section 2.2.2), the increase of the excitation frequency leads to a reduction of ion energy. In this case, reducing ion bombardment energy (IBE) does not prevent the loss of selectivity. As a consequence, the non-selectivity effect that appears for those two cases is not simply linked to the IBE,

so reducing IBE cannot widen the process window. (ii) At 10 MHz, there is no deposition on either  $\text{AlO}_x$  nor  $\text{SiO}_x\text{N}_y$ . This may be because when reducing the excitation frequency to 10 MHz, the ion flux impinging the substrate is reduced while the energy is increased [25], affecting the nucleation of Si.

One can conclude from the 10W case that the determination of selectivity is dominated by electrode temperature.

- **At 15 W**, the situation is slightly different, and certainly less clear. In fact, for an electrode temperature of  $100^\circ\text{C}$ , selectivity is lost only for 13.56 MHz while the process is selective for 10 and 27.12 MHz. For  $175^\circ\text{C}$  and at 27.12 MHz excitation frequency,  $\mu\text{-Si}$  grows only on  $\text{SiO}_x\text{N}_y$  area without growing on  $\text{AlO}_x$  area. Thus, the use of variable frequencies plasma excitation enables us to extend the windows of area selective deposition process by PECVD.

From this small set of experiments, one can state that it is not the ion bombardment energy alone that determines the deposition on the normally non-growth area.

The connection between plasma power, electrode temperature and ion bombardment energies is not yet fully clear. Even if we could not confirm the direct relationship between IBE and the deposition on non-growth area, we can state that a change in excitation frequency can open up the process window.

### 4.3 Summary

In this chapter, we have attempted to identify the physical origins behind selective microcrystalline silicon deposition on  $\text{SiO}_x\text{N}_y$  areas while leaving  $\text{AlO}_x$  pristine. For this purpose, advanced surface analyses and plasma characterization were performed.

XPS and EDX chemical analyses showed that fluorine atoms are incorporated inside  $\text{SiO}_x\text{N}_y$  while there are Al-F bonds or  $\text{AlF}_3$  only on the  $\text{AlO}_x$  surface after  $\text{Ar}/\text{SiF}_4/\text{H}_2$  plasma under ASD conditions. Thus, we can picture the reactions on each surface (schematically represented in Fig. 4.15) as follow:

- (i) On  $\text{AlO}_x$  areas, the fluorination reaction forms a very strong bond (Al-F) that blocks etching or deposition on this area.
- (ii) On the contrary, on  $\text{SiO}_x\text{N}_y$  areas, plasma species create volatile or gaseous compounds when reacting with Si that are removed easily from the surface, leaving sites where growth can nucleate [32, 33].

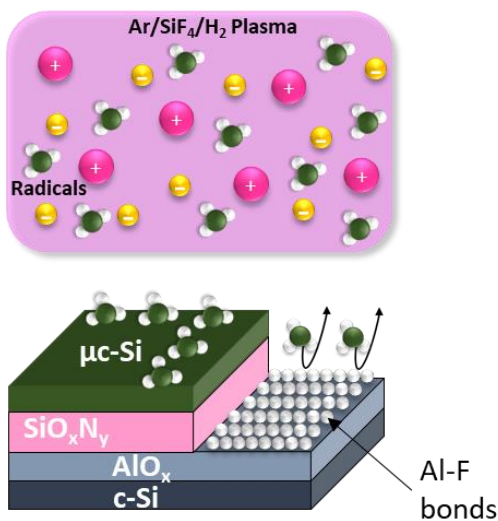


**Figure 4.15** Schematic representation of the reaction mechanism during AS-PECVD process.

Examining this mechanism, one can notice the crucial role of a fluorine-containing gas in the plasma chemistry for achieving area selective PECVD. The influence of fluorine-based plasma has been also previously studied for area selective atomic layer deposition and

atomic layer etching [34-37]. For example, R. Vallat et al. suggests that Si-F bonds passivate silicon substrates preventing TiO<sub>2</sub> growth and block surface reactions [34].

In addition to XPS and EDX surface characterization, the water contact angle measurement shows that SiO<sub>x</sub>N<sub>y</sub> is more hydrophilic than AlO<sub>x</sub> in their initial state and the fluorination of AlO<sub>x</sub> surface enhances its wettability. The presence of AlF<sub>3</sub> can be useful in optics or optoelectronics [38] or in MOS devices as it may enhance the memory window [38].

Regarding the plasma, two important points should be taken into account: (1) the fact that the two growth areas are located on the same c-Si substrate means the two areas are at the same temperature, and once in the plasma, will be at the same potential relative to the plasma [40, 41]. (2) One area cannot charge up more than the other (as could occur if one substrate was insulating and the other conductive [42]) means that the energy spectrum of the ion flux seen by the two surfaces should be very similar.

OES spectra shows that SiF<sub>3</sub> is an apparent growth precursor. Based on results from this technique, changing plasma power from 10W to 15 W did not affect relative plasma species densities in the plasma bulk because emission lines remain constant. But it may change density closer to the surface (we did not study this case because of technical difficulties to implement this in current reactor).

The variable frequency experiments allow us to consider that it is not simply because of ion bombardment energies deposition is occurring on AlO<sub>x</sub> area outside selective process windows. It is more likely due to species flux on the surfaces that increases with the increase of plasma power.

All those results indicate that our area selective plasma deposition process is strongly dependent on the interaction between plasma species and the surfaces i.e. the presence or not of Al-F bonds on the AlO<sub>x</sub> area. This indicates that our AS-PECVD have a great chance to be selective on small areas as long as the surface is composed of AlO<sub>x</sub> and SiO<sub>x</sub>N<sub>y</sub> surfaces, or their analogues.

## References

- [1] G. Akiki, M. Frégnaux, I. Florea, P. Bulkin, D. Daineka, S. Filonovich, M. Bouttemy, and E. V. Johnson, "Origin of area selective plasma enhanced chemical vapor deposition of microcrystalline silicon". *J. Vac. Sci. Technol. A* 39, 013201 (2021).
- [2] J.F. Moulder, W.F. Stickle, P.E. Sobol, K.D. Bomben, *Handbook of X-ray Photoelectron Spectroscopy*, Perkin Elmer Corporation, Physical Electronics Division: Eden Prairie, Minnesota, 1995.
- [3] A. Cuevas, M. J. Kerr and J. Schmidt, "Passivation of crystalline silicon using silicon nitride," 3rd World Conference on Photovoltaic Energy Conversion, 2003. Proceedings of, 2003, pp. 913-918 Vol.1.
- [4] Aberle, Armin G. "Overview on SiN surface passivation of crystalline silicon solar cells." *Solar energy materials and solar cells* 65.1-4 (2001): 239-248.
- [5] Seiffe, Johannes, et al. "Surface passivation of crystalline silicon by plasma-enhanced chemical vapor deposition double layers of silicon-rich silicon oxynitride and silicon nitride." *Journal of Applied Physics* 109.3 (2011): 034105.
- [6] G. Dingemans, P. Engelhart, R. Seguin, M. M. Mandoc, M. C. M. van de Sanden and W. M. M. Kessels, "Comparison between aluminum oxide surface passivation films deposited with thermal ALD, plasma ALD and PECVD," 2010 35th IEEE Photovoltaic Specialists Conference, 2010, pp. 003118-003121, doi: 10.1109/PVSC.2010.5614508.
- [7] Benick, Jan, et al. "Thermal stability of the Al<sub>2</sub>O<sub>3</sub> passivation on p-type silicon surfaces for solar cell applications." *physica status solidi (RRL)–Rapid Research Letters* 3.7-8 (2009): 233-235.
- [8] Hoex, B., J. Schmidt, R. Bock, P. P. Altermatt, M. C. M. Van De Sanden, and W. M. M. Kessels. "Excellent passivation of highly doped p-type Si surfaces by the negative-charge-dielectric Al<sub>2</sub>O<sub>3</sub>." *Applied Physics Letters* 91, no. 11 (2007): 112107.

- [9] K. Roodenko, M.D. Halls, Y. Gogte, O. Seitz, J.F. Veyan, and Y.J. Chabal, "Nature of Hydrophilic Aluminum Fluoride and Oxyaluminum Fluoride Surfaces Resulting from XeF<sub>2</sub> Treatment of Al and Al<sub>2</sub>O<sub>3</sub>". *J. Phys. Chem. C* 115, 21351 (2011).
- [10] M. Mertens, M. Mohr, K. Brühne, H.J. Fecht, M. Łojkowski, W. Świąszkowski, and W. Łojkowski, "Patterned hydrophobic and hydrophilic surfaces of ultra-smooth nanocrystalline diamond layers", *Appl. Surf. Sci.* 390, 526 (2016).
- [11] X. Liu, H. Shen, J. Liu, J. Zhang, Y. Chen, Z. Zhang, F. Zhang, N. Guan, D. Zhao, and Z. Jin, "A green, maskless, and universal preparation method for patterned surfaces on various metal substrates", *Appl. Surf. Sci.* 514, 145838 (2020).
- [12] N. Awaya and Y. Arita, "Selective Deposition of Silicon Oxide and Its Application", *Jpn. J. Appl. Phys.*, 25, L24 (1986).
- [13] N. Awaya and Y. Arita, "Selective Deposition of Silicon Oxide Using a Plasma-Fluorinated Resist Mask", *Jpn. J. Appl. Phys.*, 27, 1172 (1988).
- [14] Y. Zhang, E.H. Discekici, R.L. Burns, M.H. Somervell, C.J. Hawker, and C.M. Bates, "Single-Step, Spin-on Process for High Fidelity and Selective Deposition", *ACS Appl. Polym. Mater.* 2, 481 (2020).
- [15] A.A. Ogwu, T.I.T. Okpalugo, and J.A.D. McLaughlin, "The effect of PECVD plasma decomposition on the wettability and dielectric constant changes in silicon modified DLC films for potential MEMS and low stiction applications", *AIP Adv.* 2, (2012).
- [16] A. Ogwu and T.H. Darma, "Optical and surface energy probe of Hamaker constant in copper oxide thin films for NEMS and MEMS stiction control applications", *Sci. Rep.* 11, 1 (2021).
- [17] N. Mutsukura, M. Ohuchi, S. Satoh and Y. Machi, "The analyses of an SiF<sub>4</sub> plasma in an R.F. glow discharge for preparing fluorinated amorphous silicon thin films", 109, 47 (1983).
- [18] Henry U. LEE: and John P. DENEUVILLE Materials, "LIF AND OES DETECTION OF RADICAL SPECIES IN SiF<sub>4</sub> + H<sub>2</sub> PLASMAS", *Journal of Non-Crystalline Solids* 66 (1984) 39-44

- [19] Junkang Wang, “Novel concepts in the PECVD of silicon thin films: from plasma chemistry to photovoltaic device applications”, PhD thesis, Ecole Polytechnique, Université Paris-Saclay
- [20] J.W. Coburn and M. Chen, “Optical emission spectroscopy of reactive plasmas: A method for correlating emission intensities to reactive particle density”, *J. Appl. Phys.* 51, 3134 (1980).
- [21] G. Bruno, P. Capezzuto, and G. Cicala, “rf glow discharge of SiF<sub>4</sub>-H<sub>2</sub> mixtures: Diagnostics and modeling of the a-Si plasma deposition process”, *Journal of Applied Physics* 69, 7256 (1991)
- [22] Jie Ma, Michael N. R. Ashfold, and Yuri A. Mankelevich, “Validating optical emission spectroscopy as a diagnostic of microwave activated CH<sub>4</sub>/Ar/H<sub>2</sub> plasmas used for diamond chemical vapor deposition”, *J. Appl. Phys.* 105, (2009).
- [23] B.B. Sahu and J.G. Han, “Comparison of plasma excitation, ionization, and energy influx in single and dual frequency capacitive discharges”, *Phys. Plasmas* 23, 1 (2016).
- [24] W.L. Wiese, J.W. Brault, K. Danzmann, V. Helbig, and M. Kock, “Unified set of atomic transition probabilities for neutral argon”, *Phys. Rev. A* 39, 2461 (1989).
- [25] M. Heintze, R. Zedlitz, and G.H. Bauer, “Analysis of high-rate a-Si:H deposition in a VHF plasma”, *J. Phys. D. Appl. Phys.* 26, 1781 (1993).
- [26] S Oda, “Frequency effects in processing plasmas of the VHF band”, *Plasma Sources Sci. Technol.* 2, 26, (1993).
- [27] Kim, K.S., Kim, K.H., Ji, Y.J. et al. Silicon Nitride Deposition for Flexible Organic Electronic Devices by VHF (162 MHz)-PECVD Using a Multi-Tile Push-Pull Plasma Source. *Sci Rep* 7, 13585 (2017). <https://doi.org/10.1038/s41598-017-14122-4>
- [28] Brian Chapman. “Glow Discharge Processes: Sputtering and Plasma Etching”. New York, Wiley, 1980. (see p. 76)
- [29] W. Coburn, D.E. Horne, S. Jose, H. Keuer, and H. Junction, “Plasma potentials of 13.56-MHz rf argon glow discharges in a planar system”, 59 (1984).



- [30] M.J. Kushner, “Distribution of ion energies incident on electrodes in capacitively coupled rf discharges”, *J. Appl. Phys.* 58, 4024 (1985).
- [31] D. Gahan, S. Daniels, C. Hayden, P. Scullin, D. O’Sullivan, Y.T. Pei, and M.B. Hopkins, “Ion energy distribution measurements in rf and pulsed dc plasma discharges”, *Plasma Sources Sci. Technol.* 21, (2012).
- [32] K. Shinoda, M. Izawa, T. Kanekiyo, K. Ishikawa, M. Hori, Thermal cyclic etching of silicon nitride using formation and desorption of ammonium fluorosilicate, *Appl. Phys. Express.* 9 (2016) 3–6.
- [33] D. Humbird, D.B. Graves, Atomistic simulations of spontaneous etching of silicon by fluorine and chlorine, *J. Appl. Phys.* 96 (2004) 791–798.
- [34] R. Vallat, R. Gassilloud, O. Salicio, K. El Hajjam, G. Molas, B. Pelissier, C. Vallée, Area selective deposition of TiO<sub>2</sub> by intercalation of plasma etching cycles in PEALD process: A bottom up approach for the simplification of 3D integration scheme, *J. Vac. Sci. Technol. A.* 37 (2019) 020918.
- [35] Zywojko, D.R., Zandi, O., Faguet, J., Abel, P.R. and George, S.M., “Selective atomic layer etching of HfO<sub>2</sub> over silicon by precursor and substrate-dependent selective deposition”, *Chem. Mater.* (2020), 32, 23, 10055–10065.
- [36] K.-Y. Lin, C. Li, S. Engelmann, R.L. Bruce, E.A. Joseph, D. Metzler, and G.S. Oehrlein, “ZrO<sub>2</sub> Monolayer as a Removable Etch Stop Layer for Thermal Al<sub>2</sub>O<sub>3</sub> Atomic Layer Etching Using Hydrogen Fluoride and Trimethylaluminum”, *J. Vac. Sci. Technol. A* 38, 032601 (2020).
- [37] K. Roodenko, M.D. Halls, Y. Gogte, O. Seitz, J.F. Veyan, and Y.J. Chabal, “In Situ Monitoring of Surface Reactions during Atomic Layer Etching of Silicon Nitride Using Hydrogen Plasma and Fluorine Radicals”. *J. Phys. Chem. C* 115, 21351 (2011).
- [38] M.F.J. Vos, H.C.M. Knoop, W.M.M. Kessels, and A.J.M. MacKus, “Reaction Mechanisms during Atomic Layer Deposition of AlF<sub>3</sub> Using Al(CH<sub>3</sub>)<sub>3</sub> and SF<sub>6</sub> Plasma”. *J. Phys. Chem. C* 125, 3913 (2021).

[39] S.W. Kim, B.J. Park, S.K. Kang, B.H. Kong, H.K. Cho, G.Y. Yeom, S. Heo, and H. Hwang, “Characteristics of Al<sub>2</sub>O<sub>3</sub> gate dielectrics partially fluorinated by a low energy fluorine beam”, *Appl. Phys. Lett.* 93, 1 (2008)

[40] K.S. Sree Harsha, *Principles of Vapor Deposition of Thin Films*, Elsevier, 2005, Chapter 4.

[41] Wilfried G.J.H.M. Van Sark, “Methods of deposition of hydrogenated amorphous silicon for device applications”, *Thin Films and Nanostructures*, vol. 30, Academic Press, 2002.

[42] J. Cazaux, “Recent developments and new strategies in scanning electron microscopy”, *J. Microsc.* 217 (2005) 16–35.



# Chapter 5

## Selective processes for patterned substrates

5.1	Challenges in the fabrication of patterned substrates .....	120
5.1.1	Recall lithography steps .....	120
5.1.2	Contamination .....	121
5.1.3	Solutions to resist contamination .....	122
5.1.4	Sensitivity to process details .....	125
5.2	ASD on patterned substrates: .....	127
5.2.1	Chemical and topographical characterization .....	127
a)	Contact angle measurement .....	127
b)	Atomic Force Microscopy.....	129
c)	X-ray Photoelectron Spectroscopy.....	131
5.2.2	Area selective $\mu\text{c-Si}$ on patterned substrate with different dimension.....	138
a)	Far from pattern area .....	140
b)	Reduced $\text{SiO}_x\text{N}_y$ feature size.....	142
5.3	Summary .....	148
	References .....	150

## **5.1 Challenges in the fabrication of patterned substrates**

Throughout the previous chapters, area selective deposition and its origin have been demonstrated and investigated for deposition on  $\text{SiO}_x\text{N}_y$  without any deposition on  $\text{AlO}_x$  and for samples prepared in Configuration 1. This chapter will focus on the application of AS-PECVD process to  $\text{AlO}_x/\text{SiO}_x\text{N}_y$  patterns, i.e. Configuration 2, defined by lithography. The first part is dedicated to the challenges faced during the fabrication of such patterns in particular the contamination that potentially inhibits the selective growth of  $\mu\text{-Si}$  on  $\text{SiO}_x\text{N}_y$ . The following part includes the characterization of the growth on different feature dimensions.

### **5.1.1 Review of photolithography steps**

Patterns of aluminum oxide and silicon oxynitride were prepared by photolithography in Thales TRT clean room on the Ecole Polytechnique campus. The main steps used are as follows:

1. Spin coating of SPR 700 1.0<sup>TM</sup> positive photoresist on the silicon wafer coated with 50 nm of  $\text{AlO}_x$  and 70 nm of  $\text{SiO}_x\text{N}_y$  at 3000 rpm spin speed for 30 seconds.
2. Soft bake of the photoresist at 110°C for 1 minute on a hot plate.
3. Exposition of the photoresist to a UV lamp for 3 or 6 seconds depending on the minimum feature size of the photomask
4. Dissolution (development) of soluble area of photoresist (area exposed to UV light) in MICROPOSIT® MF-319® developer for 20 to 5 seconds depending on the chosen UV exposure time
5. Rinse in deionized water (DW) and drying the surface
6. Selective etching of  $\text{SiO}_x\text{N}_y$  area uncovered with photoresist by  $\text{SF}_6$  plasma in the reactive ion etching (RIE) system for 1 minute and a half.
7. Removal of photoresist from the surface by acetone and isopropanol

Those steps as well as the resulting sample are presented in Fig. 5.1.

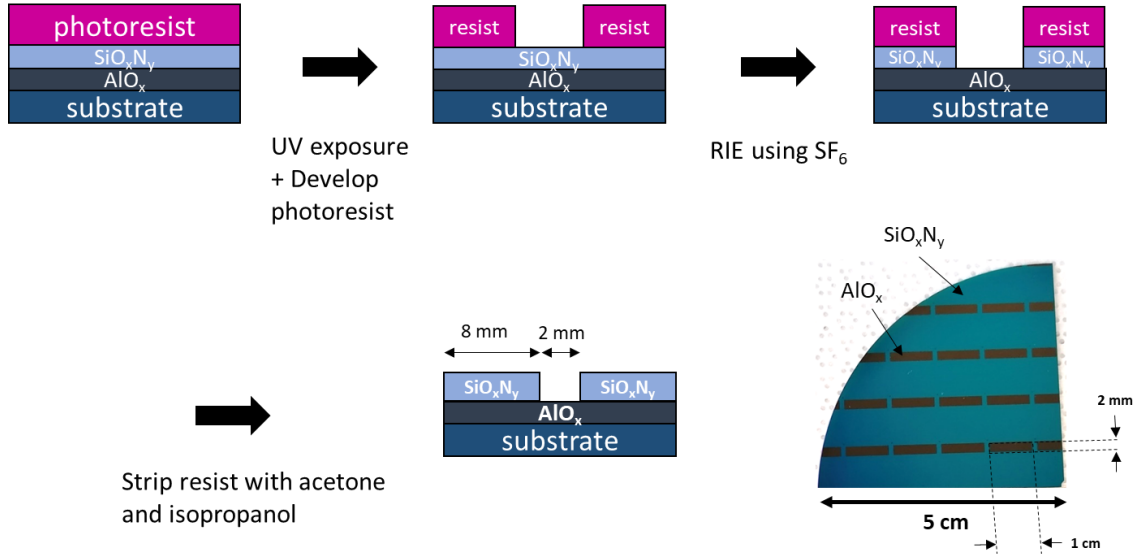


**Figure 5.1** Photolithography process used for the fabrication of  $\text{AlO}_x/\text{SiO}_x\text{N}_y$  patterns. The photo represents a top view of the resulting sample.

### 5.1.2 Contamination

During RIE etching, photoresist may get heavily cross-linked due to high temperatures, DUV-radiation, and ion bombardment resulting from the plasma [1]. This will prove problematic in photoresist removal. An example of a contaminated sample with photoresist traces is shown in Fig. 5.2. This photo is of a sample after lithography steps and after 3 minutes of  $\text{Ar}/\text{SiF}_4/\text{H}_2$  plasma under AS-PECVD conditions. It is clear that the presence of resist traces on  $\text{AlO}_x$  areas (black rectangles) affect the selectivity by enhancing the growth of  $\mu\text{c-Si:H}$  on those intended to be non-growth areas.

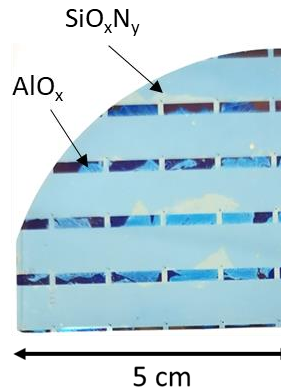


**Figure 5.2** Example of a contaminated substrate from photolithography.

### 5.1.3 Solutions to resist contamination

In order to suppress the contamination resulting from lithography, we tried numerous methods. Firstly, we changed the photoresist chemistry from SPR 700 1.0® to S1805® and n-LOF®2020. Nevertheless, it was hard to remove the alternative resists by acetone and isopropanol. Even when acetone was replaced by another solvent; N-Methyl-2-pyrrolidone (NMP), the resist traces remain on the substrate, and especially on  $\text{AlO}_x$  areas.

The second solution was to make a hard mask in order to avoid the exposure of the resist to the  $\text{SF}_6$  plasma. The method is described in Fig. 5.3. It starts with a thermal evaporation of copper on top of a substrate (including layer stack), resist patterning, and then wet etching in a diluted ferric chloride ( $\text{FeCl}_3$ ) solution in  $\text{H}_2\text{O}$ . This solution is known to selectively etch a few metals, particularly copper [2]. Once the hard mask of copper is created,  $\text{SiO}_x\text{N}_y$  is etched selectively by  $\text{SF}_6$  plasma without impacting  $\text{AlO}_x$  or Cu. The Cu mask is finally removed by  $\text{FeCl}_3$  solution. Unfortunately, using this method, we introduced additional contamination sources on the surface coming from the Cu removal and the multiple other processing steps. Selectivity was not improved.

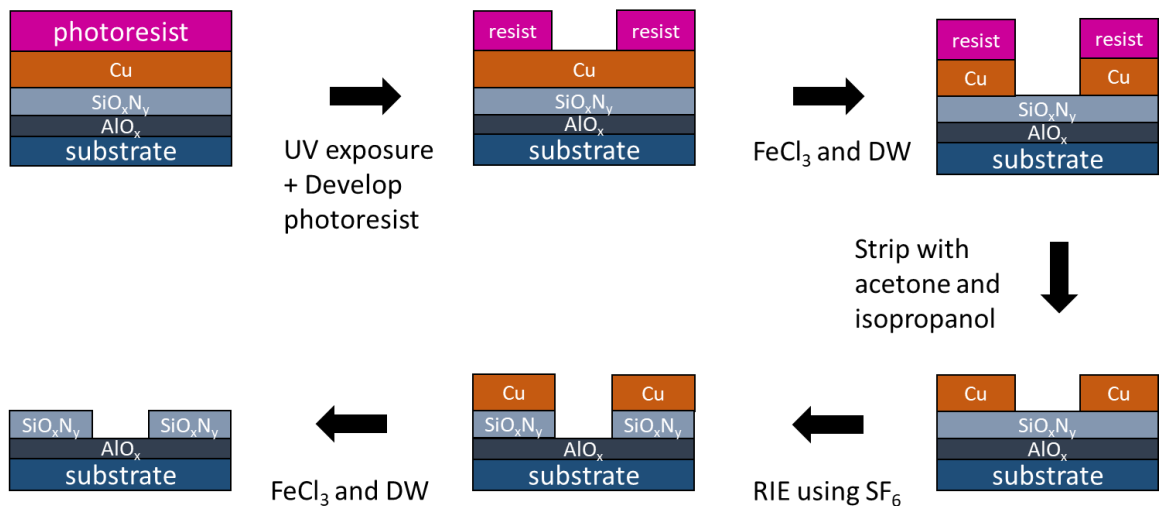


**Figure 5.3** Photolithography steps in case of lift off process.

After the failure of the previous solutions, we turned back to the initial lithography process (using SPR 700 1.0® positive resist) and included an additional step of  $\text{O}_2$  plasma surface treatment. Indeed,  $\text{O}_2$  plasma is known to remove organic contamination from the

surface as it oxidizes the organic resist polymers and removes them as volatiles, with practically no residue [1, 3]. Therefore,  $\text{AlO}_x/\text{SiO}_x\text{N}_y$  patterned substrates were treated with  $\text{O}_2$  plasma for 5 minutes in VENUS reactor.

Using the  $\text{O}_2$  plasma, we successfully removed photoresist traces. Unfortunately, the plasma exposure apparently also changed the surface properties of the  $\text{SiO}_x\text{N}_y$ , and this was manifested by a loss of silicon growth on top of  $\text{SiO}_x\text{N}_y$ , resulting in no growth whatsoever. In Fig. 5.4, a photo of a patterned substrate after 5 minutes  $\text{O}_2$  plasma and 20 minutes of  $\text{Ar}/\text{SiF}_4/\text{H}_2$  AS-PECVD process shows no any difference between before and after AS-PECVD (to be compared to the difference between Fig. 5.1 and 5.4).

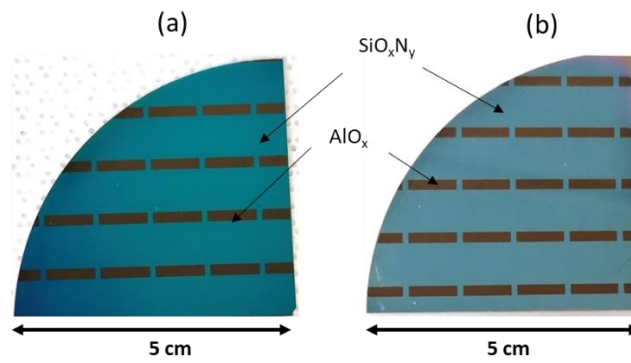


**Figure 5.4**  $\text{AlO}_x/\text{SiO}_x\text{N}_y$  patterns (a) before and (b) after 5 minutes of  $\text{O}_2$  plasma and 20 minutes of AS-PECVD process. No deposition on either growth nor non-growth areas

As an alternative to  $\text{O}_2$  plasma treatment, patterned substrates surfaces were treated with  $\text{H}_2$  plasma, as this is also known to remove organic contaminations from surfaces [4].  $\text{H}_2$  plasma treatment has been performed in a Nanomaster NRE 3500 parallel plate RIE system<sup>1</sup>. Plasma treatment time was varied between 40 minutes, 1 hour and 2 hours. The results are either no deposition on  $\text{AlO}_x$  or  $\text{SiO}_x\text{N}_y$  areas (similar to Fig. 5.4) or deposition on both areas (Fig. 5.5). In either case, area selective deposition could not be achieved.

The ultimate solution was to combine plasma treatments, and use an  $\text{O}_2$  plasma, followed by either  $\text{H}_2$ ,  $\text{SF}_6$  or  $\text{N}_2$  plasmas. Deposition on both growth and non-growth areas was obtained when surfaces were treated with 10 minutes of  $\text{O}_2$  plasma in VENUS then 20 minutes of  $\text{H}_2$  plasma in RIE. Same result was found for 5 minutes  $\text{O}_2$  plasma treatment and 40 seconds of  $\text{SF}_6$  plasma etching.

---

<sup>1</sup> More details about RIE system are found in reference [5]



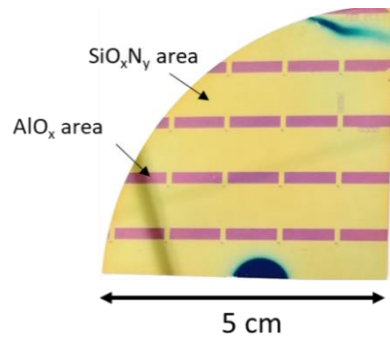


**Figure 5.5** After 2 hours of  $H_2$  plasma treatment and 20 minutes  $Ar/SiF_4/H_2$  for silicon deposition

Finally and fortuitously, selective deposition on  $SiO_xN_y$  vs  $AlO_x$  areas is achieved when using 5 minutes  $O_2$  plasma followed by 3 minutes  $N_2$  plasma surface pre-treatment, both done in the VENUS ECR-PECVD reactor.

Fig. 5.6a shows an example of selective  $\mu c$ -Si deposition on  $AlO_x/SiO_xN_y$  patterns after  $O_2+N_2$  plasma pre-treatment and 20 minutes  $Ar/SiF_4/H_2$  AS-PECVD process. Fig. 5.6b and 5.6c are the SEM images on the region between  $AlO_x$  and  $SiO_xN_y$ . As seen in the images, Si nuclei are dense on the  $SiO_xN_y$  area and drop abruptly on the  $AlO_x$  area. Since we are not able to image a cross sectional view of the pattern, we cannot certainly assume if the microcrystalline silicon is growing in a “mushroom” shape on top of  $SiO_xN_y$  area [6].

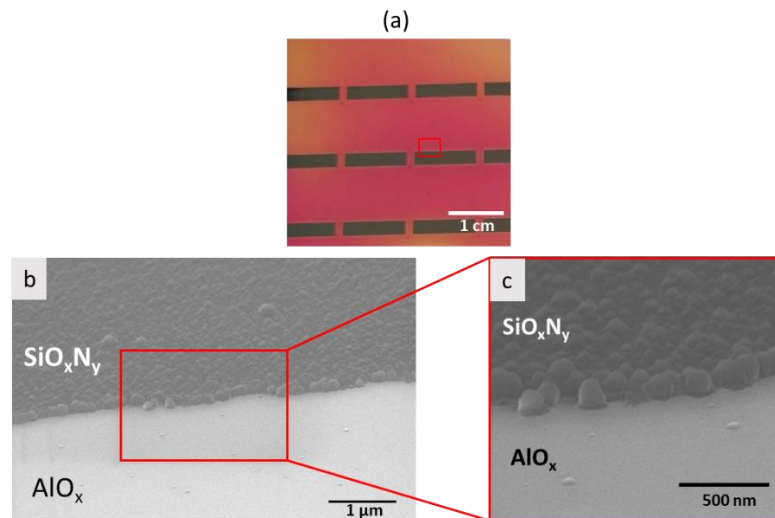


**Figure 5.6** (a) Photo of the  $AlO_x/SiO_xN_y$  patterns after 20 minutes of AS-PECVD process with its corresponding SEM images in different magnifications (b) and (c)

#### 5.1.4 Sensitivity to process details

### **a) Under etching**

Additional contamination has been identified for some cases even after O<sub>2</sub> and N<sub>2</sub> plasma surface pretreatment, and results in “unwanted” nuclei on the non-growth area. Notably, this occurs when the SF<sub>6</sub> plasma etching time is insufficient to fully etch silicon oxynitride. For example, by comparing Fig. 5.7a and 5.7b, we can notice that the density of the grains or nuclei on AlO<sub>x</sub> area after 3 minutes of SF<sub>6</sub> is less than that after 40 seconds of SF<sub>6</sub> plasma. It is likely that for 40 seconds of SF<sub>6</sub> plasma, some traces of SiO<sub>x</sub>N<sub>y</sub> remain on the AlO<sub>x</sub> area, which leads to the nucleation of silicon on top of AlO<sub>x</sub>.

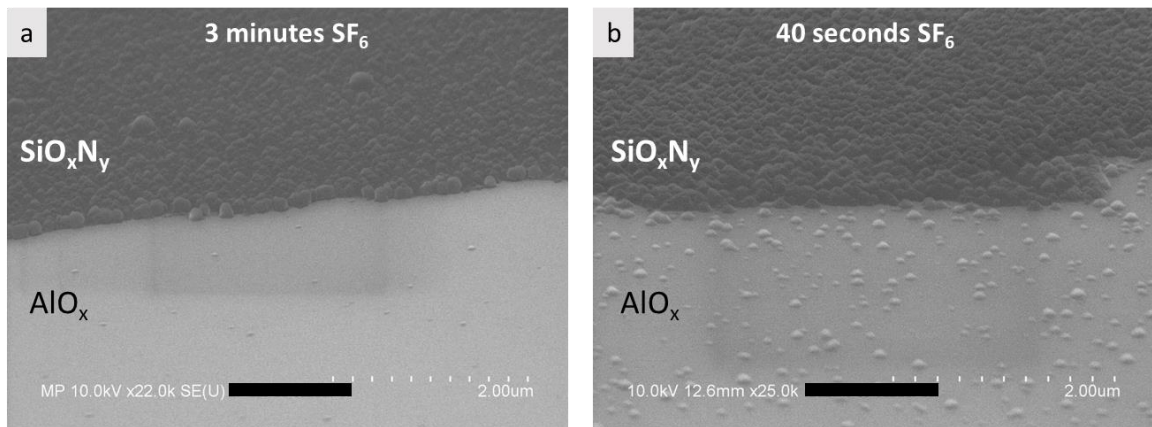


**Figure 5.7** SiO<sub>x</sub>N<sub>y</sub>/AlO<sub>x</sub> patterned samples for (a) 3 minutes and (b) 40 seconds SF<sub>6</sub> plasma etching time. Both samples were treated with 5 minutes O<sub>2</sub> plasma, 3 minutes N<sub>2</sub> plasma and 20 minutes of Ar/SiF<sub>4</sub>/H<sub>2</sub> plasma under AS-PECVD

### **b) Pattern sensitivity**

For the same O<sub>2</sub> and N<sub>2</sub> plasma surface pretreatment and under AS-PECVD conditions, it was observed that the selectivity outcome depends on the overall pattern design, especially relative areas of SiO<sub>x</sub>N<sub>y</sub> and AlO<sub>x</sub>, but on a macroscopic scale. For example, the two sample designs in figure 5.8, named Configuration 2A and Configuration 2B, show dramatically different results after plasma exposure. In configuration 2A<sup>2</sup>, μc-Si is deposited selectively

---

<sup>2</sup> Configuration 2A is the same as Configuration 2 in fig.5.6 (a)

on  $\text{SiO}_x\text{N}_y$  area, as desired, whereas in configuration 2B, under identical plasma conditions,  $\mu\text{-Si}$  does not grow on  $\text{SiO}_x\text{N}_y$  areas, nor on  $\text{AlO}_x$  areas.

It should be noted that the only difference between Conf.2A and Conf.2B is the photomask design used during photolithography process and the rest of the fabrication steps were exactly the same.

The dependence of the ASD process selectivity on the macroscopic substrate pattern remains one of the most confusing puzzles of this work. Despite many attempts to understand it, no clear physical explanation could be unveiled.

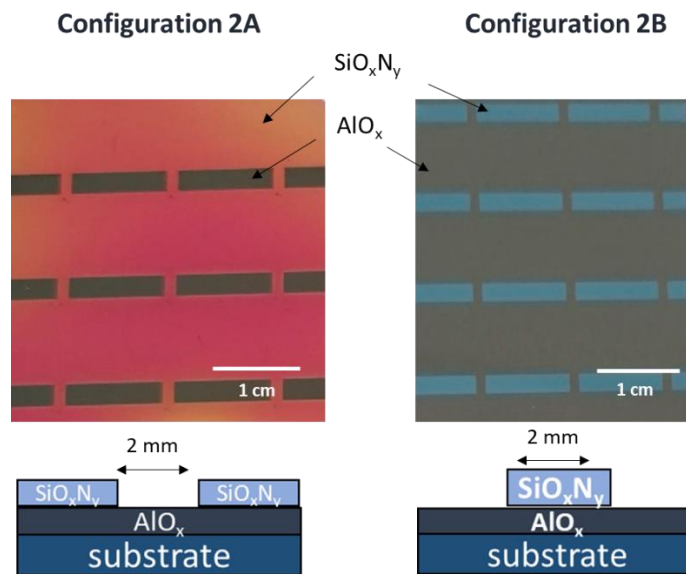


**Figure 5.8**  $\text{AlO}_x/\text{SiO}_x\text{N}_y$  patterns on c-Si substrate in configuration 2A (on the left) and Configuration 2B (on the right) after  $\text{O}_2$  and  $\text{N}_2$  plasma pretreatment followed by AS-PECVD process.

## 5.2 ASD on patterned substrates

It was shown so far that additional steps are needed to achieve selective deposition on patterned samples. This section is dedicated to the characterization of  $\text{SiO}_x\text{N}_y/\text{AlO}_x$  patterns for each plasma treatment in order to understand impact of those treatments on the

surfaces. For this purpose, contact angle measurements, atomic force microscopy, and X-ray photoelectron spectroscopy were performed on both growth and non-growth areas after each step, i.e. after the following consecutive steps: (1) photolithography, dry etching and wet cleaning, (2) 5 minutes O<sub>2</sub> plasma, (3) 3 minutes N<sub>2</sub> plasma and (4) Ar/SiF<sub>4</sub>/H<sub>2</sub> AS-PECVD. In addition, the ASD process on different SiO<sub>x</sub>N<sub>y</sub> pattern features will be studied.

## **5.2.1 Chemical and topographical characterization**

### **a) Contact angle measurement**

Water contact angle (WCA) has been measured on SiO<sub>x</sub>N<sub>y</sub> and AlO<sub>x</sub> areas after O<sub>2</sub> and N<sub>2</sub> plasma in order to check the impact of plasma pretreatment on their wettability. From Fig. 5.9, it is obvious that WCA is modified after each plasma treatment indicating a change in the chemical character of the SiO<sub>x</sub>N<sub>y</sub> surface. After O<sub>2</sub> plasma, the WCA decreased from 43° to 8° enhancing the wettability of SiO<sub>x</sub>N<sub>y</sub> surface and making the surface more hydrophilic. N<sub>2</sub> plasma increases again the WCA up to 25°. Thus, an O<sub>2</sub> plasma treatment followed by an N<sub>2</sub> plasma changes the wettability of SiO<sub>x</sub>N<sub>y</sub> in opposite ways.

On the level of area selective deposition, those two pretreatments also provide different results: while an O<sub>2</sub> plasma surface treatment prevents μc-Si selective growth on top of SiO<sub>x</sub>N<sub>y</sub> areas under AS-PECVD conditions, N<sub>2</sub> plasma after this final O<sub>2</sub> plasma helps to recover deposition on this same area. Consequently, N<sub>2</sub> plasma treatment do not somehow “reset” the surface to its initial state (before any plasma treatments) as the surface free energies are distinct. Yet, it modifies SiO<sub>x</sub>N<sub>y</sub> chemical character in a way to promote the nucleation of silicon.

Regarding AlO<sub>x</sub> area<sup>3</sup>, we measured WCA in configuration 2B. As shown in figure 5.8, WCA increased for every plasma treatment. It goes from 54° before any treatment to 68° after O<sub>2</sub> plasma reaching a value of 77° after O<sub>2</sub> and N<sub>2</sub> plasma. Those final WCA values

---

<sup>3</sup> We couldn't measure the water contact angle for AlO<sub>x</sub> in Configuration 2A because the liquid droplet drifts abruptly to the wider SiO<sub>x</sub>N<sub>y</sub> area. This problem could have been solved by reducing water droplet volume but it wasn't done due to the characteristics of the instruments

in the Configuration 2B are uncertain to be identical to that in Configuration 2B as the response to the Ar/SiF<sub>4</sub>/H<sub>2</sub> plasma under AS-PECVD conditions was different. Still it indicates that plasma treatments slightly reduce the hydrophilicity of AlO<sub>x</sub> surface and do not promote the growth of μc-Si thin film.

It should be noted that the effect of the O<sub>2</sub> plasma is opposite for both surfaces, as it enhances the wettability of SiO<sub>x</sub>N<sub>y</sub>, but reduces it for AlO<sub>x</sub> areas.

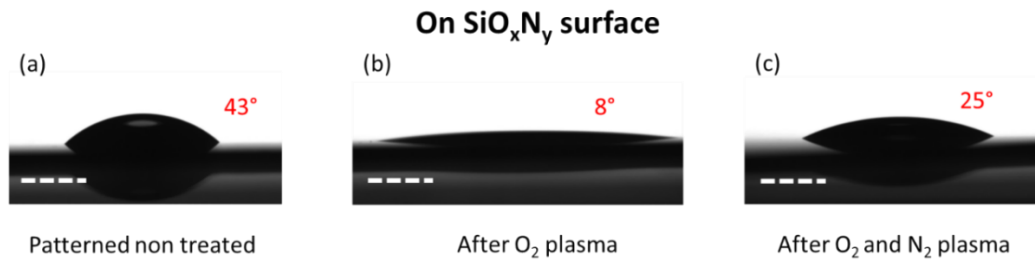


**Figure 5.9** Water contact angle measurement on top of SiO<sub>x</sub>N<sub>y</sub> surface for patterned sample in configuration 1 (a) before any plasma treatment, (b) after 5 minutes O<sub>2</sub> plasma and (c) after 3 minutes of N<sub>2</sub> plasma following 5 minutes O<sub>2</sub> plasma (scale bar: 200 μm)

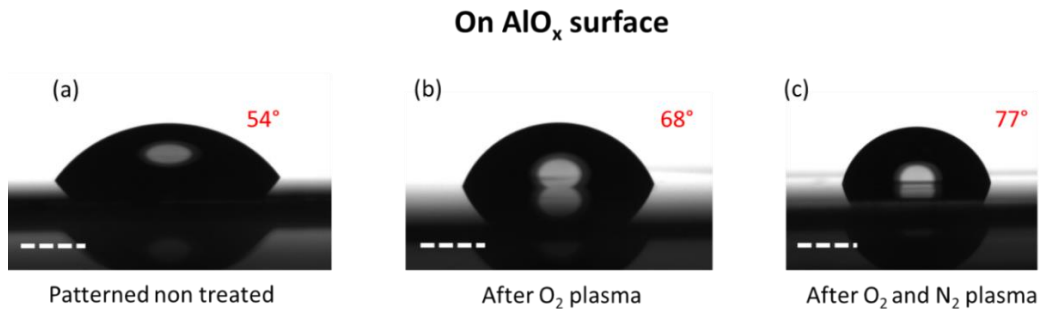


**Figure 5.10** Water contact angle measurement on top of AlO<sub>x</sub> surface for patterned sample in configuration 2 (a) before any plasma treatment, (b) after 5 minutes O<sub>2</sub> plasma and (c) after 3 minutes of N<sub>2</sub> plasma following 5 minutes O<sub>2</sub> plasma (scale bar: 200 μm)

## **b) Atomic Force Microscopy**

In addition to contact angle measurements, AFM was used to track any change in surface RMS roughness after different plasma treatments, as this may also impact growth and contact angle. The AFM images of both  $\text{SiO}_x\text{N}_y$  and  $\text{AlO}_x$  areas, along with their corresponding RMS values, are shown in figure 5.11 for the following cases: (a) on pattern after lithography, (b) on pattern after  $\text{O}_2$  plasma and (c) on pattern after  $\text{O}_2$  and  $\text{N}_2$  plasma. The measured area is  $5 \times 5 \mu\text{m}^2$ .

On the  $\text{SiO}_x\text{N}_y$  area, there is no significant change in the roughness after pattern fabrication (including photolithography and dry etching) as well as after all plasma treatments. This means that the surface modification (namely the wettability) can be only explained as a chemical change, not a physical one.

On the  $\text{AlO}_x$  area, the RMS roughness is relatively high after pattern fabrication (2.24 nm) compared to after plasma pretreatment (0.5 nm). This can be attributed to the photoresist traces resulting from the sample fabrication steps. However, the roughness did not change after  $\text{O}_2$  and  $\text{O}_2+\text{N}_2$  plasma pretreatment (similar to the  $\text{SiO}_x\text{N}_y$  area).

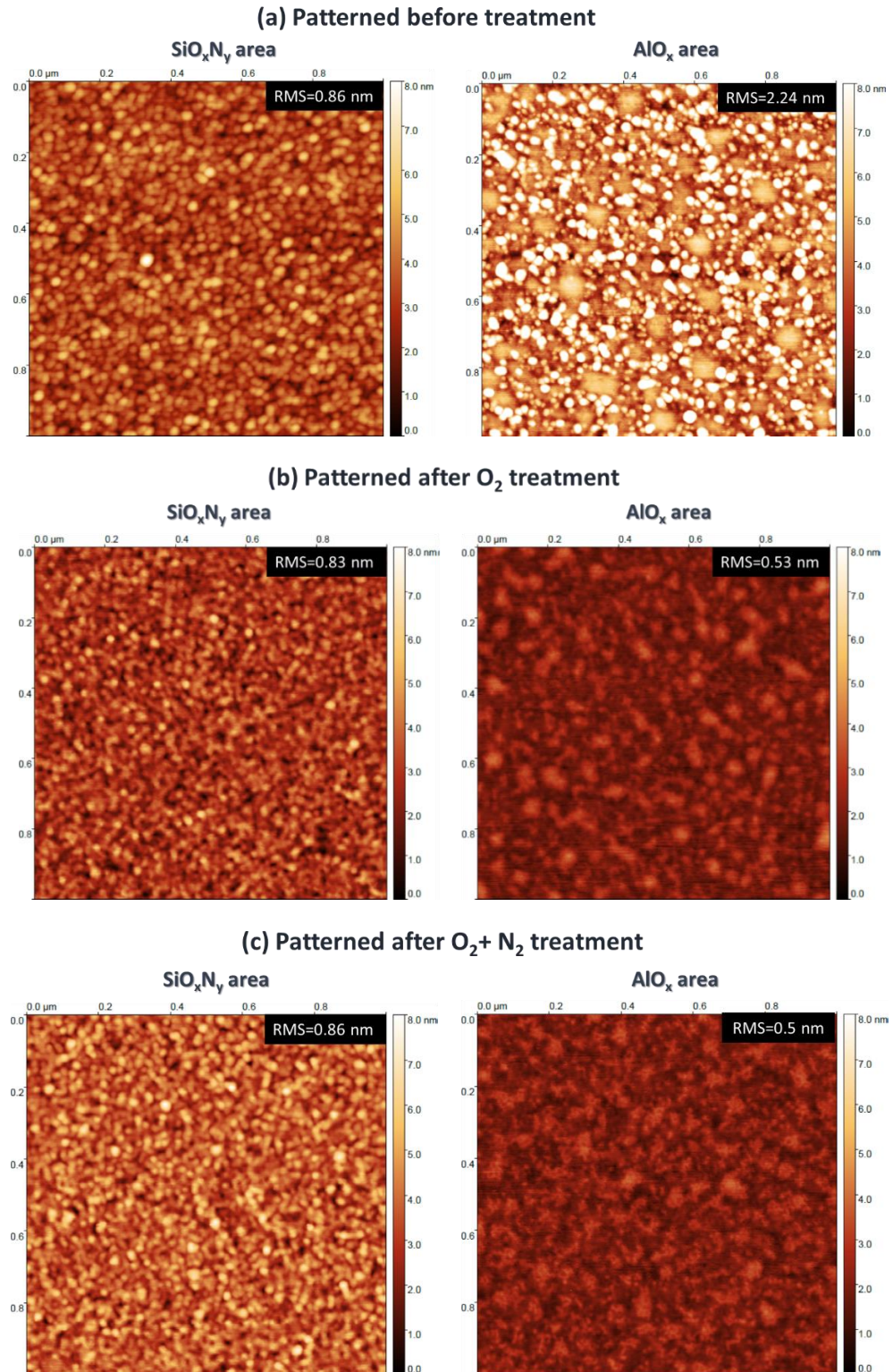


**Figure 5.11** AFM images of SiO<sub>x</sub>N<sub>y</sub> (left) and AlO<sub>x</sub> (right) after (a) photolithography, (b) after O<sub>2</sub> plasma and (c) after O<sub>2</sub> and N<sub>2</sub> plasmas pretreatment. The maximum scale height was set to 8 nm for all images.

### **c) X-ray photoelectron spectroscopy**

All the results presented so far indicate that the surfaces are chemically modified after each plasma treatment, so XPS chemical analyses have also been performed on  $\text{SiO}_x\text{N}_y$  surfaces at each step. For this study, we compare the atomic composition and bonding of four samples: (1) as-deposited  $\text{SiO}_x\text{N}_y$  before lithography, (2) patterned sample after the final step of photolithography procedure (after acetone and isopropanol rinsing), (3) patterned sample after 5 minutes of  $\text{O}_2$  plasma in VENUS and (4) patterned sample after 5 minutes of  $\text{O}_2$  plasma followed by 3 minutes of  $\text{N}_2$  plasma, both in VENUS. The atoms detected on the  $\text{SiO}_x\text{N}_y$  surface along with their composition in atomic percentage (%) are presented in table 5.1.

Firstly, one notes carbon composition (represented by the C1s peak) is 8.4% before lithography and it increases after lithography, as the surface was exposed to multiple chemical solutions. As expected, carbon traces are attenuated after  $\text{O}_2$  plasma. Their content increases again after the  $\text{N}_2$  plasma treatment (but not to as much as it was before any treatment).

Secondly, F is detected on patterned substrates in only minor quantities (<0.4%), which indicates that the photoresist provides a good protection for the  $\text{SiO}_x\text{N}_y$  layer from plasma species during  $\text{SF}_6$  plasma etching. In addition, the Si2p content remains constant for the different samples. Finally, from N and O atomic percentage variations, we could asset that the  $\text{O}_2$  plasma inserts O in the surface, as O percentage goes from 21.10% to 54.8%. Furthermore, the  $\text{N}_2$  plasma inserts N, since N1s increases after  $\text{N}_2$  plasma (N percentage goes from 9.6% before  $\text{N}_2$  plasma to 21.4% after  $\text{N}_2$  plasma). Accordingly, O atoms are replaced by N atoms after  $\text{N}_2$  plasma treatment.

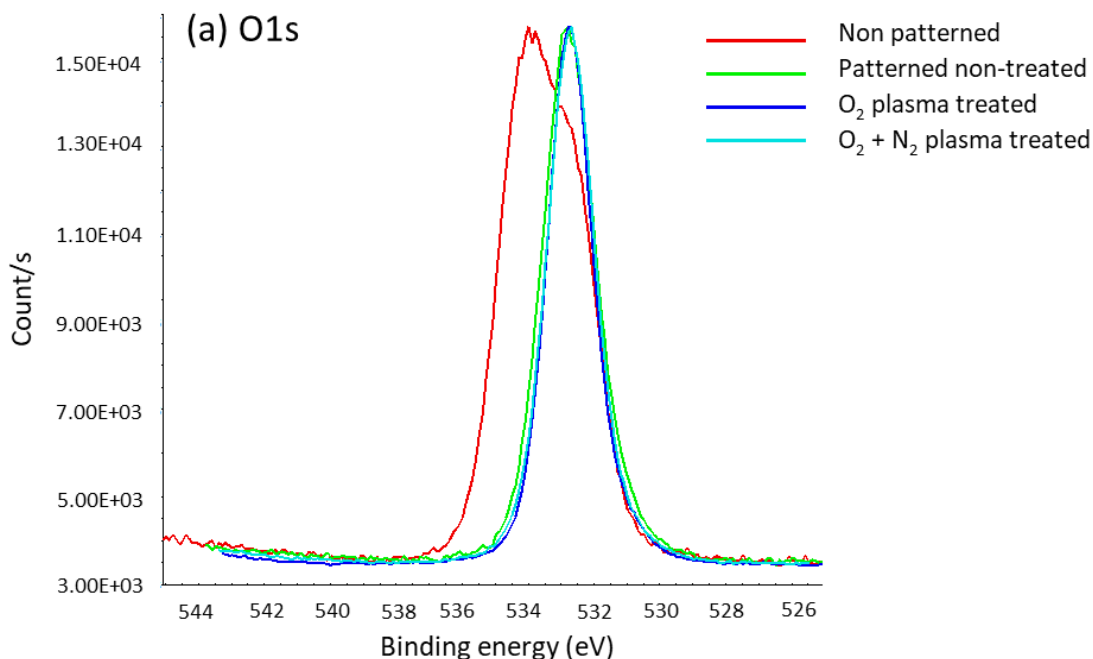
Similarly, a comparison of high resolution spectra has been carried out for the four samples named above. We selected O1s, N1s and Si2p photoelectron peaks and shown in figure 5.12. The shift of the O1s, N1s and Si2p peaks on blanket  $\text{SiO}_x\text{N}_y$  surface (red peaks) corresponds to charge effect linked to the dielectric nature of the material [7]. We can notice from Si2p photoelectron peaks (Fig. 5.12c) that the peak position is shifted to higher or lower energies depending on the treatment applied to the surface. After pattern fabrication i.e. after



lithography, this charge effect is reduced, and the O/N ratio is 0.61 for the SiO<sub>x</sub>N<sub>y</sub> layer. After O<sub>2</sub> plasma the O/N ratio is drastically increased from 0.61 to 5.70. In other words, O<sub>2</sub> plasma inserts O in the SiO<sub>x</sub>N<sub>y</sub> layer. After N<sub>2</sub> plasma, O/N ratio becomes 1.83. All this indicates that the surface composition and the chemistry of SiO<sub>x</sub>N<sub>y</sub> evolves after each plasma treatment, and on the basis of previous observations, the amount of N in the layer is crucial in promoting the selective growth of the μc-Si layer.

	C1s	F1s	N1s	O1s	Si2p	Si/N+O	O/N
<b>Non patterned</b>	8.4	-	36.5	21.5	33.7	0.58	0.59
<b>Patterned non treated</b>	11.7	0.3	34.6	21.1	32.3	0.58	0.61
<b>After 5 minutes of O<sub>2</sub> plasma</b>	3.2	-	9.6	54.8	32.4	0.50	5.70
<b>After 5 mins O<sub>2</sub> plasma followed by 3 mins N<sub>2</sub> plasma</b>	5.7	0.1	21.4	39.2	33.5	0.55	1.83

**Table 5.1** Atomic composition (in %) from XPS survey on SiO<sub>x</sub>N<sub>y</sub> surface for patterned samples in configuration 2



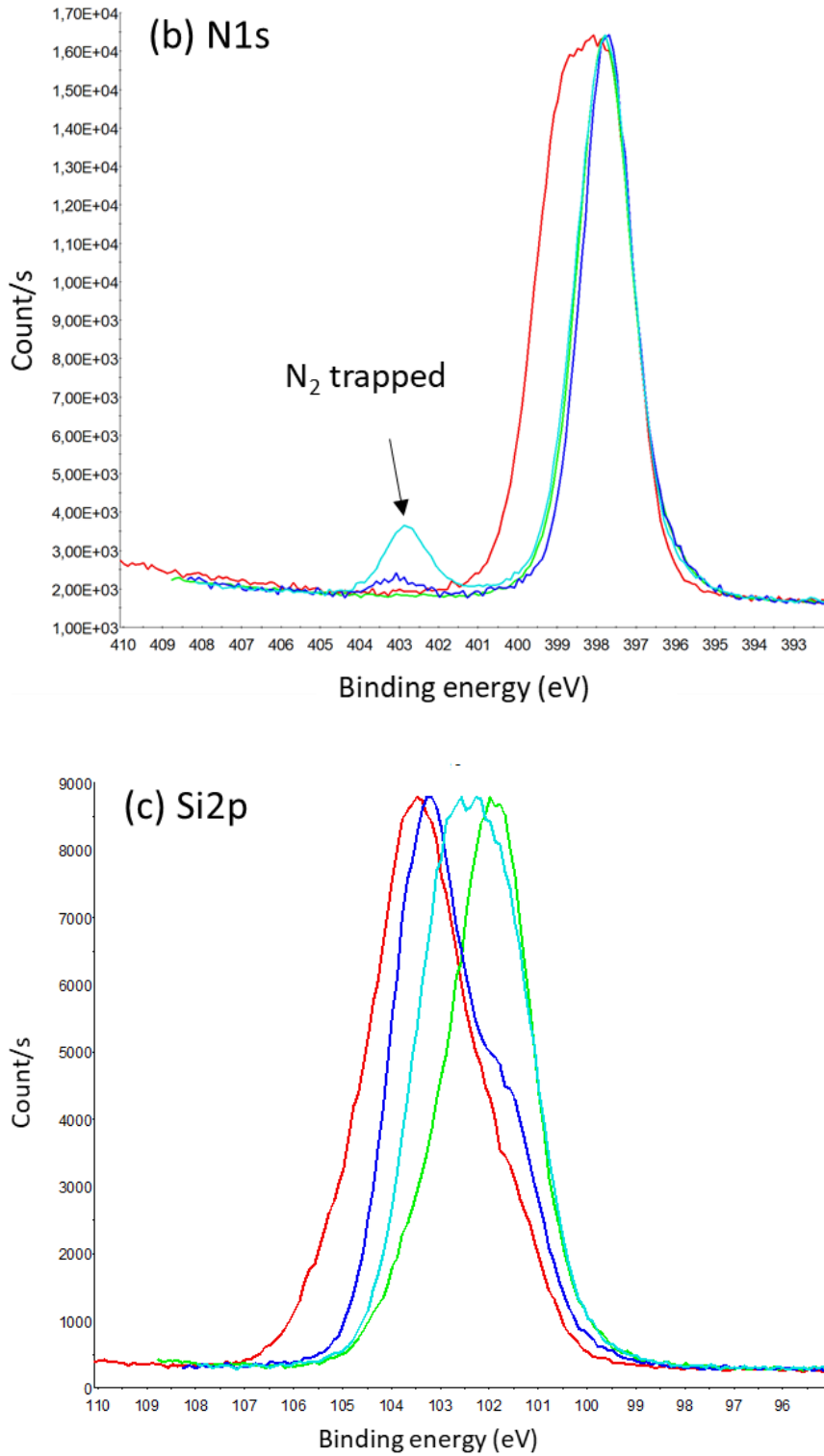


**Figure 5.12** (a) O1s, (b) N1s, (c) Si2p photoelectron spectra on as-deposited blanket SiO<sub>x</sub>N<sub>y</sub> (red) and on SiO<sub>x</sub>N<sub>y</sub> pattern fabricated by lithography before any treatment (green), after O<sub>2</sub> plasma

treatment (dark blue) and after O<sub>2</sub> and N<sub>2</sub> plasma treatments (light blue). Spectra are auto-scaled to simplify the interpretation

The same XPS analysis has been done on three AlO<sub>x</sub> areas: (1) patterned sample (i.e. directly after lithography), (2) patterned treated with 5 minutes O<sub>2</sub> plasma and (3) patterned treated with 5 minutes O<sub>2</sub> and 3 minutes N<sub>2</sub> plasma in VENUS reactor. The atomic compositions on the AlO<sub>x</sub> surface at each step is presented in table 5.2. After lithography, the C and F content in the layer is high: 22.8% and 19.3% respectively, and traces of S are detected as well. This is explained by the contamination induced during lithography process (remaining traces of photoresist) and the subsequent SF<sub>6</sub> plasma etching. As expected, C and O compositions are significantly reduced after the O<sub>2</sub> and N<sub>2</sub> plasma. Moreover, O is inserted in AlO<sub>x</sub> layer after O<sub>2</sub> plasma, as is N in this same layer after N<sub>2</sub> plasma (similar to SiO<sub>x</sub>N<sub>y</sub> layer).

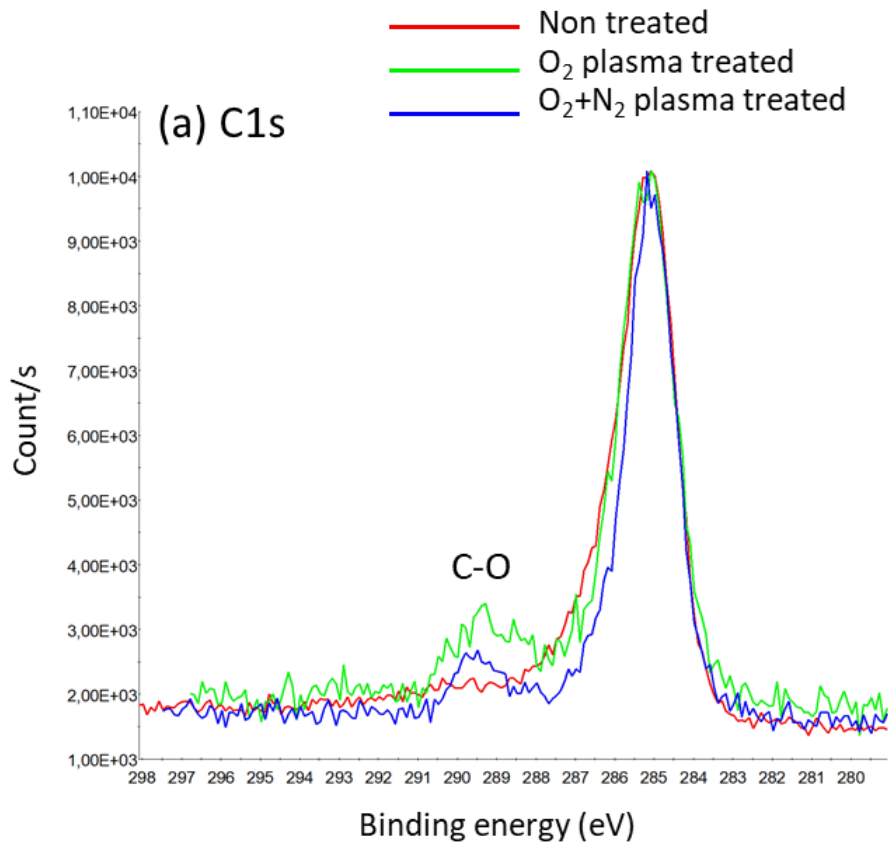
The traces of Si and N detected on AlO<sub>x</sub> surface allows us to consider the possibility of a deposition of a very thin layer of SiN after N<sub>2</sub> plasma. In fact, the ECR-PECVD chamber is not only used for O<sub>2</sub> and N<sub>2</sub> plasma treatments, but also for SiO<sub>x</sub>N<sub>y</sub> thin film deposition and chamber walls are not cleaned after each experiment. This may lead to SiN<sub>x</sub> sputtering from the antennae during N<sub>2</sub> plasma treatment, and redeposition on the treated surface. As seen previously, for short N<sub>2</sub> exposure times (3 minutes), this does not cause any growth of μc-Si on AlO<sub>x</sub> areas, and the selectivity is still conserved. However, this sputtering may be problematic for longer N<sub>2</sub> plasma process times.

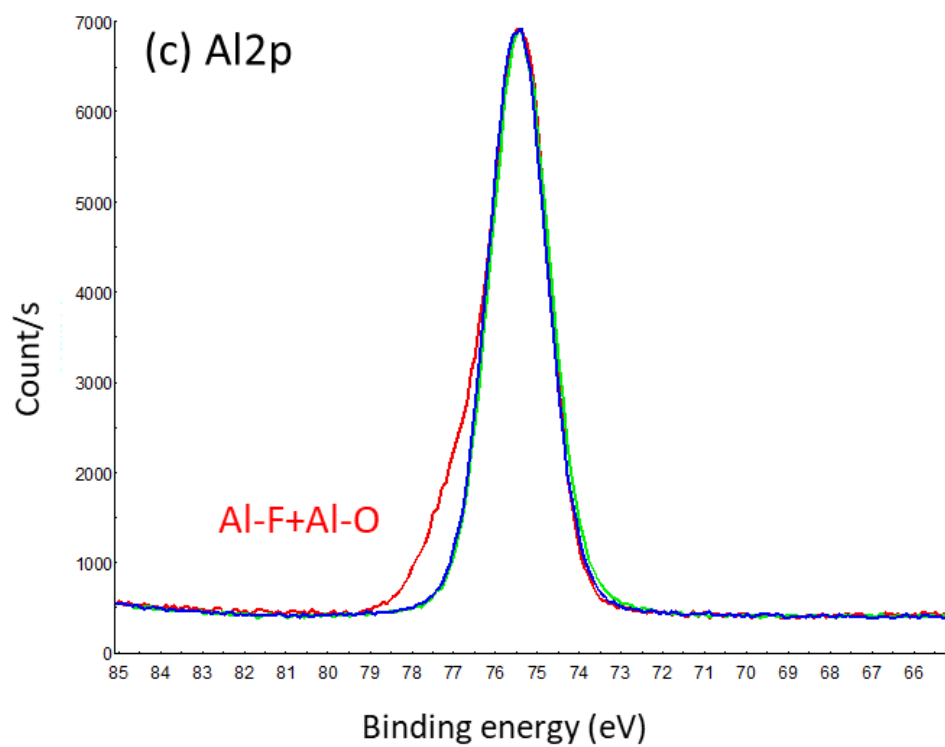
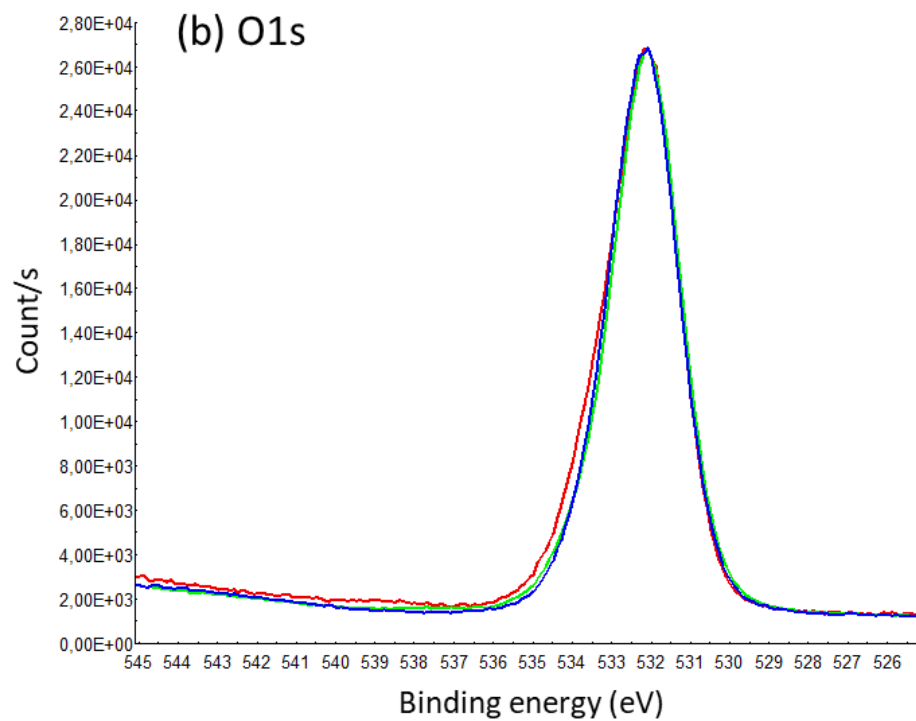
	Al2p	C1s	F1s	N1s	O1s	Si2p	S2p	Al/O
<b>Patterned non treated</b>	25.3	22.8	19.3	0.9	30.6	-	0.5	0.83
<b>After 5 minutes of O<sub>2</sub> plasma</b>	35.2	8.2	1.2	0.2	54.2	0.3	-	0.68
<b>After 5 mins O<sub>2</sub> plasma followed by 3 mins N<sub>2</sub> plasma</b>	32.5	10.8	1.8	5.3	47.2	1.8	-	0.73

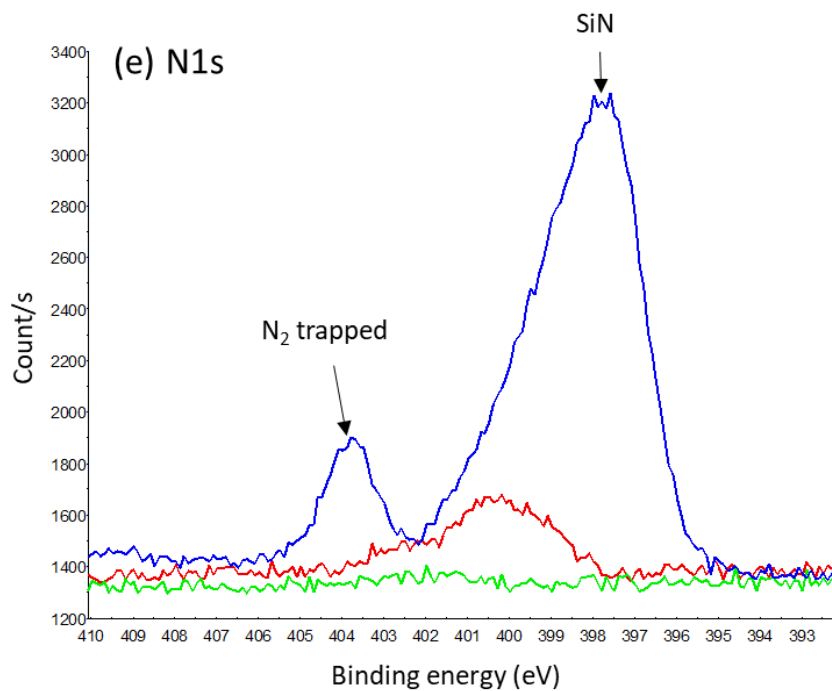
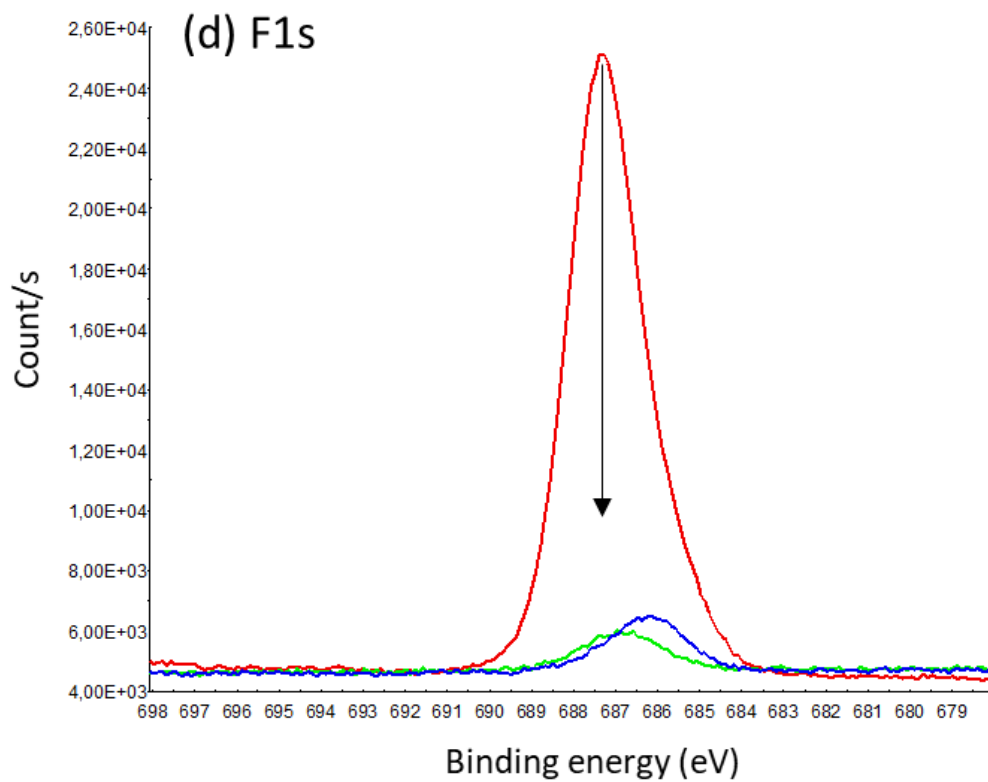
**Table 5.2** Atomic composition (in %) from XPS survey on AlO<sub>x</sub> surface for patterned samples in configuration 2A

In addition to the atomic composition analyses, C1s, O1s, Al2p, F1s, N1s and Si2p photoelectron peaks have been compared after each plasma treatment. In Fig. 5.13, C1s, O1s and Al2p spectra are normalized to the spectrum for the first, patterned, non-treated sample.

We can conclude that after plasma treatment (whether O<sub>2</sub> plasma or O<sub>2</sub> and N<sub>2</sub> plasma): (1) the charging effect is reduced since the shift in binding energies for O1s, Al2p and F1s peaks is reduced, (2) the appearance of C-O bonds can be noted (see Fig. 5.13a) and (3) the F1s peak is increasing. Also, before any plasma treatment, the Al2p peak is attributed to two bonds: Al-O and Al-F. The same effect happens when AlO<sub>x</sub> is exposed to the Ar/SiF<sub>4</sub>/H<sub>2</sub> AS-PECVD process (chapter 4). Last but not least, SiN deposition on the AlO<sub>x</sub> surface due to sputtering during the N<sub>2</sub> plasma is confirmed from Fig. 5.13e and 5.13f. However, this layer does not drive the nucleation of silicon on AlO<sub>x</sub> areas during an Ar/SiF<sub>4</sub>/H<sub>2</sub> plasma under AS-PECVD conditions, and so selectivity could be still achieved.







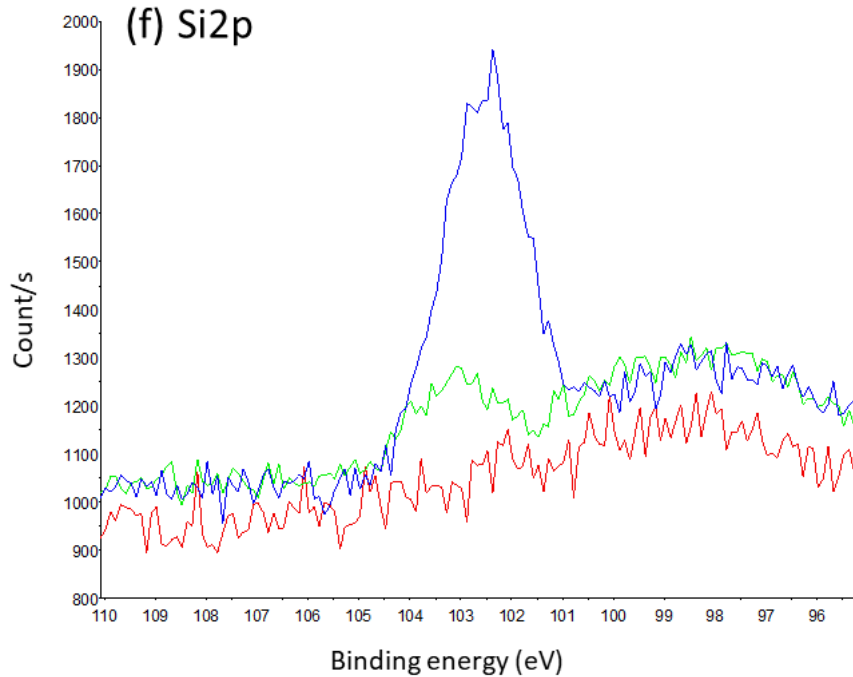


**Figure 5.13** (a) C1s, (b) O1s, (c) Al2p, (d) F1s, (e) N1s and (f) Si2p photoelectron spectra on AlO<sub>x</sub> area fabricated by lithography after any treatment (red), after O<sub>2</sub> plasma treatment (green) and after O<sub>2</sub> followed by N<sub>2</sub> plasma treatments (blue)

## 5.2.2 Area selective $\mu\text{-Si}$ on patterned substrates with different dimensions

As previously stated, the optimum steps for achieving area selective deposition on AlO<sub>x</sub>/SiO<sub>x</sub>N<sub>y</sub> patterns are:

- 5 minutes of O<sub>2</sub> plasma pretreatment in VENUS
- 3 minutes of N<sub>2</sub> plasma pretreatment in VENUS
- 20 minutes Ar/SiF<sub>4</sub>/H<sub>2</sub> plasma in ATOS under ASD conditions.

The final goal of my PhD was to check the sensitivity of our ASD process towards feature dimensions, as it is known that for certain ASD approaches (namely AS-ALD) that the selectivity is not the same between blanket and patterned areas of the same material.

We designed a photomask, shown in Fig. 5.14, that contains rectangles of  $2 \times 10 \text{ mm}^2$  with different spacing between them. The rectangles will become  $\text{AlO}_x$  areas, so this design allows us to have different feature dimensions of  $\text{SiO}_x\text{N}_y$  areas on the same substrate, and to check the selectivity of our AS-PECVD process for smaller features.

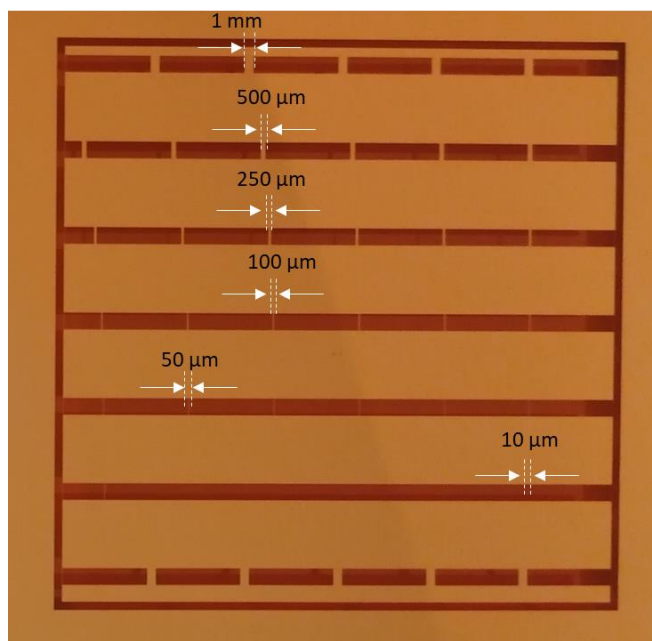


**Figure 5.14** Photo of photomask with different spacing between transparent rectangles

The patterned substrates were fabricated following the steps listed in section 5.1.1. Then, substrates were treated with 5 minutes of  $\text{O}_2$  plasma in the VENUS reactor, followed by 3 minutes of  $\text{N}_2$  plasma. Once treated, the patterned substrates were loaded in the PECVD reactor for the AS-PECVD process<sup>4</sup>. Fig. 5.15a shows an example of the resulting  $\text{AlO}_x/\text{SiO}_x\text{N}_y$  patterns, where the  $2 \times 10 \text{ mm}$  rectangles become  $\text{AlO}_x$  areas surrounded by  $\text{SiO}_x\text{N}_y$  material. The different dimensions of  $\text{SiO}_x\text{N}_y$  areas are determined by the rectangle spacing, as seen in Fig. 5.15b and 5.15c. In order to characterize  $\mu\text{c-Si}$  growth, SEM and AFM have been performed on (a) blanket areas (far from the pattern), (b)  $50 \mu\text{m} \times 2 \text{ mm}$  strips, and (c)  $15 \mu\text{m} \times 2 \text{ mm}$   $\text{SiO}_x\text{N}_y$  strips.

---

<sup>4</sup> For some reason, the  $\text{N}_2$  plasma was not necessary to restore growth on  $\text{SiO}_x\text{N}_y$  for those kind of patterned substrates. They required only an  $\text{O}_2$  plasma to obtain selective microcrystalline silicon on  $\text{SiO}_x\text{N}_y$  area while leaving the  $\text{AlO}_x$  area pristine.



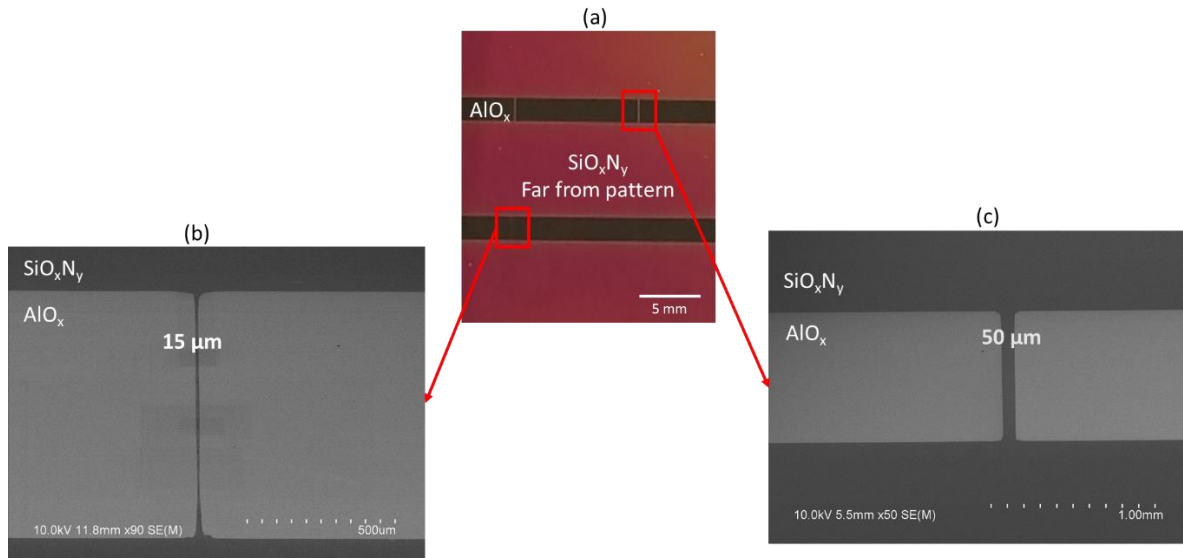


**Figure 5.15** (a) Photo of the  $\text{AlO}_x/\text{SiO}_x\text{N}_y$  pattern after AS-PECVD process and SEM images for two different  $\text{SiO}_x\text{N}_y$  area dimensions: (b)  $15\ \mu\text{m}\times 2\ \text{mm}$  and (c)  $50\ \mu\text{m}\times 2\ \text{mm}$

### a) Far from pattern (blanket)

Before starting to study the growth of  $\mu\text{c-Si}$  on  $\text{SiO}_x\text{N}_y$ , it is important to verify that the  $\text{AlO}_x$  area is indeed free of growth. Therefore, Fig. 5.16 shows a SEM image of the  $\text{AlO}_x$  area after AS-PECVD process. There are some very dispersed nuclei on the surface that could be due to some surface contamination that promotes the nucleation of Si during  $\text{Ar}/\text{SiF}_4/\text{H}_2$  plasma. However, their density is relatively small, and we consider that the process is selective.

Furthermore, on the  $\text{SiO}_x\text{N}_y$  far from pattern,  $\mu\text{c-Si}$  is growing in the same manner as it does on non-patterned samples<sup>5</sup>. The layer's roughness reaches a certain maximum and then decreases to a constant value when the layer becomes denser (Fig. 5.17). From ellipsometry modeling, the  $\mu\text{c-Si}$  thin film thickness is about 62 nm and the final roughness is about 13 nm. This last value is in good agreement with the RMS roughness extracted from the AFM image of Fig. 5.18 of the  $\text{SiO}_x\text{N}_y$  blanket area. Also, the SEM image of the same area is at approximately the same lateral magnification, and shows similar surface morphology.

<sup>5</sup> See figure 3.8 in chapter 3

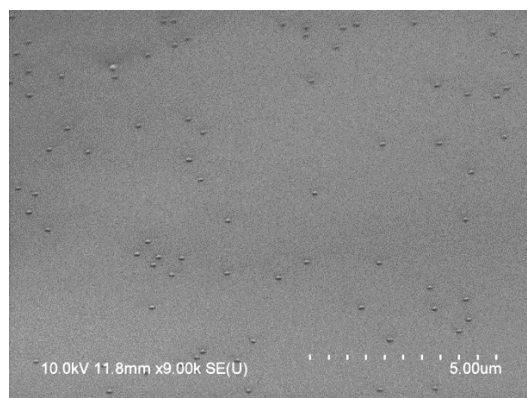


Figure 5.16 SEM image on top of  $\text{AlO}_x$  area

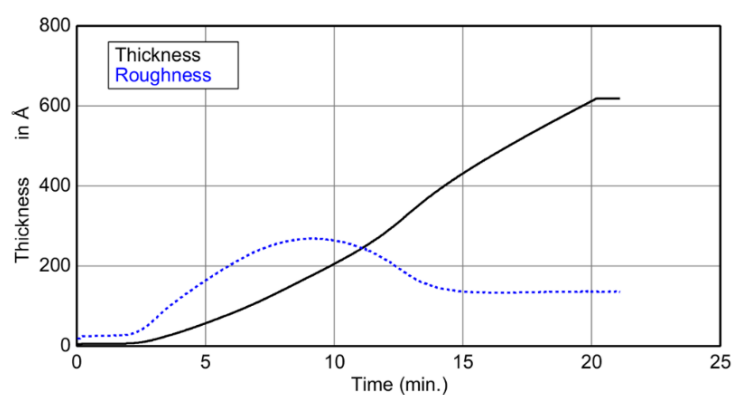


Figure 5.17 Evolution of  $\mu\text{c-Si}$  thickness and roughness with time when deposited on top of blanket  $\text{SiO}_x\text{N}_y$  area

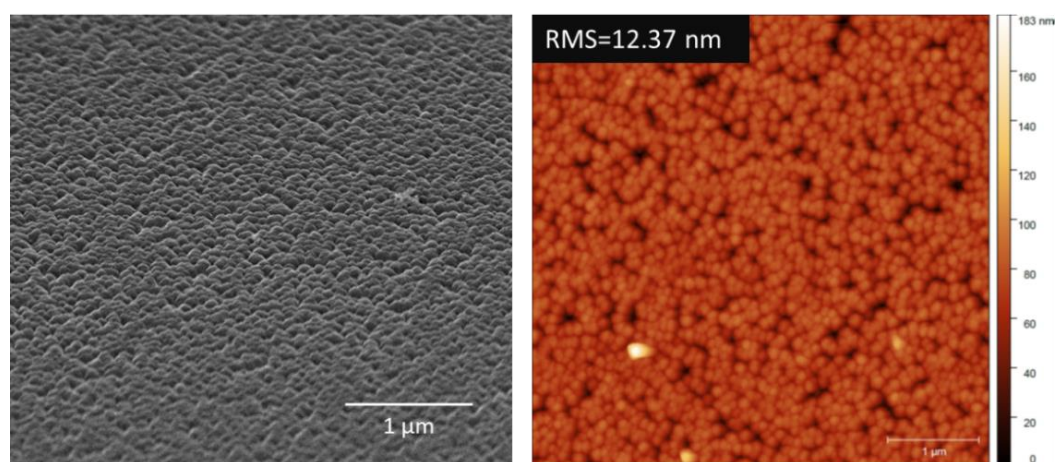


Figure 5.18 SEM and AFM images of blanket  $\text{SiO}_x\text{N}_y$  area

## **b) Reduced SiO<sub>x</sub>N<sub>y</sub> feature size**

We could not perform in-situ ellipsometry on the 15  $\mu\text{m}\times 2\text{ mm}$  and 50  $\mu\text{m}\times 2\text{ mm}$  SiO<sub>x</sub>N<sub>y</sub> feature sizes as the beam spot size is too big to fit in the whole area. Therefore, SEM and AFM have been applied to both areas to check for selectivity.

Firstly, 20x20  $\mu\text{m}^2$  SEM and AFM images were taken for the 15  $\mu\text{m}$  feature width and are presented in Fig. 5.19a and b. The fabricated pattern is not of great quality in terms of appearance, which can be explained by the loss of contrast and resolution during photolithographic fabrication. This may be due to multiple factors, such as light diffraction in the optical system during UV exposure (because of a relatively large air gap between photoresist and photomask or mask reflectivity [8]), an excess in developing time, or a poor adhesion of the photoresist to the substrate. However, we decided to not focus on the quality of the patterns, but rather study the sensitivity of our ASD process to the changes in area dimension. For this purpose, we extract the texture profile from the AFM image (Fig. 5.19 c) and estimate an 85 nm thick Si layer on top of a 70 nm of SiO<sub>x</sub>N<sub>y</sub> layer (the thickness of SiO<sub>x</sub>N<sub>y</sub> was calculated from spectroscopic ellipsometry data).

Closer views (5x5  $\mu\text{m}^2$ ) of the 50  $\mu\text{m}\times 2\text{ mm}$  and 15  $\mu\text{m}\times 2\text{ mm}$  SiO<sub>x</sub>N<sub>y</sub> areas are presented in figure 5.20. The SEM and AFM images indicate that for both feature dimensions, there is a deposition of  $\mu\text{c-Si}$  thin film consistent with small grains on the surfaces. Nevertheless, the RMS roughness is slightly higher for the 50  $\mu\text{m}$  (27 nm) feature width compared to the 15  $\mu\text{m}$  feature (22 nm).

This effect leads us to consider the possibility of having different thicknesses on top of each SiO<sub>x</sub>N<sub>y</sub> area. As these areas are much smaller than the ellipsometry spot, an estimation of silicon thickness has been extracted from the profile texture of each area, as illustrated in the 3D AFM images of figure 5.21. We found that by fixing the SiO<sub>x</sub>N<sub>y</sub> layer thickness to 70 nm, the layer on top - which is supposed to be  $\mu\text{c-Si}$  along with its roughness - is around 80 nm thick, and that this thickness is similar for both feature sizes.

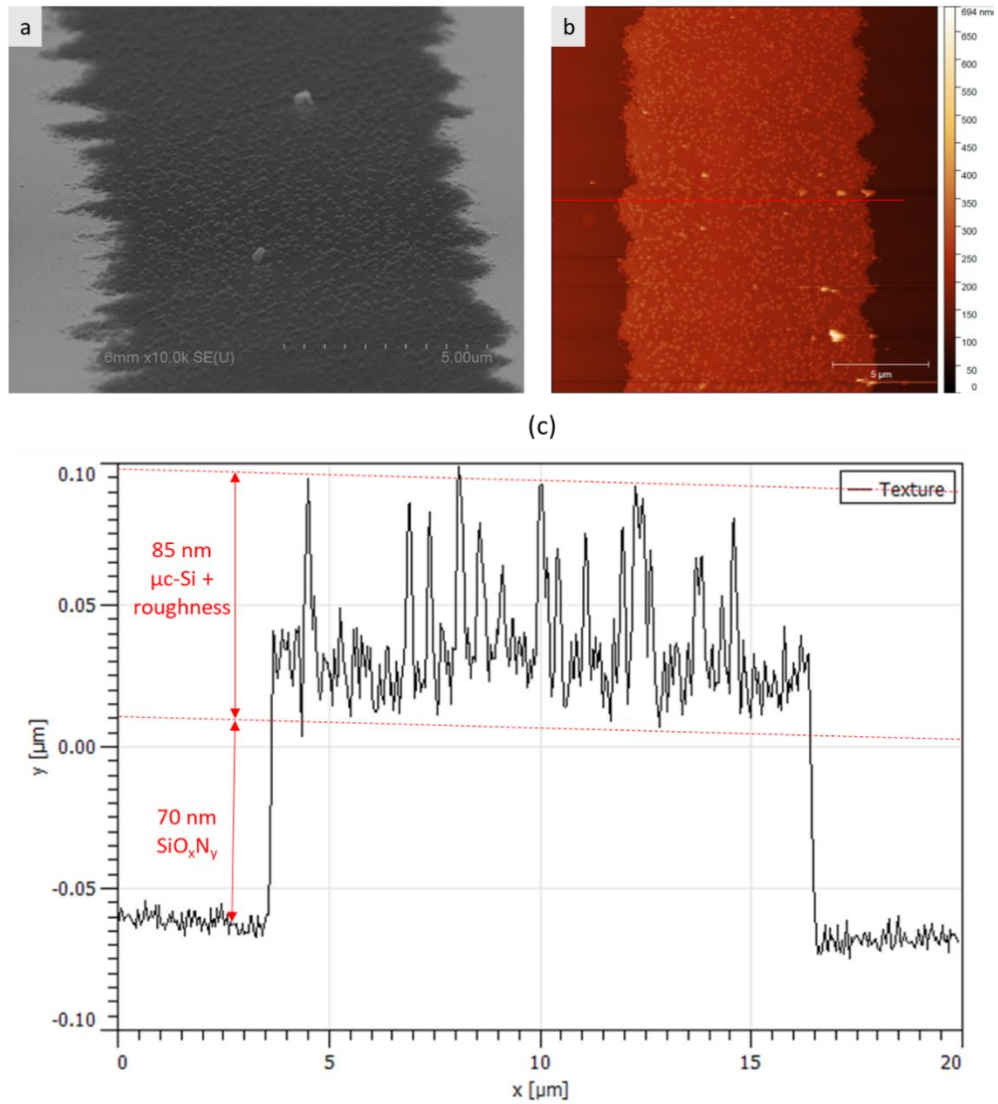
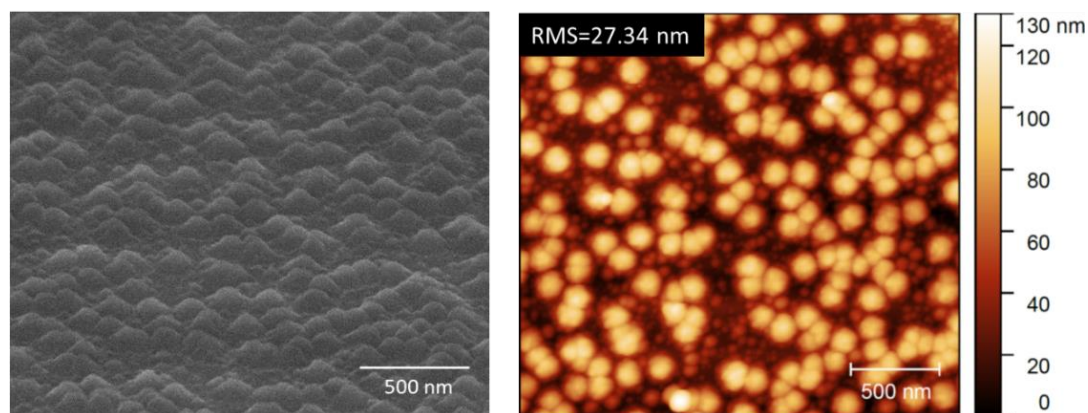


**Figure 5.19** (a) SEM image and (b) AFM image of the 50 μm×2 mm SiO<sub>x</sub>N<sub>y</sub> area. (c) profile corresponding to the line indicated in the AFM image.

(a)  $50\ \mu\text{m} \times 2\ \text{mm}$



(b)  $15\ \mu\text{m} \times 2\ \text{mm}$

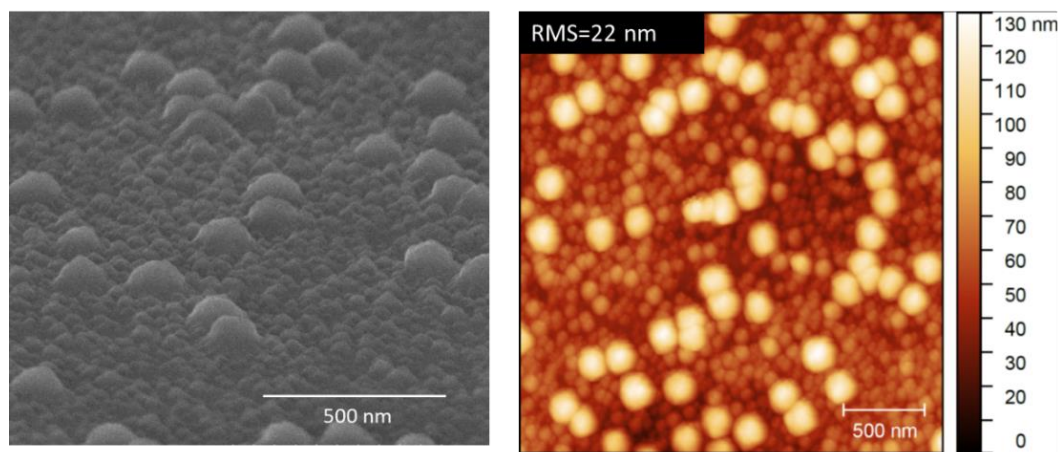


**Figure 5.20** AFM and SEM images of two  $\text{SiO}_x\text{N}_y$  areas with two dimensions: (a)  $50\ \mu\text{m} \times 2\ \text{mm}$  and (b)  $15\ \mu\text{m} \times 2\ \text{mm}$

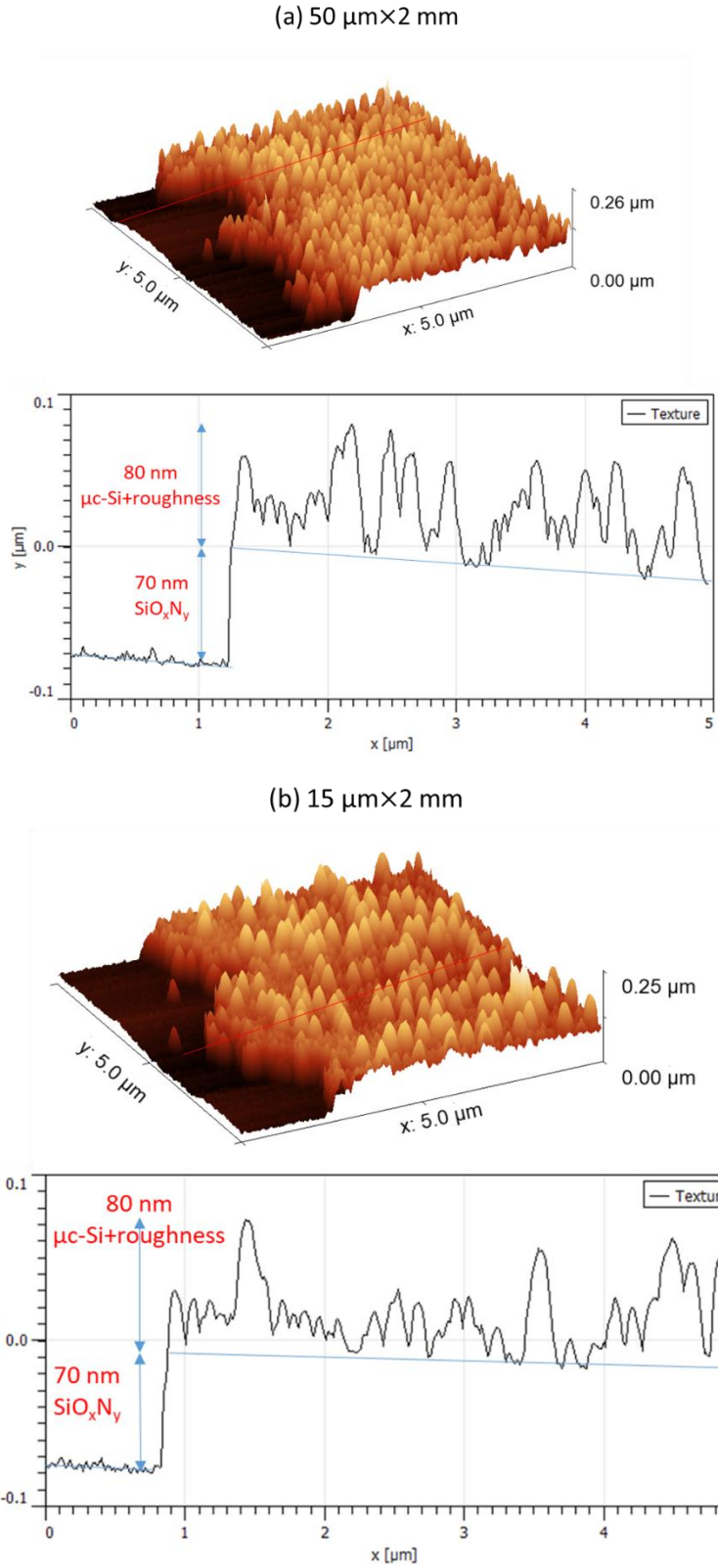


**Figure 5.21** AFM images in 3D representation with their corresponding texture profile for (a)  $50\ \mu\text{m} \times 2\ \text{mm}$  and (b)  $15\ \mu\text{m} \times 2\ \text{mm}$   $\text{SiO}_x\text{N}_y$  areas

Looking at Fig. 5.20a and b, one notes a difference in grain size distribution. To quantify this appearance, AFM data were also used to determine the grain size distribution on 50  $\mu\text{m}$  and 15  $\mu\text{m}$  feature widths. For this study, the “grain distribution” feature in Gwyddion software was employed to mark the grains by a chosen height threshold, and afterwards, to count the detected grains in terms of their equivalent radius. The equivalent grain radius in Gwyddion software is defined as the radius of the disk with the same projected area as the grain<sup>6</sup>.

The result is presented in Fig. 5.22. In this study, noise was not treated specifically during image treatment, so grains of  $< 10$  nm radius are mostly noise and grains with a radius  $> 90$  nm are agglomerates of multiple grains that should not be taken into account. We can conclude that:

- (i) At a height threshold of 86 nm, there are more grains of radius between 10 to 60 nm on the 50  $\mu\text{m}$  feature compared to the 15  $\mu\text{m}$  feature, on which grains tend to be larger (Fig. 5.21a)
- (ii) If we reduce the height threshold to 51 nm, only then on the 15  $\mu\text{m}$  feature could we detect a large number of grains with radii between 10 and 60 nm (Fig. 5.21b).

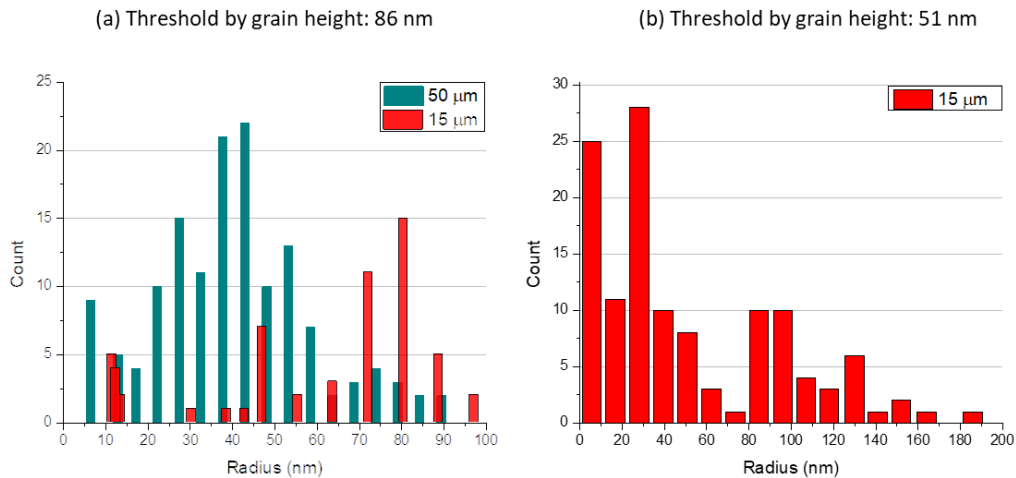


**Figure 5.22** Equivalent grain radius distribution marked by (a) 86 nm and (b) 51 nm height threshold

<sup>6</sup> For more details and examples about this method see references [9-11]

In Fig. 5.23, a comparison of  $\mu\text{c-Si}$  thickness and its roughness is illustrated for three  $\text{SiO}_x\text{N}_y$  areas: (a) far from pattern, (b)  $50\ \mu\text{m}$  and (c)  $15\ \mu\text{m}$ . The thickness on an area far from the pattern was measured by in-situ ellipsometry, while the thicknesses and surface roughnesses of the strips were measured by AFM. It is clear that Si is growing at almost the same growth rate everywhere, as the thicknesses are very similar. The RMS roughness is a little deceiving. It indicates higher values on  $50\ \mu\text{m}$  feature compared to  $15\ \mu\text{m}$  not because the silicon layer is rougher, but rather because there are homogenously larger grains on the  $50\ \mu\text{m}$  feature.

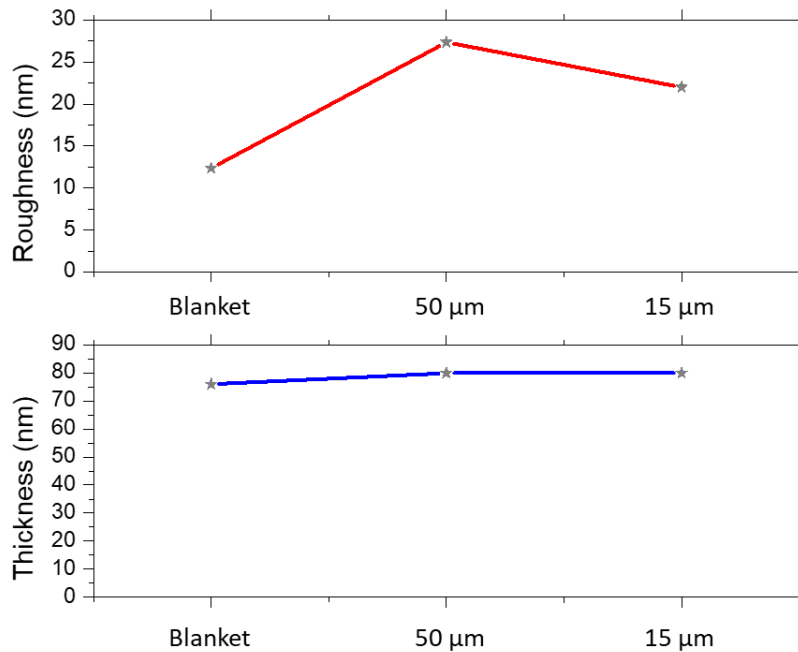


**Figure 5.23** Microcrystalline silicon film thicknesses (blue) and its roughness (red) on top of blanket,  $15\ \mu\text{m}$  and  $50\ \mu\text{m}$   $\text{SiO}_x\text{N}_y$  areas dimensions.

To conclude, the layer structure and morphology are different on each  $\text{SiO}_x\text{N}_y$  area. That is to say, **on the blanket  $\text{SiO}_x\text{N}_y$  area**, the grains representing  $\mu\text{c-Si}$  film are small and dense leading to a relatively smooth surface. **On  $50\ \mu\text{m}$  feature width**, Si layer is a mixture of small and medium dense grains. **On  $15\ \mu\text{m}$  feature width**, the Si layer consists of both small and rather sparse large grains.



### **5.3 Summary**

In order to obtain selective deposition when using  $\text{SiO}_x\text{N}_y/\text{AlO}_x$  patterns, additional steps are needed to remove surface contamination originating from the photolithography. The vital step before  $\text{Ar}/\text{SiF}_4/\text{H}_2$  AS-PECVD is a surface pretreatment by  $\text{O}_2$  plasma. XPS analyses proves that this  $\text{O}_2$  plasma removes organic contamination from the surface, including carbon, fluorine and sulfur traces that are present due to  $\text{SF}_6$  plasma etching and chemical solution during lithography. This will enhance the inhibition of silicon growth on the  $\text{AlO}_x$  area. However sometimes the  $\text{O}_2$  plasma pretreatment inhibits the growth of microcrystalline silicon on both growth and non-growth areas. In this case, a short  $\text{N}_2$  plasma (about 3 minutes) is necessary to recover the deposition of silicon on the growth  $\text{SiO}_x\text{N}_y$  area.

The fact that for every kind of pattern there is a different plasma treatment needed prior to the AS-PECVD process confirms the sensitivity of the ASD process to the surface properties. It can be affected by any minor change in the initial state of the surface or in the substrate preparation process, and great care must be taken in order to regularly reproduce results.

The chemical modification of  $\text{SiO}_x\text{N}_y$  and  $\text{AlO}_x$  surfaces derived from each plasma treatment was verified by contact angle measurements. We found that  $\text{O}_2$  plasma enhances the wettability of  $\text{SiO}_x\text{N}_y$  yielding to high surface energy, whilst the  $\text{N}_2$  plasma reduces again the surface energy; the water contact angle (which was  $25^\circ$ ) becomes closer to the initial WCA of the surface before any lithography ( $38^\circ$ ).

The nature of the chemical modification has been identified by XPS analysis. We found that  $\text{O}_2$  and  $\text{N}_2$  plasma insert O and N respectively in the  $\text{SiO}_x\text{N}_y$  and  $\text{AlO}_x$  layers. Furthermore, after  $\text{N}_2$  plasma, Si traces are detected on the  $\text{AlO}_x$  area. This possibly may explain the presence of unwanted nucleation on this non-growth area, as seen in SEM images.

The ASD process is not only sensitive to the surface pretreatment but also to the distribution of  $\text{AlO}_x$  and  $\text{SiO}_x\text{N}_y$  areas on the surface. In fact, when the  $\text{AlO}_x$  area is

surrounding a small  $\text{SiO}_x\text{N}_y$  area, selectivity is lost as well as all  $\mu\text{c-Si}$  growth. Even after  $\text{O}_2$  or  $\text{N}_2$  plasma treatment, we weren't able to grow silicon on either  $\text{SiO}_x\text{N}_y$  areas nor on  $\text{AlO}_x$  areas. It seems to be a macroscopic effect, as selectivity is still achieved for small spacing in the reverse case, i.e.  $\text{SiO}_x\text{N}_y$  area is surrounding a small  $\text{AlO}_x$  area (Fig. 5.15).

Finally, selective deposition is achieved on  $\text{SiO}_x\text{N}_y$  in forms of strips with feature dimensions down to  $15\ \mu\text{m}$  without any  $\mu\text{c-Si}$  deposition on  $\text{AlO}_x$  areas. In situ ellipsometry and AFM shows that the silicon deposited selectively is  $61\ \text{nm}$  thick. On the  $\text{SiO}_x\text{N}_y$  areas far from pattern, the roughness of the layer is around  $13\ \text{nm}$ . This roughness increases when feature dimensions are reduced. Moreover, the structure and the morphology of the  $\mu\text{c-Si}$  layer selectively deposited on  $\text{SiO}_x\text{N}_y$  varies depending on feature dimensions. It is consistent of a mixture of small and medium grains on  $50\ \mu\text{m}$  feature, large and dispersed grains on  $15\ \mu\text{m}$  feature and small and dense grains on "far from pattern" or "blanket" areas.

## References

- [1] Michael S. Hibbs, "System Overview of Optical Steppers and Scanners" in *Microlithography: Science and Technology*, Second Edition, p. 40-46, (2007).
- [2] Bryce C, Berk D. Kinetics of the dissolution of copper in iron (III) chloride solutions. *Industrial & engineering chemistry research*. 1995 Apr;34(4):1412-8.
- [3] S. M. Irving, *Kodak Photoresist Seminar*, 2, 26, (1968)
- [4] B.A. Thedjoisworo, D. Cheung, and D. Zamani, "Characterization of hydrogen-plasma interactions with photoresist, silicon, and silicon nitride surfaces", *J. Vac. Sci. Technol. A Vacuum, Surfaces, Film*. 30, 031303 (2012).
- [5] Guillaume Fisher, PhD thesis, "Plasma nanotexturing of silicon for photovoltaic applications: tailoring plasma-surface interactions for improved light management", *Ecole Polytechnique-Paris Saclay University*, November 2018.
- [6] R.H.A. Ras, E. Sahramo, J. Malm, J. Raula, and M. Karppinen, "Blocking the Lateral Film Growth at the Nanoscale in Area-Selective Atomic Layer Deposition", *J. Am. Chem. Soc.* 130, 11252 (2008).
- [7] X. Yu and H. Hantsche, Fresenius. "Some aspects of the charging effect in monochromatized focused XPS", *J. Anal. Chem.* 346, 233 (1993).
- [8] K. Suzuki and B. W. Smith, "Microlithography science and technology", second edition. Taylor & Francis Group, LLC, (2007), see chapter 1 page 37-38.
- [9] P. Klapetek, I. Ohlídal, D. Franta, A. Montaigne-Ramil, A. Bonanni, D. Stifter, H. Sitter: Atomic force microscopy characterization of ZnTe epitaxial films. *Acta Physica Slovaca* 53 (2003) 223–230, doi:10.1143/JJAP.42.4706
- [10] Duman, Ali Nabi. "Grain analysis of atomic force microscopy images via persistent homology." *Ultramicroscopy* 220 (2021): 113176.
- [11] Chicea, D., B. Neamtu, R. Chicea, and L. M. Chicea. "THE APPLICATION OF AFM FOR BIOLOGICAL SAMPLES IMAGING." *Digest Journal of Nanomaterials & Biostructures (DJNB)* 5, no. 4 (2010).

# *Conclusion and Perspectives*

Plasma Enhanced Chemical Vapor deposition is a potentially useful technique to achieve an Area Selective Deposition process through the use of a fluorinated precursor. In this thesis, we were able to: (i) identify a process window for which the selective deposition by PECVD could be obtained, (ii) understand the mechanism behind this selectivity, and finally (iii) verify the sensitivity of the process to small area dimensions.

## **Area selective PECVD process**

We determined the optimal Ar/SiF<sub>4</sub>/H<sub>2</sub> plasma conditions that allow the selective growth of microcrystalline silicon ( $\mu\text{c-Si}$ ) thin film on silicon oxynitride (SiO<sub>x</sub>N<sub>y</sub>) area and prevent its growth on an aluminum oxide (AlO<sub>x</sub>) area situated on the same substrate. Those same plasma conditions prevent silicon growth on other material such as aluminum and nickel. We found that the selectivity is very sensitive to the concentration of H<sub>2</sub> in the gas mixture, to the radio frequency plasma power and to the electrode temperature. As a result, a slight change in the PECVD conditions (such as the increase of plasma power from 10 W to 15 W or the electrode temperature from 100°C to 175°C) would cause the deposition of  $\mu\text{c-Si}$  on AlO<sub>x</sub> surfaces. In addition to the plasma conditions, we observed a sensitivity of the AS-PECVD process to the surface contamination and plasma walls condition.

## **Plasma-surface interaction**

Under AS-PECVD conditions, plasma species, most likely via creation of volatile compounds on the SiO<sub>x</sub>N<sub>y</sub> surface, create favorable sites for Si nucleation. At the same time those plasma species react with the AlO<sub>x</sub> surface creating strong Al-F bonds in the form of a very stable AlF<sub>3</sub> layer, preventing the nucleation of Si. This AlF<sub>3</sub> layer also enhanced the wettability of AlO<sub>x</sub> surface.

In general, PECVD is not a surface-dependent technique and deposition should occur on any kind of material. As an exception, Ar/SiF<sub>4</sub>/H<sub>2</sub> PECVD becomes surface-dependent

under area selective deposition conditions. In order to understand the particularity of this plasma, series of experiments using different RF excitation frequencies with constant plasma powers were done. However, we found that the mechanism is more complicated than expected and further measurements are required.

### **Use of area-selective PECVD on patterned samples.**

The last part of this work was dedicated to fabrication of patterned samples and the study of their sensitivity towards the AS-PECVD process. We found that a plasma pretreatment of O<sub>2</sub> and N<sub>2</sub> plasma is necessary to obtain selective deposition of microcrystalline silicon on SiO<sub>x</sub>N<sub>y</sub> versus AlO<sub>x</sub>. The role of O<sub>2</sub> plasma was to remove contamination derived from fabrication process. However, Si normally does not grow on SiO<sub>x</sub>N<sub>y</sub> areas after the treatment, as O<sub>2</sub> plasma changes the chemical composition of these areas. As N<sub>2</sub> plasma, when performed after O<sub>2</sub> plasma treatment, modifies again the composition of SiO<sub>x</sub>N<sub>y</sub> in such a way that restores selectivity again. It is not just the SiO<sub>x</sub>N<sub>y</sub> composition that varies with plasma treatment but also the surface wettability. In fact, O<sub>2</sub> plasma enhances the wettability of the SiO<sub>x</sub>N<sub>y</sub> while N<sub>2</sub> plasma reduced it.

Our AS-PECVD process provides selectivity on SiO<sub>x</sub>N<sub>y</sub> feature dimensions down to 15 μm. The structure and the morphology of the deposited microcrystalline silicon differ from large areas to smaller ones, while growth rate does not change.

### **Perspectives.**

Some of the results that we observed during my PhD were not interpreted and it would be good to study them to gain better understanding of the selective process. Namely, (i) study the relationship between surface free energy and plasma chemistry or (ii) find an explanation on the sensitivity of our AS-PECVD process to the macroscopic distribution of AlO<sub>x</sub> and SiO<sub>x</sub>N<sub>y</sub> areas on the substrate, as it is a strange observed effect.

Furthermore, measuring ion energy distribution function for non-selective plasma conditions i.e. for plasma power of 15W, electrode temperature of 175°C or H<sub>2</sub> gas flow above 20 sccm, could help correlate the role of the ions in the plasma in obtaining selectivity.

As was mentioned in the manuscript, the patterned substrates prepared for small features have low resolution, so it is worth to fabricate samples with higher quality. It could be also interesting to try AS-PECVD process on area dimensions far below 10  $\mu\text{m}$ .

Since the current area selective deposition research is confined mostly to the Atomic Layer Deposition technique (ALD), it would be interesting to generalize our AS-PECVD to be able to apply it in an area selective plasma enhanced ALD (PEALD) approach.

Finally, it could be useful for technological application to study new precursors to allow the selective deposition of other materials, for example metals. In addition, extending the application of the AS-PECVD process to solar cell fabrication by combining it with the localized plasma process developed in the laboratory using a patterned power electrode could be beneficial.



# Appendix

- A Thermal evaporation and sputtering techniques
- B Optical Emission Spectroscopy and X-Ray Diffraction Spectroscopy
- C Unexplained images in Scanning Electron Microscopy
- D Ion Energy Measurements



# Appendix A

## Thermal evaporation and sputtering techniques

Thermal evaporation deposition technique consists in heating materials (usually in the form of powders, grains or pellets) in a vacuum chamber until reaching their evaporating point. The material vapors will traverse the distance between the crucible/boat and substrate (typically several tens of centimeters) more or less following Knudsen's cosine law of molecular flow into vacuum and condense then on a relatively cold substrate forming a thin film (for more details about thermal evaporation technique see references [1]). In our case, a Boc Edwards A306 thermal evaporator was used and its schematic representation is given in Fig. A1. The metals are held in a tungsten boat (W is a refractory metal that can be used at the temperatures up to 2500 °C) and are evaporated by heating the boat applying a high electric current through it. A high energy electron beam can also be used to evaporate solids.

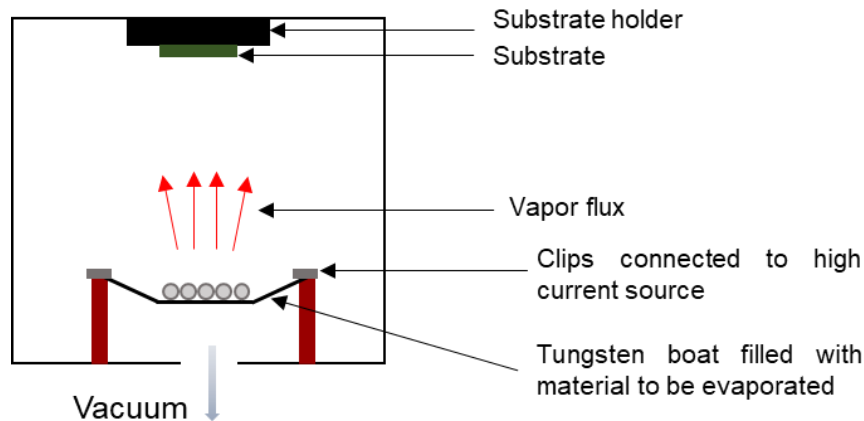


**Figure A1** Schematic representation of thermal evaporator chamber

Magnetron sputtering technique is another physical vapor deposition method for depositing thin film used in this thesis. It is based on sputtering a target material by energetic ion bombardment in a low-pressure magnetized plasma. The atoms are ejected from the surface of the target by impinging heavy (usually  $\text{Ar}^+$ ) gaseous ions, traverse the distance between target and substrate (typically several centimeters), reach the substrate surface and

condenses on the surface forming thin layer. Magnetron sputtering uses a strong magnet, placed behind the target to confine the electrons generated in argon plasma (at the pressure in order of a millitorr) near the target surface. By confining the plasma near the target, higher density of electrons (and ions) is reached where it is needed for higher sputtering rate and to prevent any resputtering of the deposited material [2-4].

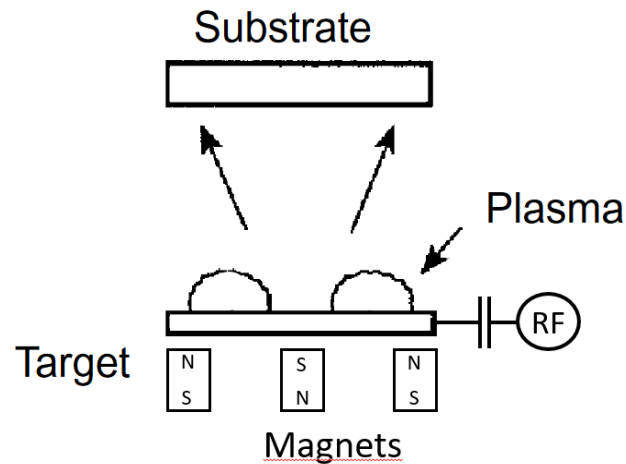


**Figure A2** Schematic representation of RF magnetron sputtering (adapted from [3] ).

## References

- [1] Donald M. Mattox, Deposition Processes, “The Foundations of Vacuum Coating Technology”, William Andrew Publishing, 2003, Pages 11-33, Editor(s): Donald M. Mattox, <https://doi.org/10.1016/B978-081551495-4.50009-7>.
- [2] Wasa Kiyotaka, Thin Film Processes, “Thin film materials technology: sputtering of control compound materials”, Springer Science & Business Media, 2004, Pages 17-69.
- [3] Donald M. Mattox, Chapter 1 Introduction and Chapter 7 Physical Sputtering and Sputter Deposition (Sputtering), Handbook of Physical Vapor Deposition (PVD) Processing (Second Edition), William Andrew Publishing, Pages 1-24 and pages 237-286, 2010, <https://doi.org/10.1016/B978-0-8155-2037-5.00001-0>

[4] C. Charpentier, “Investigation of deposition conditions and annealing treatments on sputtered ZnO:Al thin films: Material properties and application to microcrystalline silicon solar cells”, *PhD thesis*, École Polytechnique, 2012.

# Appendix B

## B1 Optical Emission Spectroscopy

Optical Emission Spectroscopy is an analytical technique used to get the information on the composition of the plasma. The certain number of excited and ionized molecules and atoms in the plasma emit photons during de-excitation that can be detected by a spectrometer. Those emissions have distinct energy spectra, which allow to attribute the emission lines to specific species. Analyzing the full emission spectra of the plasma we may identify its major constituents. The 13.56 MHz Ar plasma emission spectra recorded in ATOS reactor at following conditions is presented in Fig. B1.

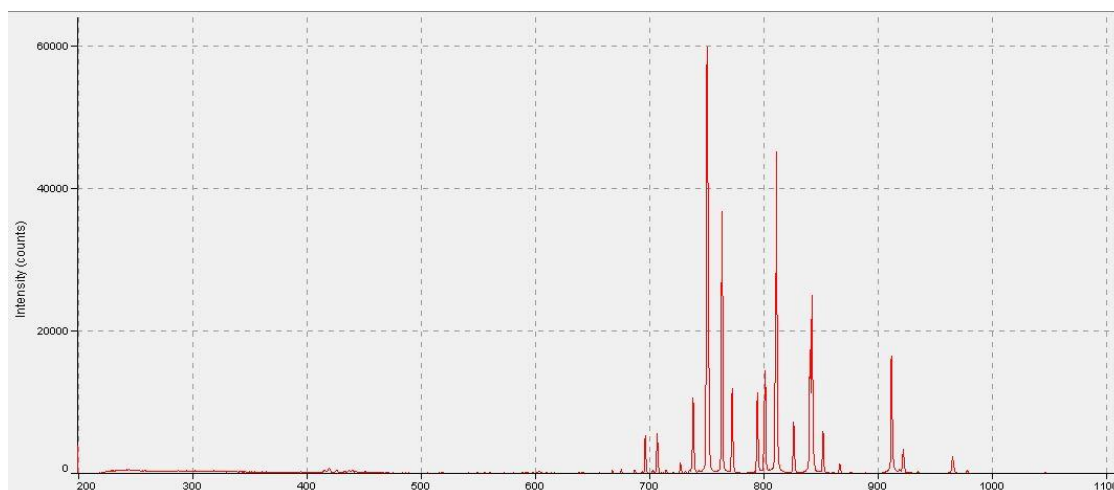


**Figure B1** Emission spectra of Ar in ATOS reactor.

Optical system usually focusses collected light into an optical fiber, that is used to guide the light to a diffracting grating-based spectrophotometer. The diffraction grating in the spectrometer splits the light and images it to the detector that measures the intensity of light for each wavelength. The measured peak position will thus depend on the composition of the plasma (presence of certain species) and intensity on species concentration, power, injected to the plasma, transparency of the optical system and grating design and quantum efficiency (sensitivity) of the detector to the photons of particular energy. With each specie

having a set of specific emission wavelengths, by analyzing this emission spectrum, we can get idea on what is happening in the plasma.

## B2 X-ray diffraction.

X-Ray Diffraction is an experimental method to determine the atomic and molecular structure of a crystal. It consists of illuminating the sample with an X-Ray beam. The signal observed is related to the atomic structure of the sample. The principle is: when X-Ray beam interact with the electrons presented in the sample a diffraction happens due to the small wavelength comparable with the size of the electron in a sample; the process is known as elastic scattering. Hence when moving the illumination source and the detector, constructive and destructive interferences will occur depending on the position of the electron and therefore the atomic structure of the sample. On the detector side the signal varies for very specific angles (Fig. B2). The interferences between the light scattered from the electron structure and the incident beam follow Bragg law. The angular distribution of the detected signal allows to retrieve the structure of the sample.

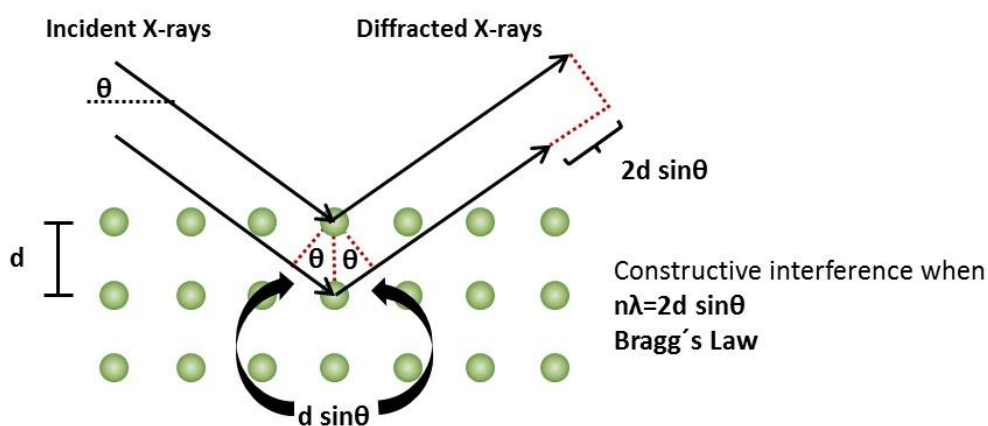


**Figure B2** X-ray diffraction principle. [Credits: <https://wiki.anton-paar.com/at-de/roentgendiffraction-xrd/> ]

In this work, we used grazing incidence x-ray diffraction mode (Fig. B3) where the incident beam is fixed at a small angle with the sample surface and the detector is moving.

This geometry enhances the diffraction intensity of a thin film while reducing the signal from the substrate [1].

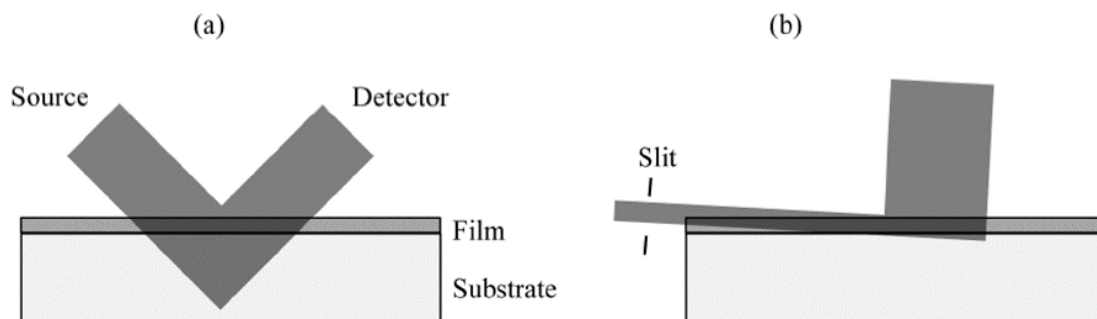


**Figure B3** Schematic of (a) conventional and (b) grazing incidence x-ray diffraction (extracted from reference [1])

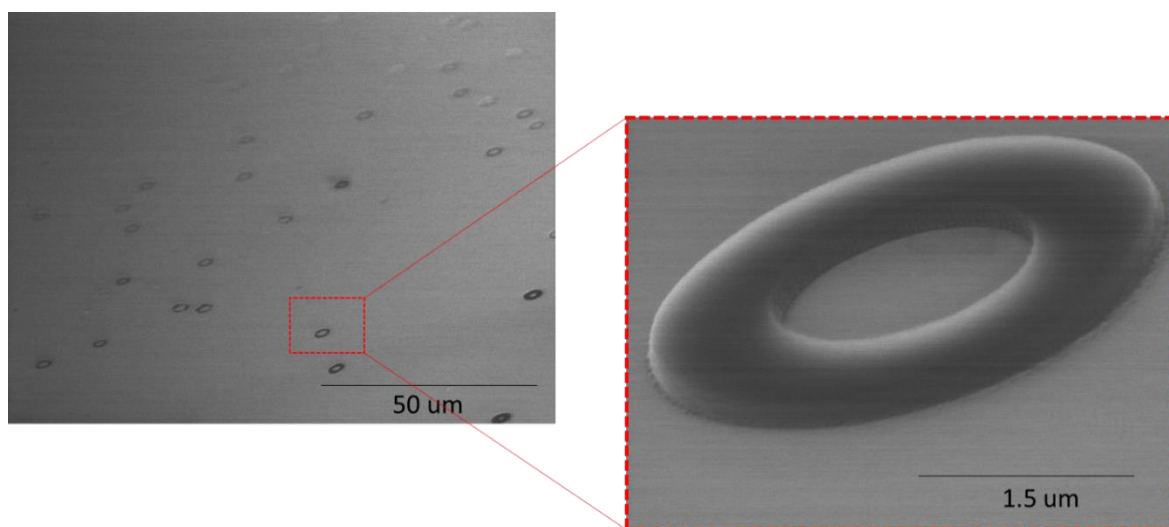
## Reference

[1] Myeongkyu Lee, “X-Ray diffraction for materials research: from fundamentals to applications”. CRC Press, 2017.

## Appendix C

### Unexplained SEM images

Those donut shaped structures were found, for some cases, on patterned samples on  $\text{AlO}_x$  area. A curiosity.



# Appendix D

## Ion Energy Measurements

A Semion Retarding Field Energy Analyser (RFEA) by Impedans was used to measure the ion flux and the ion energy distribution function (IEDF) hitting the substrate. The analyser is made of four grids (G0, G1, G2 and G3) and a collector plate (C) as shown in figure D1. G0 prevents plasma formation within the RFEA and is equal to Vdc. G1 repels electrons coming from the plasma that enter into the sensor. G2 discriminates the ions based on their energy. G3 creates a retarding potential for secondary electrons that can be emitted from the surface of the collector. C is the collector electrode that attracts the ions for detection. In our case, the button probe sensor was mounted on the grounded electrode to measure plasma ion flux and energy under ASD conditions, i.e. 200/14/20 sccm of Ar/SiF<sub>4</sub>/H<sub>2</sub> gas fluxes, electrode temperatures of 100°C, power of 10 W, and pressures of 0.3 Torr and 1.5 Torr. We chose G1=C=-50V, G3=-60V, G0=0V (sensor is mounted to the grounded electrode) and G2 range=[-60V, +60V] with 1.0 V step.

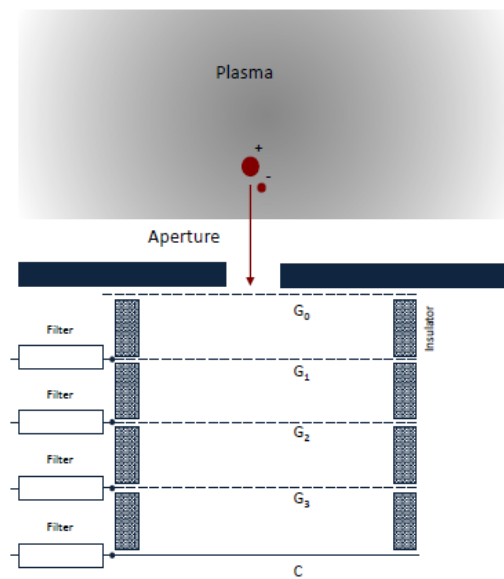


**Figure D1** Semion RFEA structure (credits: Impedans Ltd, Semion Technical, [www.impedans.com](http://www.impedans.com))



Figure D2 shows the current-voltage (IV) curve and its first derivative for low pressure (0.3 Torr) and high pressure (1.5 Torr). By comparing the two graphs we can notice that the data are exploitable for low pressure but it is not the case for high pressure-the conditions that are more useful to our application.

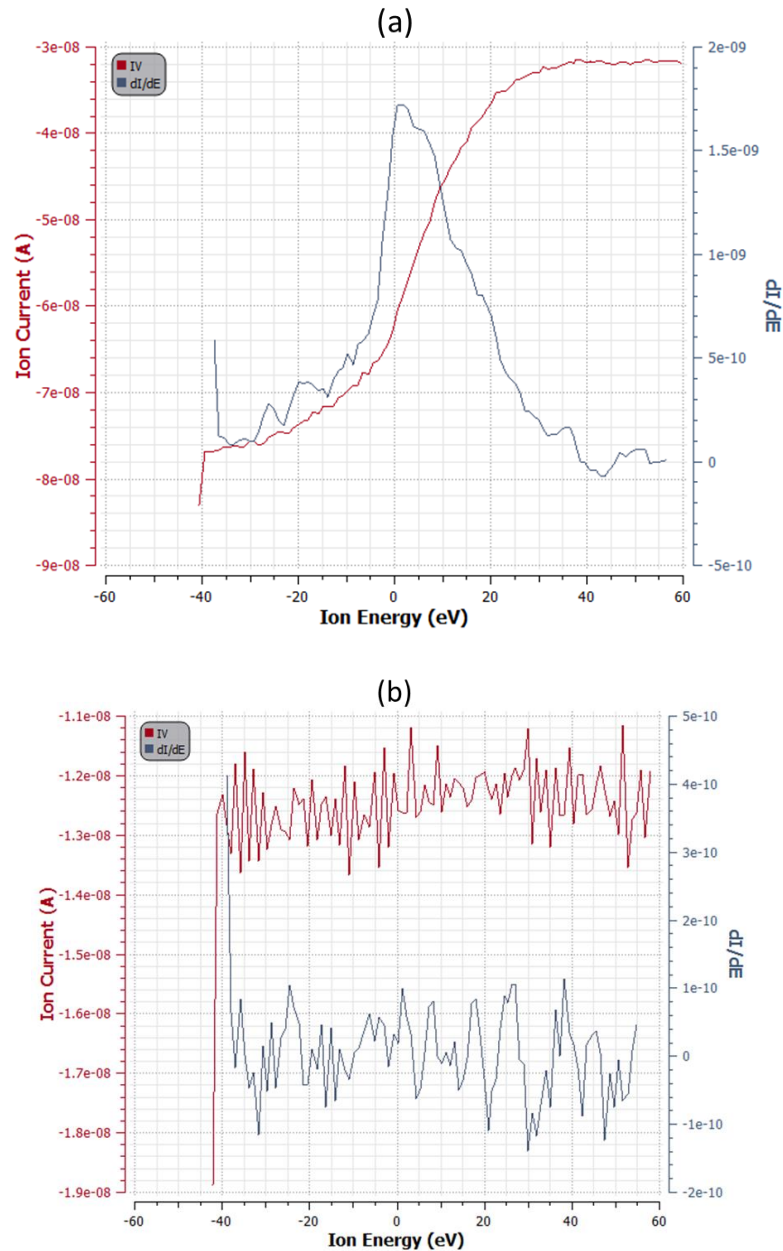


**Figure D2** Current-voltage (IV) curve and its first derivative for a pressure of (a) 0.3 Torr and (b) 1.5 Torr under ASD plasma conditions

# ***List of publication***

## **Peer reviewed journals**

- **G. Akiki**, D. Suchet, D. Daineka, S. Filonovich, P. Bulkin, and E. V. Johnson, “Area Selective Deposition of Silicon by Plasma Enhanced Chemical Vapor Deposition using a Fluorinated Precursor “, **Applied Surface Science** 531, 147305 (2020)
- **G. Akiki**, M. Frégnaux, I. Florea, P. Bulkin, D. Daineka, S. Filonovich, M. Bouttemy and E. V. Johnson, “Origin of Area Selective Plasma Enhanced Chemical Vapor Deposition of Microcrystalline Silicon”, **Journal of Vacuum Science & Technology A** 39, 013201 (2021)

## **Conference oral and poster presentations**

- Contributed talk, ICANS 28, *August 2019*, Palaiseau, France
- Contributed talk, AVS 66, *October 2019*, Columbus, USA
- Poster presentation, ASD 19, *April 2019*, Leuven, Belgium
- Poster presentation, ASD 20, *April 2020* Stanford, California, USA (cancelled due to COVID19 crisis)
- Oral (virtual) in 73rd Annual Gaseous Electronics Virtual Conference *October 5-9 2020*
- Oral (virtual) presentation in AVS 67 Showcase held in *October 27-29, 2020* (Finalist in PSTD Coburn and Winters Award)
- Oral (virtual) presentation in Area Selective Deposition Workshop, *April 2021*
- Oral (virtual) presentation in AVS 67 Virtual Symposium, *October 25-29 2021*
- Oral presentation, MRS Fall Meeting, *29 November-02 December 2021*, Boston, USA



# *Résumé de la thèse*

L'industrie des semi-conducteurs fait face au défi complexe de la miniaturisation qui nécessite de fabriquer de motifs de l'ordre de la dizaine de nanomètres (nm). Cette fabrication s'avère en outre coûteuse et même parfois impossible à cette échelle avec les techniques de photolithographie actuelles. Le développement de procédés de dépôt par croissance sélective (Area-Selective Deposition ASD) est une solution prometteuse et attractive permettant la réduction des étapes de préparation ce qui engendre une diminution du coût et du temps de fabrication. Cette approche « bottom-up » contrôle et localise la croissance d'une couche mince sur une zone bien spécifique du substrat. En d'autres termes, le procédé ASD en lui-même est intrinsèquement conçu pour favoriser le dépôt sur une zone du substrat appelée « zone de croissance » et empêcher le dépôt sur la « zone de non croissance » (les deux zones sont constituées de deux matériaux différents). Les principales techniques utilisées dans ce domaine sont la technique de dépôt de couche atomique (ALD) et la technique de dépôt chimique en phase vapeur (CVD). Les approches ASD consistent soit en la désactivation de la zone de non croissance par des molécules chimiques ; soit en l'activation de la zone de « croissance » par des traitements plasma. Le dépôt sélectif peut être également réalisé en combinant le dépôt et la gravure dans un même procédé en se basant sur le délai de nucléation entre deux matériaux différents. L'objectif de ma thèse était de développer une nouvelle approche ASD en utilisant une technique de dépôt chimique en phase vapeur assisté par plasma (PECVD).

La première partie de la thèse exploite la chimie du plasma  $\text{Ar/SiF}_4/\text{H}_2$  qui permet la croissance sélective et locale de couches minces de silicium microcristallin ( $\mu\text{-Si}$ ) sur une surface d'oxynitride de silicium ( $\text{SiO}_x\text{N}_y$ ), tandis que pour les mêmes conditions de plasma, la croissance du  $\mu\text{-Si}$  n'est pas assurée sur une surface d'oxyde d'Aluminium ( $\text{AlO}_x$ ), sachant que les deux matériaux se trouvent sur le même substrat de silicium. Nous avons constaté que cette sélectivité ne pourrait être obtenue que pour des conditions de plasma spécifiques, appelée les conditions AS-PECVD. Notamment la sélectivité est très sensible à la concentration de  $\text{H}_2$  dans le mélange de gaz, à la puissance radiofréquence du plasma et à la température des électrodes. Notre approche basée sur le plasma, est une méthode simple qui ne nécessite qu'une seule étape pour déposer

sélectivement 55 nm de  $\mu\text{-Si}$  sur  $\text{SiO}_x\text{N}_y$  (vérifier par l'ellipsométrie) pendant une durée relativement courte (20 minutes) par rapport aux approches alternatives basées sur la technique « Atomic Layer Deposition » (ALD). Les mêmes conditions AS-PECVD assurent le dépôt sélectif sur différents matériaux, notamment sur les métaux. Dans cette section, nous avons également montré des cas où le dépôt plasma  $\text{Ar/SiF}_4/\text{H}_2$  n'est pas sélectif, ce qui signifie que la croissance du silicium a eu lieu à la fois sur les zones  $\text{SiO}_x\text{N}_y$  et  $\text{AlO}_x$ . Par exemple, l'augmentation de la puissance du plasma de 10 W à 15 W ou la température des électrodes de 100°C à 175°C entraîne le dépôt de  $\mu\text{-Si}$  sur des surfaces  $\text{AlO}_x$ .

Dans la deuxième section, nous nous sommes concentrés sur les chimies de surfaces du  $\text{SiO}_x\text{N}_y$  et  $\text{AlO}_x$  afin de comprendre l'origine de notre procédé AS-PECVD. Les techniques basées sur la spectroscopie aux rayons X (X-ray Photoelectron Spectroscopy - XPS et Energy Dispersive X-ray spectroscopy - EDX) ont permis de détecter une grande quantité d'atomes de fluor sur la zone  $\text{AlO}_x$  suite à la formation de liaisons Al-F au-dessus de cette zone. Par conséquent, le plasma  $\text{Ar/SiF}_4/\text{H}_2$  sous les conditions AS-PECVD crée un « masque chimique » d' $\text{AlF}_3$  empêchant la nucléation du silicium microcristallin sur la zone  $\text{AlO}_x$ . Au niveau du plasma, en général, la PECVD est une technique indépendante de la surface et le dépôt se produit sur tout type de matériel. Pourtant, le plasma  $\text{Ar/SiF}_4/\text{H}_2$ , sous des conditions particulières (conditions de dépôt sélectif), est devenu dépendant de la surface. Donc, pour comprendre la particularité de ce plasma, des séries d'expériences avec différentes fréquences d'excitation RF pour une puissance de plasma constante ont été faites. En effet, en variant la fréquence, l'énergie de bombardement ionique change ce qui peut affecter la sélectivité. Cependant, nous avons constaté d'après ses expériences que ce n'est pas simplement l'énergie de bombardement ionique qui entraîne la croissance de silicium sur la zone  $\text{AlO}_x$ . C'est probablement dû au flux d'espèces de plasma arrivant sur les surfaces qui augmente avec l'augmentation de la puissance du plasma.

La dernière section s'intéresse à l'application du procédé AS-PECVD sur des échantillons présentant des motifs, fabriqués par photolithographie, pour vérifier la sensibilité de notre procédé vis-à-vis les dimensions de surface. La préparation de ces motifs engendre des contaminations sur les surfaces, ce qui nécessite des étapes supplémentaires de nettoyage par plasma d'oxygène et d'activation de la surface de « croissance » par plasma d'azote. Les analyses XPS et les mesures d'angle de contact ont montrés que les traitements en plasma modifient la composition chimique

des surfaces  $\text{SiO}_x\text{N}_y$  et  $\text{AlO}_x$  ainsi que leurs mouillabilités. Nous montrons que le procédé de dépôt par croissance sélective est possible sur des surfaces de  $\text{SiO}_x\text{N}_y$  de petites dimensions (de l'ordre de  $15\ \mu\text{m}$ ). La structure et la morphologie de la couche  $\mu\text{c-Si}$  déposée sélectivement sur  $\text{SiO}_x\text{N}_y$  varie en fonction des dimensions de la surface. Elle consiste d'un mélange de grains petits et moyens sur un trait de  $50\ \mu\text{m}$ , de grains gros et dispersés sur un trait de  $15\ \mu\text{m}$  et de grains petits et denses sur les zones "loin du motif". Même si la morphologie et la structure du  $\mu\text{c-Si}$  sont modifiés avec la dimension des motifs, le taux de croissance reste lui constant.

Pour conclure, le dépôt chimique en phase vapeur assisté par plasma est une technique potentiellement utile pour réaliser un procédé de dépôt par croissance sélective ou ASD grâce à l'utilisation d'un précurseur de dépôt fluoré. Dans cette thèse, nous avons pu : (i) identifier une fenêtre de procédé pour laquelle le dépôt sélectif par PECVD pourrait être obtenue, (ii) comprendre le mécanisme derrière cette sélectivité, et enfin (iii) vérifier la sensibilité du procédé aux petites dimensions de surface. Puisque la sélectivité est possible sur de petites surfaces, ce procédé PECVD de dépôt par croissance sélective peut être potentiellement employer pour la fabrication de dispositifs à base de semi-conducteur nécessitant des étapes de dépôt localisé. De plus, il peut être un bénéfice dans la fabrication de cellules solaires.

**Mots clés :** Dépôt par croissance sélective, PECVD, semi-conducteurs, silicium-microcristallin, analyse-de-surface



**Titre :** Dépôt par croissance sélective de silicium microcristallin par PECVD : Origine physique, défis et solutions.

**Mots clés :** Dépôt par croissance sélective, PECVD, semiconducteurs, silicium-microcristallin, analyse-de-surface

**Résumé :** Cette thèse de doctorat est consacrée d'une part à la démonstration d'un nouveau procédé de dépôt par croissance sélective utilisant la technique de dépôt chimique en phase vapeur assisté par plasma (PECVD) et d'autre part à la compréhension de son origine physique. Sous des conditions bien spécifiques appelées AS-PECVD, le plasma Ar/SiF<sub>4</sub>/H<sub>2</sub> permet la croissance sélective et locale de couches minces de silicium microcristallin hydrogéné ( $\mu\text{c-Si:H}$ ) sur une surface d'oxynitride de silicium ( $\text{SiO}_x\text{N}_y$ ), tandis que la croissance du  $\mu\text{c-Si:H}$  n'est pas assurée sur une surface d'oxyde d'Aluminium ( $\text{AlO}_x$ ). Les mêmes conditions AS-PECVD assurent le dépôt sélectif sur différents matériaux, notamment sur les métaux.

En dehors de ses conditions, le plasma Ar/SiF<sub>4</sub>/H<sub>2</sub> n'est pas sélectif, ce qui signifie que la croissance du silicium a eu lieu à la fois sur les zones  $\text{SiO}_x\text{N}_y$  et  $\text{AlO}_x$ . Des techniques de caractérisation de surface par rayons X ont détectées une grande quantité d'atomes de fluor sur la zone  $\text{AlO}_x$ . Ce qui suggère la formation de liaisons Al-F empêchant la nucléation du  $\mu\text{c-Si:H}$  sur la zone  $\text{AlO}_x$ .

Le procédé AS-PECVD a été appliqué à des échantillons à motifs fabriqués par photolithographie. La sélectivité est possible sur des surfaces de  $\text{SiO}_x\text{N}_y$  de petites dimensions (de l'ordre de 15  $\mu\text{m}$ ) ce qui peut être un bénéfice dans la fabrication de semi-conducteurs.

**Title:** Area selective deposition of microcrystalline silicon by PECVD: physical origin, challenges and solutions.

**Keywords :** Area-selective-deposition, PECVD, semiconductors, microcrystalline-silicon, surface-analysis

**Abstract :** This PhD thesis is devoted to the demonstration of a new area selective deposition process based on the plasma enhanced chemical vapor deposition (PECVD) technique and to understanding the physical origin behind it. For specific plasma conditions, which we term AS-PECVD conditions, Ar/SiF<sub>4</sub>/H<sub>2</sub> plasma selectively and locally deposit hydrogenated microcrystalline silicon ( $\mu\text{c-Si:H}$ ) thin films on silicon oxynitride ( $\text{SiO}_x\text{N}_y$ ) while preventing their growth on aluminum oxide ( $\text{AlO}_x$ ). The same AS-PECVD conditions provide selectivity on different materials as well, notably on metals. While outside AS-PECVD conditions, Ar/SiF<sub>4</sub>/H<sub>2</sub> plasma deposition is not selective meaning that

silicon growth occurred on both  $\text{SiO}_x\text{N}_y$  and  $\text{AlO}_x$  areas. X-ray spectroscopy based techniques were able to detect a large quantity of fluorine atoms on  $\text{AlO}_x$  area. This is due to the formation of Al-F bonds on top of this non-growth area preventing the nucleation of  $\mu\text{c-Si:H}$  on it.

The AS-PECVD process was applied to patterned samples fabricated by photolithography. Selectivity was achieved on smaller  $\text{SiO}_x\text{N}_y$  features (on the order of 15  $\mu\text{m}$ ). Therefore, it remains possible that AS-PECVD can be used for semiconductor device fabrication at even smaller scales.